博士論文

論文題目　　Characterization of aerosol sources with potential post-emission particle-size transitions

(排出後に粒子径変化の可能性を持つエアロゾル発生源の特性評価)

氏　　名　　阿部レネー曜

Abe René Yo

Doctoral Thesis

Characterization of aerosol sources with potential post-emission particle-size transitions

（排出後に粒子径変化の可能性を持つエアロゾル発生源の特性評価）

Thesis Advisor: Associate Professor Yoshiaki Akutsu

Submitted by

René Yo Abe

August 2015

Department of Environment Systems
Graduate School of Frontier Sciences
The University of Tokyo

Table of Contents

1. Abstract

Aerosols with high potential of particle size changes during or after emission have been characterized for two types of aerosol particles. Primary Biological Aerosol Particles (PBAP) which can be broken up during emission or re-suspension processes and aerosols produced by pyrotechnics which show a dramatic change in optical properties through hygroscopic growth at high humidity conditions have been investigated. Protein content was measured in urban ambient aerosol sampled with an Andersen type high-volume cascade-impactor with four stages over a year in a suburban area near Shibuya. Although protein is present in most primary biological aerosol particles, it has rarely been quantified in particulate matter. Depending on the analysis method, it can also be used as tracer for specific source types. We obtained amino acid profiles using an HPLC method from particulate matter hydrolysate in order to apply a receptor model for source apportionment. Protein content was found to make up around 0.5 to 2% of particulate matter. Through seasonally variable amino acid compositions some emission sources, e.g., pollen and fallen leaves were observed at higher contributions for large particles (d>7 μm) in spring and winter, respectively. These findings indicate the presence of biological material in all particle size fractions down to the sub-micrometer range at similar mass proportions. For aerosol emissions from pyrotechnics, a method for measuring and characterizing optical properties and humidity characteristics was developed, in order to allow comparison of aerosols from different pyrotechnics. These methods were applied, in order to assess the effects of metal and metal compound additives on aerosol properties. A linear relationship between mass of vaporized metal chlorides and light extinction caused by aerosol at high relative humidity has been observed. Both types of aerosol particles were found to evolve to a size around 1 μm and therefore perform very well as particles potentially harmful to health through their ability to penetrate through the whole respiratory tract as well as as cloud condensation nuclei which occur at high number concentrations because of their small size but are not too small to allow uninhibited growth.

2. Introduction

Anthropogenic emissions of air pollutants have been causing health and environmental problems for centuries on urban scales. Starting in the late nineteenth century impact of smoke emissions occur with increased severity, including thousands of deaths caused by air-pollution episodes. However, it was not until the second half of the twentieth century that extensive research on atmospheric aerosols was pursued. (Jacobson, 2005a) Chemical composition and size of aerosol particles (particulate matter) vary greatly depending on the way they are generated. Natural sources include sea spray, soil dust, pollen, spores, bacteria, and emissions from volcanic activity, natural fires and lightning, while anthropogenic sources include fly-ash from combustion of fossil-fuel, biomass and traffic-related uplift of dust and soil. (Jacobson, 2005b) Advances in sampling, chemical analysis methods as well as data evaluation methods have led to global inventories and observation networks of particulate matter.

Particle size affects both lifetime in the troposphere as well as penetration depth into the human body. Particles smaller than 10 μm (cf. PM_{10}, SPM) remain suspended in the atmosphere for around 1 week and are likely to accumulate depending on meteorological factors, especially in urban regions. They can penetrate into the respiratory tract where, at elevated concentrations, they exert adverse effects on health. 2.5 μm is the size of particles which can reach the pulmonary alveoli representing the largest deposition surface for fine aerosol particles (cf. $PM_{2.5}$). Even smaller particles receive more attention not only because of their penetration depth into the respiratory tract but also because they can act as adsorbent for volatile species through their large specific surface area or even penetrate into the blood (cf. Section 3.2).

In global meteorological predictions, on the other hand atmospheric aerosols are assigned the largest and almost only cooling effect on the Earth's energy balance but are at the same time associated with the largest uncertainty ranges due to difficulties in measurements and lack of observations of some relevant properties. Size-distribution and hygroscopicity are key parameters determining aerosol-radiation interactions and aerosol-cloud interactions which strongly influence direct and indirect radiative forcing of aerosol on climate. Scattering interaction of aerosol particles with radiation in the Mie-regime as opposed to weak Rayleigh-scattering (primarily by N_2 and O_2 molecules) becomes significant for particle sizes larger than the respective radiation's wavelength (cf. Mie scattering in Section 3.1.2) and is together with interaction with cloud particles responsible for most of the cooling effects in the radiative forcing model. (IPCC, 2013)

Particles with diameters around 0.5 μm or more play a role for solar radiation. Due to dependence of total scattering intensity on the number of relevant particles, volume or mass based scattering efficiency decreases inversely proportional to the third power of particle size. With most of the solar irradiance in the visible and near infrared spectrum of light, particles of a size around 1μm scatter solar radiation most efficiently per unit mass of suspended particles. On the other hand, small particles (around some 100 nm) emitted by, e.g., combustion processes, or generated as secondary aerosols by nucleation from gases do not strongly interact with relevant radiation. They can however grow by aging processes or act as cloud condensation (or ice) nuclei to form coarse mode (>1 μm) particles or cloud droplets if they are adequately wettable. As such accumulation mode particles (around 100 nm to 1 μm) occur at high number concentrations while retaining a high potential to form light scattering particles. Through combination of these properties they play an important role in the Earth's energy balance.

Primary (directly emitted) and secondary aerosol particles (produced from gaseous precursors) are subject to environmental processes and conditions, under which particle sizes are not maintained. Particles from some emission sources can therefore be found in other particle size classes, than at the time of emission. In this thesis, two different aerosol source types are characterized regarding post-emission changes of their particle size distributions resulting in accumulation mode concentrations which are higher than presently recognized. One is primary biological aerosol particles (PBAPs), contributions of which to accumulation mode particles have generally been neglected although small particles like bacteria or fragments of plant and animal tissue can be found in some aerosols. (Miguel, et al., 1999; Bauer, et al., 2003) Small particles of biological material are also emitted in aerosols produced by human activity like re-suspended material ground down by traffic or vapors emitted during food preparation processes. These particles have hitherto not been sufficiently tracked in atmospheric measurements. Size distributions of PBAPs therefore need to be revised to account for small particles generated by break down of particles previously classified as mostly coarse or giant particles, especially for urban aerosols. The other is combustion of pyrotechnic compositions which is scarcely considered in atmospheric aerosols except during specific episodes. Aerosol particles emitted by pyrotechnic compositions share their mechanism of particle generation with fly ash as a mixture of particles produced from undercooled vapors and spray of at least partly fused residue if not all components are completely vaporized during combustion. Due to differences in combustion speed and particle

concentrations as well as chemical composition, however, separate characterization of their particle size distribution and hygroscopic behavior is required. Especially volatile metal compounds responsible for flame coloration which are optimized for producing their respective metal chloride vapors but also vaporized combustion products originating from fuel and oxidant produce accumulation mode particles at high concentrations (Dutschke, et al., 2011).

Both aerosols from pyrotechnics and PBAPs are good cloud condensation nuclei (CCN). The latter have been reported in cloud droplets in the form of spores and bacteria. Single or clusters of multiple such entities as particles fit into the size range of the accumulation mode, but also fragments of biological material may be contributing. Large PBAPs such as pollen are also suggested as giant CCN which do not actually serve as condensation nuclei but initiate coalescence of cloud droplets which cannot grow further grow efficiently by condensation and therefore play a role in formation of precipitating hydrometeor particles. Aerosols from pyrotechnics, on the other hand, are highly hygroscopic. Generation of persistent much more opaque aerosol plumes under high humidity conditions depicts these particles' superior performance as cloud condensation nuclei (CCN) requiring much lower supersaturations than most other CCN to form aqueous cloud droplets. Presence of such particles can prevent higher supersaturations to be reached which most other CCN require to get activated and form cloud droplets, thereby promoting formation of larger cloud droplets (because of lower number concentrations) which in turn can more efficiently be scavenged by large hydrometeors.

Although these two aerosol source types are active as CCN mostly through particles of the same size class of accumulation mode, characterization of their post-emission particle size transitions require completely different approaches regarding their measurement. PBAPs in urban aerosols are subject to processes such as road traffic or other human activities which grind down or break up particles over a relatively wide area and time scale. They need to be tracked by a class of tracer species specific to PBAPs but allowing distinction of a number of different PBAP sources. Aerosols emitted by pyrotechnics generate their particles through a phase transition from the gas phase and undergo their size transition from Aitken mode (<100 nm) to accumulation (about 100 nm to 1 μm) or the lower coarse mode (>1 μm) in much shorter time scales due to their extreme concentrations during emission. These particles required observations in chamber experiments under controlled temperature and humidity conditions to capture

their hygroscopic behavior. The physical basis required to measure and describe aerosol properties as well as health considerations and aerosol emission- and growth-mechanisms of the aerosol sources are further described in Chapter 3.

In Chapter 4, PBAPs' size distribution in urban ambient aerosol is analyzed using amino acids in hydrolysate of particulate matter. Size of terrestrial primary biological aerosol particles (PBAPs) has generally been categorized as consisting mostly of coarse mode particles with a mass based mode maximum at 2 to 3 µm. Though PBAPs smaller than 2 µm have long been recognized as sources of organic particulate matter, they have been paid less attention to than other anthropogenic or geologic sources and contributions to accumulation mode has been thought to be small. Recent studies report significant contributions of fungal spores to urban atmospheric aerosol as well as bacteria and other microorganisms in cloud water samples, the latter indicating their role as ice nuclei in aerosol-cloud interactions. PBAPs' possible contributions to global climate changes have been recognized in processes like cloud nucleation but need to be explored yet. (Després, et al., 2012) Size resolved analysis of protein amino acids provides data for tracing most PBAPs and can be used to detect or even identify unknown sources or small particles formed by breakup of larger PBAPs if suitable data sets are compiled.

Chapter 5 characterizes hygroscopic properties of aerosol particles emitted during combustion of fireworks, which are reported mainly in the sub-µm range (Dutschke, et al., 2011) but also contain a significant number of large particles of up to a few mm. The latter causing characteristic fallout near the firework scene can be considered a local phenomenon with impacts on spectators, residents or neighboring areas. The fine fraction shares its properties with fly-ash from other combustion processes in that it contains high proportions of alkaline, alkaline earth and heavy metals specific to their respective sources as can be found in ambient aerosols (Wang, et al., 2007), but cannot be mitigated by measures like filtration as in process plants. Most firework aerosols are also known to produce highly opaque smoke plumes at high humidity conditions. In this work, a measurement method using an un-pressurized combustion chamber is developed for studying this hygroscopic behavior quantitatively. By analyzing the effect of ambient humidity-conditions and ingredients used in pyrotechnic compositions on visible aerosol development, measures to reduce these aerosols and their visibility can be tested for efficiency.

Through characterization of these aerosol sources' size distributions, their contributions

to the Earth's radiative budget can be refined. Especially high concentrations of sub-micrometer particles which act as condensation- or ice-nuclei can have a significant impact on aerosol-cloud interactions. Chapter 6 summarizes the contributions of PBAPs which were found to contain sub-µm particles at concentrations comparable to the coarse size fractions to urban ambient aerosols and hygroscopic growth behavior of aerosols from pyrotechnics which themselves show strong aerosol radiation interactions at high humidity conditions and can be considered very good cloud condensation nuclei.

3. Theoretical Part

3.1. Particulate Matter

In the field of receptor measurements dusts are always a very complex mixture of a multitude of components. There are several means of classifying dust. Primary and secondary particles can, for example be distinguished. Primary particles are emitted already as particles at its source and occur unaltered in receptor samples. Examples are mineral dust from soil erosion or soot particles which originate from operating diesel motor vehicles. Secondary particulate components are generated from gaseous precursors through transformation processes in the atmosphere (e.g., oxidation). Sulfate, which is generated from SO_2, can be mentioned as example here.

Another way of classification is assigning components to its or its precursor's sources. Here the differentiation of anthropogenic and natural sources is often a first step. Important anthropogenic sources of particulate matter which by far are causing the largest part of particulate matter emissions include

- industrial and commercial production processes,
- combustion processes (motor vehicles, residential heating, etc.),
- mechanical processes (abrasion from streets, re-suspension of dusts),
- secondary production from other pollutants such as SO_2, NO_x and NH_3 as well as volatile organic compounds (VOC).

The main natural sources of particulate matter are:

- Soil erosion
- Evaporation of water from spray particles and crystallization of salt components (e.g., sea spray)
- Soot and fly ash from naturally occurring combustion processes (e.g., forest fires)
- Volcanic activity
- Uplift (re-suspension) of eroded materials (e.g., desert sand)
- Secondary aerosols from natural precursors (e.g., emissions from plants)

Both classifications are combined in Table 1 which lists the main components as well as their precursors or sources. (Marhold, 2003)

Table 1. Main components of dust and their precursors/sources

	Component	Precursors/Sources
Primary Components	soot	combustion processes
	geologic materials	construction, agriculture, traffic, wind
	heavy metals	combustion, manufacturing
	abrasion particles	mechanical stress
	biological materials	spores, plant debris
Secondary Components	sulfate	sulfur dioxide
	nitrate	nitrogen oxides
	ammonium	ammonia
	organic carbon	VOC (Volatile Organic Carbon)

3.1.1. Aerodynamic Properties

First classification of dusts suspended in the atmosphere is ensued almost exclusively by particle size. Because determination of actual sizes for particles of mostly irregular geometric form is difficult or not meaningful, the concept of an aerodynamic diameter is introduced. It describes particles with a diameter a spherical particle with a density of 1g cm^{-3} would need to have in order to display the same settling velocity as the particle in observation.

To distinguish dust by particle size, particles are generally divided into three size classes:

- Total suspended particles (TSP) corresponds to particles with settling speeds $\leq 10 cm \cdot s^{-1}$
- PM_{10} (Particulate Matter 10 μm) are particles with an aerodynamic diameter ≤ 10 μm (more exact definition: particles passing an inlet with a separation efficiency of 50% for particles with an aerodynamic diameter of 10 μm)
- $PM_{2.5}$ (Particulate Matter 2.5 μm) are particles with an aerodynamic diameter ≤ 2.5 μm (more exact definition: particles passing an inlet with a separation efficiency of 50% for particles with an aerodynamic diameter of 2.5 μm)

Instead of PM_{10} which was introduced in 1987 by the USA, Suspended Particulate Matter (SPM) with a slightly different definition of particles < 10 μm (particles passing an inlet with a separation efficiency of 100% for particles with an aerodynamic diameter of 10 μm) approximately corresponding to a definition of $PM_{6.5}$-PM_7 is used in Japan since its earlier introduction in 1972. Figure 1 schematically describes the relationships

between each of the size classes. Smaller size-classes are part of the respective next larger class. For aerosol emission sources, size distributions among the classes can often vary greatly. In ambient aerosol samples without influences from nearby sources, differences between TSP and PM_{10}/SPM can be assumed to be low, i.e., immission samples mainly consist of particles smaller than 10 µm (aerodynamic diameter).

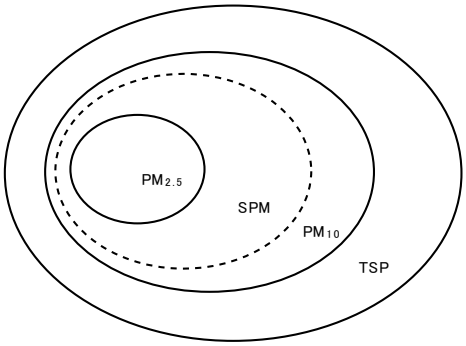

Figure 1. Size classes of atmospheric aerosols.

As aerosol sampling inlets, impactor and cyclone separators are the most prominent particle separation devices. These inlets make use of drag and inertial forces of particles to separate and deposit particles larger than their cut-off diameter on collection surfaces or containers. In an aerosol impactor, drag force on the particle, particle momentum, and the effective transit time across the impactor plate determine, whether a particle is impacts. The relevant effects can be combined in a dimensionless parameter called Stokes number:

$$St = \frac{\rho d_p^2 C V}{9 \mu W} \tag{1}$$

where ρ is particle density d_p is aerodynamic particle diameter V is velocity in the impactor jet, μ is air viscosity, W is jet diameter and C is the empirical Cunningham slip factor defined as:

$$C = 1 + \frac{\lambda}{d}\left[2.514 + 0.800 \exp\left(-0.55 \frac{d_p}{\lambda}\right)\right] \tag{2}$$

Stokes number is proportional to the ratio of particle stopping distance to half the jet diameter when a particle is injected into still air and can be interpreted as the ratio of particle relaxation time to the transit time through the impaction region. Impaction efficiency increases with growing Stokes number. For impactors with similar geometry critical Stokes numbers St_{50} corresponding to the cut-off diameter d_{50} are found to be nearly the same, even at different jet diameters or velocities. The cut-off diameter can thereafter be predicted using the critical Stokes number using

$$d_{50}^2 C = \frac{9\mu\pi n W^3 St_{50,round}}{\rho Q} \quad (3)$$

for round impactor jets. (Hering, 1995)

A Cyclone separator utilizes centrifugal force in a spinning gas stream rather than the relaxation of accelerated particles. Centrifugal force of a particle with the mass m_p and tangential velocity v_θ (≈inlet velocity) at a radius r is given as $m_p v_\theta^2 / r$. Turbulence and complexity of flow fields in cyclone separators has, however, lead to semi-empirical formulae for the prediction of cut-off diameters , separation efficiencies and cyclone dimensions. (Lidén & Gudmundsson, 1996)

3.1.2. Optical Properties of Aerosol Particles

In particle-polluted air, scattering is the most important light attenuation process, followed by absorption. Scattering and absorption also occurs on very small particles such as gas molecules for which prominent examples are Rayleigh scattering, giving the sky its blue color because of it higher efficiency at short wavelengths, or molecular absorption spectra, coloring air polluted with NO_2 in a brownish tint. The strongest light absorbing particles are black carbon, main component of soot, hematite (Fe_2O_3) and aluminum oxide (Al_2O_3) while the most important light scattering particles are cloud droplets and hydrometeors. For modeling light extinction in aerosols, extinction coefficients for both absorption and scattering need to be calculated with

$$\epsilon_{a,\lambda} = \sum_{i=0}^{N_B} n_i \sigma_{a,i,\lambda} \qquad \epsilon_{s,\lambda} = \sum_{i=0}^{N_B} n_i \sigma_{s,i,\lambda} \quad (4)$$

respectively. N_B is the number of size bins, n_i the number concentration of aerosol particles of a given size, and $\sigma_{a,i,\lambda}$ and $\sigma_{s,i,\lambda}$ are the effective absorption and scattering cross sections of a single aerosol particle which are given by

$$\sigma_{a,i,\lambda} = \pi r_i^2 Q_{a,i,\lambda} \qquad \sigma_{s,i,\lambda} = \pi r_i^2 Q_{s,i,\lambda} \quad (5)$$

for spherical particles, where πr_i^2 is the actual aerosol cross section (cm^2), $Q_{a,i,\lambda}$ (dimensionless) is the single-particle absorption efficiency, and $Q_{s,i,\lambda}$ is the single particle scattering efficiency. The absorption and scattering efficiencies which are functions of the particle's complex index of refraction m_λ and depend on wavelength and the size parameter

$$x_{i,\lambda} = \frac{2\pi r_i}{\lambda} \quad (6)$$

which can be approximated for a small particle ($x_{i,\lambda} < 0.1$ or $d_{i,\lambda} < 0.03\lambda$) in the Rayleigh-regime as Tyndall absorber or scatterer as

$$Q_{a,i,\lambda} \approx \frac{2\pi r_i}{\lambda}\left[\frac{24 n_\lambda \kappa_\lambda}{\left(n_\lambda^2+\kappa_\lambda^2\right)^2+4\left(n_\lambda^2-\kappa_\lambda^2+1\right)}\right] \tag{7}$$

where n is the real part of the refractive index (scattering) and κ the imaginary part (absorption). For a particle in the Mie-Regime ($0.1 < x_{i,\lambda} < 100$ or $0.03 \cdot \lambda < d_i < 32 \cdot \lambda$) with boundary conditions for homogenous spheres the expressions

$$\begin{aligned} \mathrm{ru^s} &= \frac{1}{\mathrm{k}}\sum_{n=1}^{\infty}(-i)^n \frac{2n+1}{n(n+1)} \;\; \mathrm{a_n}\xi_n(kr)P_n^1(\cos\theta)\cos\phi \\ \mathrm{rv^s} &= \frac{1}{\mathrm{k}}\sum_{n=1}^{\infty}(-i)^n \frac{2n+1}{n(n+1)} \;\; \mathrm{b_n}\xi_n(kr)P_n^1(\cos\theta)\sin\phi \end{aligned} \tag{8}$$

for the potentials u and v are obtained where ξ_n are Hankel functions, P_n^1 are associated Legendre polynomial and the coefficients a_k and b_k are complex functions which are formally obtained as

$$\begin{aligned} a_n &= \frac{\psi_n'(y)\psi_n(x) - m\psi_n(y)\psi_n'(x)}{\psi_n'(y)\xi_n(x) - m\psi_{n(y)}\xi_n'(x)} \\ b_n &= \frac{m\psi_n'(y)\psi_n(x) - \psi_n(y)\psi_n'(x)}{m\psi_n'(y)\xi_n(x) - \psi_{n(y)}\xi_n'(x)} \end{aligned} \tag{9}$$

with functions ψ *and* ξ expressed, for example, as linear combinations of Bessel functions and Neumann functions. In the far field solution the expressions for u and v are approximated with reduced Hankel functions as

$$\begin{aligned} ru^{\mathrm{s}} &\approx -\frac{ie^{-\mathrm{ikr}}\cos\phi}{k}\sum_{n=1}^{\infty}\frac{2n+1}{n(n+1)}\;\mathrm{a_n}P_n^1(\cos\theta) \\ \mathrm{rv^s} &\approx -\frac{ie^{-\mathrm{ikr}}\sin\phi}{k}\sum_{n=1}^{\infty}\frac{2n+1}{n(n+1)}\;\mathrm{b_n}P_n^1(\cos\theta) \end{aligned} \tag{10}$$

The flux density of the scattered light in an arbitrary direction is given by

$$F(\theta,\phi) = \frac{F_0}{k^2 r^2}\left[i_2(\theta)\cos^2\phi + i_1(\theta)\sin^2\phi\right] \tag{11}$$

where F_0 represents the incident flux density i_1, i_2 are intensity functions for the perpendicular and parallel components, respectively. Total flux of the scattered light integrated over all angles is therefore

$$f = \int_0^{2\pi}\int_0^{\pi} F(\theta,\phi) r^2 \sin\theta \, d\theta d\phi \tag{12}$$

where $\sin\theta \, d\theta \, d\phi$ is the differential solid angle $d\Omega$, and $r^2 \, d\Omega$ gives the differential area. The scattering cross section is thereafter given by

$$\sigma_s = \frac{f}{F_0} = \frac{\pi}{k^2}\int_0^{\pi}\left[i_1(\theta) + i_2(\theta)\right] sin\theta d\theta \tag{13}$$

resulting in the scattering efficiency of a sphere as

$$Q_s = \frac{\sigma}{\pi a^2} = \frac{1}{x^2}\int_0^{\pi} [i_1(\theta) + i_2(\theta)]\, sin\theta d\theta \tag{14}$$

With the help of some properties of Legendre polynomials which can be associated to the integral, the efficiency can be evaluated to yield

$$Q_s = \frac{2}{x^2}\sum_{n=1}^{\infty} (2n+1)(|a_n|^2 + |b_n|^2) \tag{15}$$

Finally, absorption cross sections and efficiencies can be obtained from the relations

$$\sigma_a = \sigma_e - \sigma_s,\ Q_a = Q_e - Q_s. \tag{16}$$

For absorbing spheres $m_{\lambda,r}$ and $m_{\lambda,i}$ represent real (refraction) and imaginary (absorption) part of the complex index of refraction $m_\lambda = m_{\lambda,r} - im_{\lambda,i}$.

For aqueous particles the absorption term can be neglected, unless the particles become very large (i.e. hydrometeors) extinction efficiencies equal scattering efficiencies Q_{ext} plotted in Figure 2. For small particle sizes of a few hundred nm, efficiencies get very small. For different wavelengths, the x axis shifts slightly, which can cause colored (reddish or bluish) appearance of light scattered from or transmitted through aerosols, if the particle size distribution is sufficiently narrow. A moderate increase in refractive index, e.g., m_r = 1.50 (dashed line) shifts the curve towards smaller particles. (Bohren & Huffman, 1983; Liou, 2002; Jacobson, 2005c)

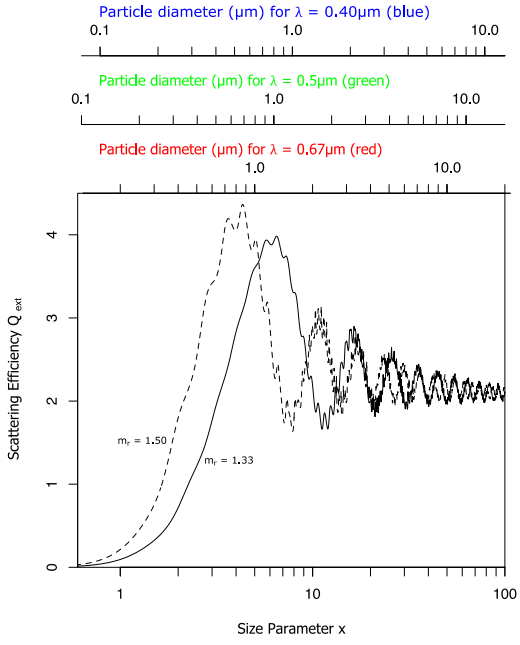

Figure 2. Scattering efficiency Q_{ext} for water spheres (solid line; m_r = 1.33) and spheres with a refractive index of m_r = 1.50 (dashed line).

Scattering efficiency and angular patterns of scattered light can be analyzed to measure

particle size in a light scattering single particles (particle counters) or as linear combination of a series of size bins, to obtain a particle size distribution (MIE scattering particle size distribution analyzer). Scattering parameters, in particular the scattering efficiencies depend on the complex refractive index m_λ of the scattering particles. For droplets consisting of water or aqueous salt and acid solutions within the MIE-Regime which can be expected to display m_λ of 1.33-1.5, the angular scattering pattern does not show significant variation caused by changes in the refractive index. Plots of normalized scattering patterns calculated with a Mie Scattering Calculator (Prahl, 2012) in Figure 3 coincide almost perfectly for refractive indices of 1.33 (solid line - pure water) and 1.5 (dashed line). Uncertainties in refractive indices due to changing concentrations in solutions have therefore low influence on particle size measurements using light scattering patterns. Scattered light intensity, however, does vary and may in some cases have an influence on size distribution details.

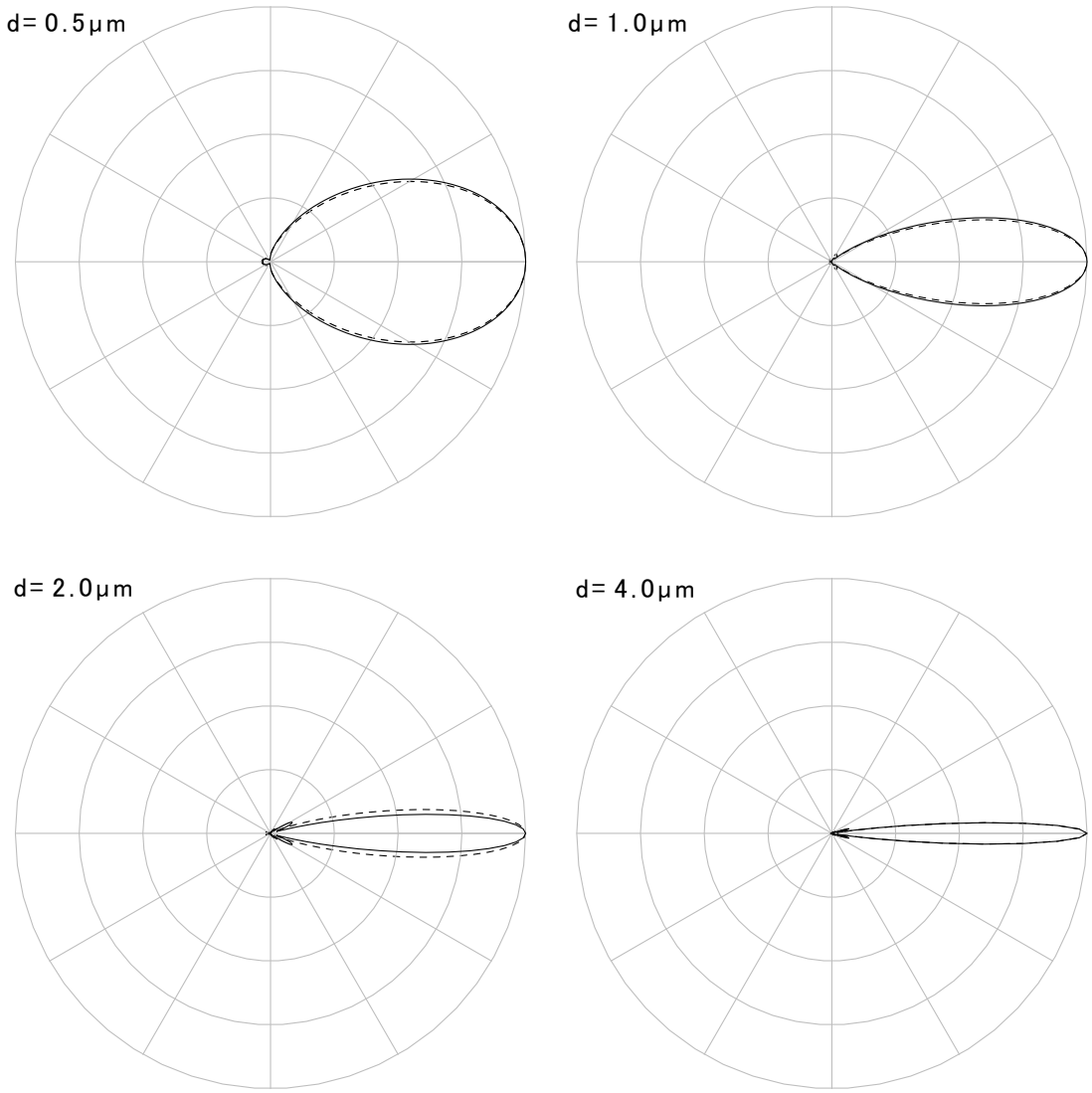

Figure 3. Normalized predominantly forward scattering patterns (unpolarized, linear scale) for different small particles of various diameters with refractive indices of 1.33 (solid line) and 1.50 (dotted line) at λ = 670nm.

3.2. Health Considerations

Fine dust particles suspended in air are absorbed through breathing into the human body. Depth of particle penetration is dependent on particle size. Particles with diameters of around 5 to 30 µm are already deposited in the nose-throat region of the respiratory tract because of high air velocities and bends in the upper air paths – for large diameters almost completely, for smaller diameters only partially.

Small particles in the range of 10 to 20 µm can penetrate as deep as the bronchial tubes and trachea and precipitate there due to low air speeds. Particles smaller than 10 µm

can reach the alveoli (air sacs) where they can, through a long residence time of about two months (Birgersson, et al., 1988), impair regular lung function. In addition, particulate matter can induce inflammations or even absorbed into the blood (Neuberger, et al., 2004). Figure 4 shows the penetration depths of the different particle-size fractions into the human body.

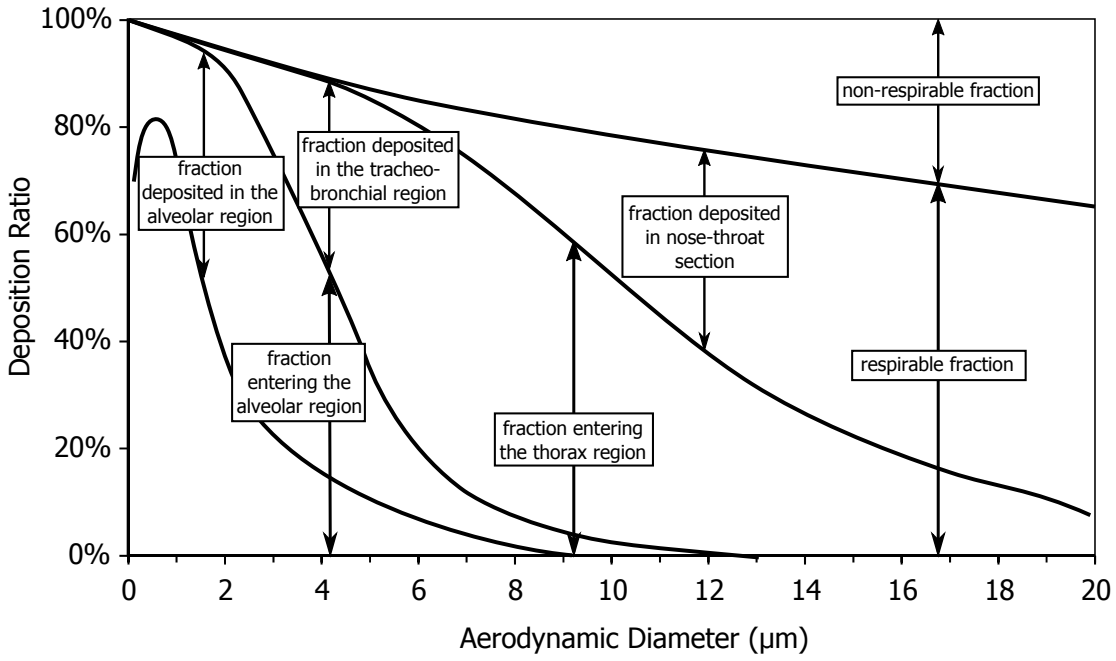

Figure 4: Respirability of aerosols (Deutsche Forschungsgemeinschaft, 2012)

Correlations between particulate pollution and increase mortality have already been recognized in the 80s of the last century. In the last decades, a multitude of epidemiological studies has verified negative impact on human health. These include very extensive studies in which daily mortalities in the 20 largest cities of the USA over a period of 7 years were included (Daniels, et al., 2000), as well as numerous locally confined investigations.

A major recognition found in all studies is that exposure to elevated particulate matter levels can lead to adverse effects on human health. The report „Health aspects of air pollution [...]“ (World Health Organization, 2003) supplies a short summary on the spectrum of impacts from exposure to particulate matter on human health.

Table 2. Health effects of particulate matter exposure (World Health Organization, 2003)

Effects of short-term exposure	Effects of long-term exposure
pneumonia	increase of respiratory problems
respiratory diseases	reduction of lung function
cardiovascular diseases	increase of chronic pulmonary diseases
increased use of medication	
higher number of hospital admissions	reduction of life expectancy through
increase in mortality	cardiovascular diseases and lung cancer

3.3. Bio-Aerosol Emissions

Biological material of various origins is found in all particle size fractions of atmospheric aerosols. Bio-aerosols can both be emitted naturally as well as in the influence of human activities. Spores and pollen are naturally designed for transport by wind, and are efficiently emitted by the fungi or wind-pollinating plants. Also bacteria and other microorganisms can become airborne as particles and can be found in cloud water samples. (Bauer, et al., 2003) Erosion and uplift of soil, for example can strongly be intensified by traffic on paved and unpaved roads. Particles including soils and leaves deposited the road surface are transported, ground down to diameters of at least 2 µm and re-suspended by the traffic. (Patra, et al., 2008) Biological material, especially pollen, which originally are relatively large particles around 30 µm, when they are undamaged, can be disintegrated by exposure to moisture or water (Johri & Vasil, 1961) or by traffic-related mechanical stress and release small granules of 2.5-4 µm (Motta, et al., 2006). A variety of organic substances are also set free as particulate matter from combustion of leaves (Schmidl, et al., 2008) and wood (Caseiro, et al., 2009; Elsasser, et al., 2013). Particularly fine particulate matter containing protein material has a potential, though highly dependent on susceptibility of individuals, to cause significant health effects through allergic reactions.

3.4. Emissions from Pyrotechnics

Pyrotechnics have been reported to release significant amounts of very fine particulate matter in the range of a few 100 nm in diameter. (Wehner, et al., 2000; Dutschke, et al., 2011) It is also known, that the majority of pyrotechnics also produce very large particles of dispersed molten combustion residue with diameters up to the millimeter range as fallout, apart from un-combusted structural parts. Also, gaseous emissions have been investigated, especially in respect to items for indoor use. (Dutschke, et al., 2009) Metals and other elements from compounds used specifically in pyrotechnics can

be readily found at elevated levels in atmospheric aerosol during and firework consumption episodes. (Drewnick, et al., 2006; Wang, et al., 2007; Sarkar, et al., 2010) Even residual perchlorate oxidant has been found in such aerosols. (Shi, et al., 2011)

3.4.1. Base Combustion Products

Pyrotechnic compositions consist of an oxidant/fuels system which, with the exception of those displaying explosive combustion, generally sustains its combustion in a complex equilibrium of heat-conduction, radiative heat transfer, decomposition of the solid or molten oxidant and fuel, and often spatially varying combustion processes involving condensed phase and vapor phase reactions. An example of ammonium perchlorate shown in Figure 5 illustrates the different processes of oxidant vaporization and decomposition, as well as binder decomposition and diffusion flames occurring during composite combustion. (Vandenkerckhove & Jaumotte, 1961; Jacobs & Whitehead, 1969) Many composites further involve liquid and solid phase processes of oxidant and catalyst compounds taking part in or slowing down binder or oxidant decomposition. Table 3 summarizes major particulate and gaseous emissions found in exhaust from pyrotechnics' components.

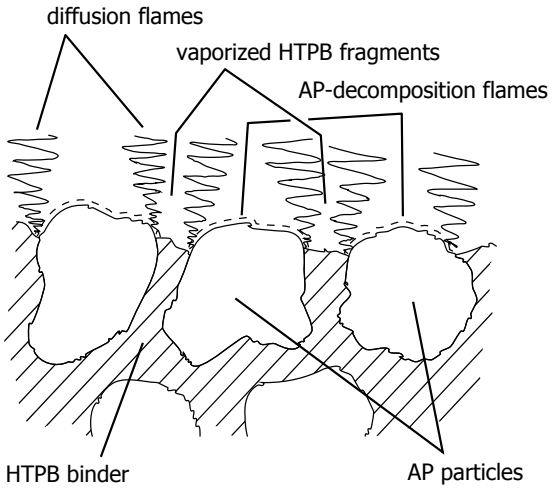

Figure 5. AP/HTPB Composite combustion flame structures near the composite surface.

Table 3. Emissions originating from various components used in pyrotechnic devices

Pyrotechnics' Component	Particulate Emissions	Gaseous Emissions
black powder	K_2SO_4, K_2CO_3, $K_2S_2O_3$, K_2S, soot	CO_2, CO, H_2O, H_2S, COS
potassium perchlorate and chlorate base compositions	KCl, K_2CO_3, traces of perchlorate	CO_2, CO, H_2O, HCl
ammonium perchlorate base compositions	HCl mists at high humidity, NH_4Cl	H_2O, CO_2, CO, HCl, NH_3
flame coloring additives	$BaCl_2$, $CuCl_2$, NaCl, $SrCl_2$	CO_2, NO_x
spark generating additives and catalysts	MgO, $MgCl_2$, Al_2O_3, TiO_2, Fe_2O_3, $FeCl_3$, Cr_2O_3	

The most commonly used explosive composition in fireworks is black powder (gunpowder). With a composition of 75% potassium nitrate, 15% charcoal and 10% sulfur it is also known for producing a tremendous amount of smoke emissions and solid residue in launch barrels as well as H_2S which is responsible for the characteristic smell of its plume. (von Maltitz, 2004) Compositions based on potassium chlorate and perchlorate represent the *classic* palette of stars producing brilliant high temperature colored flames, but also are known to produce significant amounts of visible smoke from partially vaporized KCl and HCl. Compositions based on potassium nitrate and organic nitrates (nitric acid esters) are of interest, because of safety (sensitivity and incompatibility of chlorates with impurities) and environmental (stability of perchlorate) aspects (Shi, et al., 2011), but mostly have not succeeded in reaching the performance levels displayed by compositions with chlorine based oxidants. (Shimidzu, 1981)

Compositions based on Ammonium perchlorate (AP) do not produce aerosol particles during combustion and find use with hydroxyl-terminated poly-butadiene as binder in rocket propellant applications, where visually obscuring plumes and visible trajectories are undesirable. Combustion products of AP/HTPB base composites only contain gaseous products like CO_2, H_2O and HCl of which only the latter can cause aerosol formation in combination with high humidity conditions. (Kubota, 2004) AP is used as oxidant in some blinking compositions, but has only found minor presence in regular stars, mostly because of its incompatibility with black powder-like compositions used in priming (igniting) compositions and lifting charges. Nitrate present in black powder reacts with ammonium to form ammonium chloride, which due to its hygroscopic nature absorbs water vapor from ambient air and causes stars to become unignitable over time. (Shimidzu, 1981) The fact that it produces virtually no fallout particles as they are found in compositions using potassium salts can be of interest in some applications.

3.4.2. Products from Additives

In solid rocket boosters for astronomical applications, metal (Al) additives increase energy output of the smoke-free AP/HTPB base composition but at the same time cause the exhaust to form thick white clouds. In pyrotechnics fine particulate matter is produced not only from metal powder additives which produce characteristic spark effects, but also from flame coloring compounds, which are transformed to metal chlorides volatile in the high temperature flames. Metal chloride molecules of BaCl, CuCl, SrCl as well as Na-atoms emit their characteristic emission spectra when they transition from an excited state. (Shimidzu, 1981; Kosanke & Kosanke, 2004) Except CuCl, metal chlorides are mostly present at higher oxidation states ($BaCl_2$, $SrCl_2$, NaCl) than the molecules and atoms responsible for light emission and rapidly condensate at high temperatures (boiling points over 1500 K (Perry, 2011)) through homogeneous nucleation. Thereby aerosol particles with diameters in the range of up to a few 100 nm are formed at high number concentrations.

3.4.3. Aerosol Formation

Aerosol particles are formed from gas molecules in a nucleation process. Molecules aggregate to a cluster to form small liquid drop. If the cluster is large enough and exceeds a critical diameter, it becomes stable and can grow further by condensation. If the particles are generated without a pre-existing surface the process is called homogeneous nucleation. The process can be dramatically aided by an existing particle surface, which is then called heterogeneous nucleation. In case of particle formation from the volatile metal chlorides, a homogeneous nucleation process can be assumed, which results in the observed high concentration of particles in the 100 nm scale. Production rate of particles can be predicted based on classical nucleation theory, which derives homogeneous and heterogeneous nucleation rates from

$$\Delta G = 4\pi r_p^2 \sigma_p - \frac{4}{3}\pi r_p^3 \rho_p \frac{RT}{m_q} \ln S_q \tag{17}$$

which describes the change in Gibbs free energy during nucleation of a cluster, which is primarily affected by surface tension σ_p of a particle with radius r_p and density ρ_p, and by the saturation ratio S_q which is the partial pressure of the gas divided by its saturation vapor pressure over the particle surface. Work that needs to be done against surface tension to enlarge the particle decreases with particles size and above a critical size, the particle can become stable. The critical radius can be found by setting

$\Delta G/\mathrm{d}r_p = 0$ which is

$$\frac{\Delta G}{dr_p} = 8\pi r_p \sigma_p - 4\pi r_p^2 \rho_p \frac{RT}{m_q} \ln S_q = 0 \tag{18}$$

which can be solved to give the critical radius:

$$r_c = \frac{2\sigma_p m_q}{\rho_p RT ln S_q} \tag{19}$$

Homogeneous nucleation rate after classical theory is expressed as

$$J_{\mathrm{hom}} = 4\pi r_c^2 \beta_x Z_n N_x \exp\left(-\frac{\Delta G^*_{\mathrm{hom}}}{k_b T}\right) \tag{20}$$

where

$$\Delta G^*_{hom} = \frac{4}{3}\pi r_c^2 \sigma_p \tag{21}$$

k_b is Boltzmann's constant, N_x is the number concentration of the nucleating gas x,

$$\beta_x = N_x \sqrt{\frac{k_b T}{2\pi M_x}} \tag{22}$$

is the number of gas molecules striking a unit surface area per second and $N_x \exp(-\Delta G^*_{\mathrm{hom}}/k_b T)$ is an equilibrium concentration of nucleated clusters of critical radius r_c. (Dahneke, 1983; Jacobson, 2005b) When high supersaturation ratios are reached, homogeneous nucleation not only reaches higher nucleation rates through more favorable $\Delta G^*_{\mathrm{hom}}$, but also can produce particles starting at a smaller critical radius r_c. Final particle size distributions are further influenced by growth by condensation and coagulation processes. Numerous studies have produced a series of numerical calculation models (Yu, et al., 2008; Zhou & Chan, 2011), of which some are made available online (Prakash, et al., 2003).

3.4.4. Hygroscopic Growth

Hygroscopic growth starting from solid particles represents a heterogeneous nucleation process which requires little supersaturation states to start aqueous phase formation. Further, the vapor pressure of H_2O for hygroscopic substances at which aqueous phase formation begins is usually given as the vapor pressure over is saturated solution. This vapor pressure is expressed as deliquescence relative humidity (DRH) or critical relative humidity values, which are tabulated for many salts. The Kelvin effect increases vapor pressure of very small particles by curvature of the particle surface but plays only a small role, as soon as the particle has grown by uptake of water. Reduced vapor pressure over aqueous solutions of electrolytes (mostly metal chlorides in this study) causes particle growth for relative humidity conditions above DRH. Once formed

aqueous solutions also strongly attract hygroscopic gases such as HCl vapors, which generally are present in exhaust from pyrotechnics. The hygroscopic metal chloride particles formed by homogeneous nucleation therefore grow significantly in size at high relative humidity and display high light scattering efficiencies as thick clouds after growth.

4. Measurement of Protein Content in Aerosol

4.1. Protein Content in Aerosol

Free and protein amino acid content is known to be present in atmospheric aerosols (Milne & Zika, 1993). Proteins in particulate matter have mostly been investigated with respect to allergies, which react to specific proteins present in certain types of primary biological aerosol particles (PBAPs). Previous studies mostly concentrate on allergen proteins as tracer compounds for specific source types such as allergens found in pollen (Yasueda, et al., 1983) and its fragments (Swoboda, et al., 2004), as well as dusts from food processing (Bogdanovic, et al., 2006), pet (Holmquist & Vesterber, 2002), residential (Custovic, et al., 1999) and road dust (Miguel, et al., 1999). Abundance of primary cellular and protein particles from direct emission into the atmosphere have also been reported (Jaenicke, 2005). Measurement of total protein content has only been performed in few aerosol studies, e.g., from atmospheric aerosols (Franze, et al., 2003) or residential aerosols (Armstrong, et al., 2001).

Quantification of protein amino acids content in aerosol particles fractionated by a high-volume cascade-impactor represents a new, more general indicator of PBAPs including information on its distribution over aerosol size fractions. Acquired amino acid compositions are analyzed in source-receptor models. Though not nearly as specific as immunologic detection of allergen proteins, analysis of proteins by amino acid content can provide enough multidimensional data to attribute protein content to aerosol source groups. Sampling periods covering a whole year provide new insight into seasonal variations of size distribution and composition of protein matter in the urban atmosphere.

4.2. Methods

Aerosol was sampled and analyzed at a suburban sampling site near Shibuya using a high volume aerosol sampler equipped with an Anderson type cascade impactor which separated aerosol samples into five size fractions of >7 μm, 7-3.3 μm, 3.3-2 μm, 2-1.1 μm and <1.1 μm at a flow rate of 566 $L \cdot min^{-1}$. Sampling periods from one to two weeks covered a whole year ranging from February 2009 to January 2010 and yielded tens to hundreds of mg of PM per filter. PM load per filter was large enough to perform analysis of protein content by hydrolysis and subsequent analysis of the yielded amino acids. Concentration profiles were collected over a period of approximately one year, providing

insight into seasonal variations of protein content in urban ambient aerosol. Collection of amino acid emission profiles enabled estimation of source contributions to the measured ambient aerosol concentrations using a receptor model. Source apportionment was applied to the amino acid concentration and source profiles with a receptor model called Chemical Mass Balance (CMB) Model (United States Environmental Protection Agency, 2005) to estimate contributions from various aerosol sources to total aerosol mass concentrations in each size fraction. The model is based on an effective-variance least squares method accounting for uncertainties immanent to source types or groups and receptor measurements and returns linear combinations of source profiles, which best fit the concentration profiles measured at a receptor site. It is used as a planning tool in aerosol source inventories for state implementation plans in the USA as well as aerosol research in Europe (Puxbaum, 2011). The source profiles for application in the CMB model are required to display linear independent species concentration sets among each other for successful apportionment. Similar profiles need to be combined to group profiles to avoid co-linearity problems.

4.2.1. Sampling Aerosol

For gravimetric and chemical analysis of aerosol samples, particles need to be collected on a suitable media for later analysis. One of the most common media is a fiber filter with low interferences regarding the analysis to be performed. Pallflex Tissuquartz™ filters offer low moisture pickup and superior chemical purity as a filter consisting of binder-free pure quartz (Pall Life Sciences, 2002). Further, it can easily be cut with high precision and negligible sample loss using punching irons or roller cutters (Abe & Puxbaum, 2006). It practically does not interfere with rigorous extraction reactions methods using concentrated mineral acids.

Atmospheric aerosols are generally sampled using inertial separation of particle sizes to define the sampled particle size range. Total Suspended Particulate (TSP) is an exception defining no upper limit for particle size in terms of its design, but airborne particulates which can escape the immediate vicinity of the ground rarely exceed about 60µm. (Jacobson, 2005b) There are three types of such separation devices, which are cyclone, impactor, and mobility analyzer. All of them can be designed to feed at least the fraction of aerosol particles which are smaller than their cut-point diameter through an online analysis device or filter for later analysis. The load of large aerosol particles, they can efficiently separate, however, decreases in the mentioned order and need to be

considered for proper application.

A high volume version of the Anderson type cascade impactor (AH-600F, Shibata Scientific Technology) with 4 impactor stages and a filter stage divided aerosol samples into five size fractions (>7, 7-3.3, 3.3-2, 2-1.1 and <1.1 µm) at a flow rate of 566 L/min. Sampling time was generally 1 to 2 weeks in order to collect enough aerosol mass for analysis. Perforated Pallflex® Tissuquartz™ filters for the cascade-impactor and backup-filters (AHQ-630: ø=30 cm; AHQ-640 8×10") were purchased from Tokyo Dylec Corp. Filters were weighed in a humidity- and temperature-controlled dust-free tent. Humidity was held at 50% RH by a Yamato Scientific IG400 constant humidity chamber which was operated with the open chamber door connected to the tent. Filters were allowed to equilibrate at the pre-set humidity conditions for 24 hours before weighing and an average was calculated of five weighs. Room temperature was held constant at 20°C by regular air conditioning. Filters were weighed before and after sampling without folding or cutting on a custom large weighing dish attached to a standard analytical balance (readability d = 0.1 mg) with a modified weighing chamber (Figure 6). Until all weighing had finished filters were separately packed without folding in PE-plastic bags and stored only loosely stacked in a cardboard case for transport. This minimized losses through filter crumbling and particle transfer from filter to plastic bag surfaces.

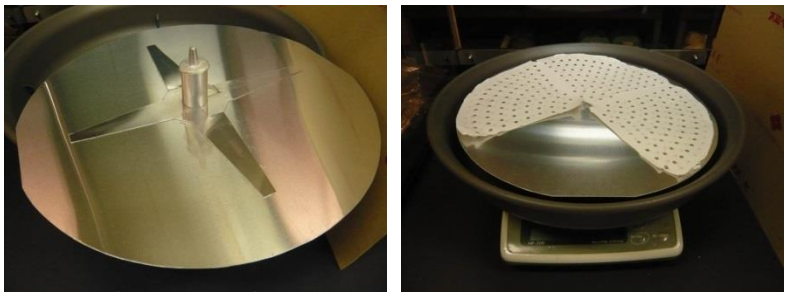

Figure 6 Custom aluminium weighing pan (bottom side) and filter on analysis balance with modified weighing chamber (filter already cut; top lid not attached).

4.2.1.1. Filter Load/Unload Procedures

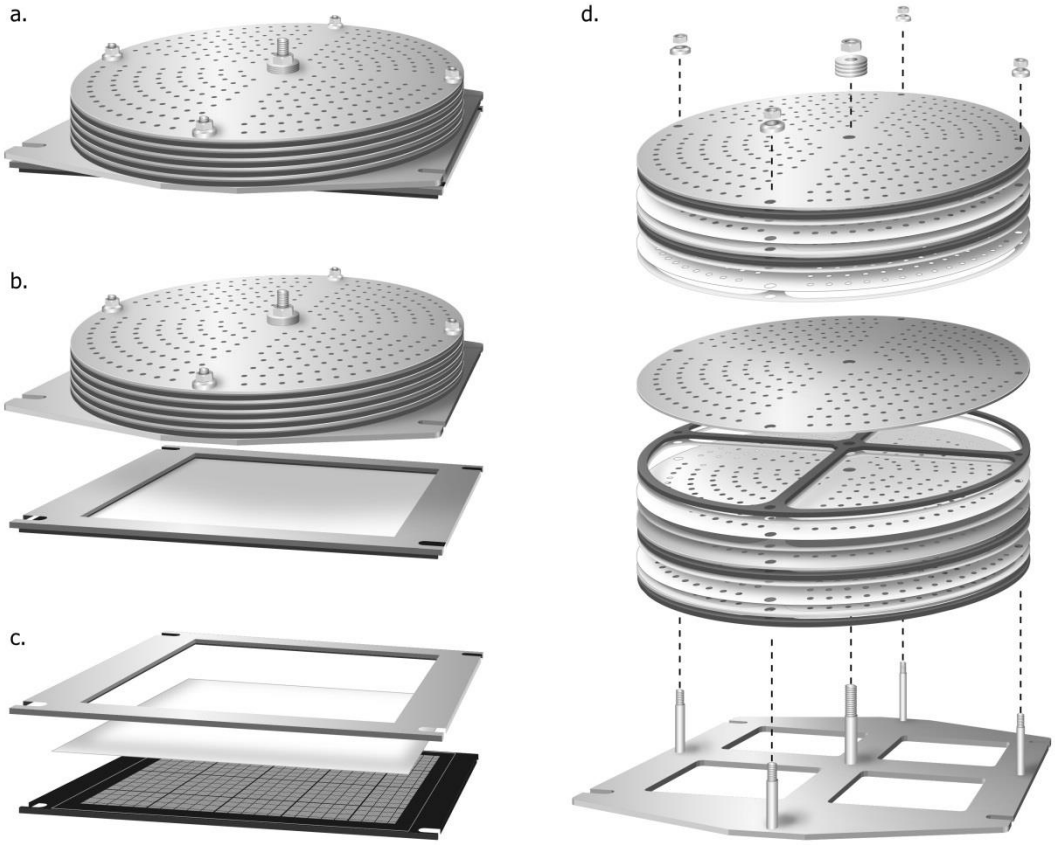

Figure 7. AH-600F aerosol sampler: a. complete assembly; b. cascade impactor and backup filter holder; c. explosion view of backup filter holder; d. explosion view of the cascade impactor assembly.

The AH-600F aerosol sampler consists of four impactor stages and a backup filter stage for the fine aerosol fraction. Figure 7 shows the components of the aerosol sampler's cascade impactor and backup filter holder. Filter exchange is most conveniently performed on a table but can also be performed on the floor if the area is cleaned sufficiently and only requires little more than 1 m^2 of space. Wind and dust need to be avoided as best as possible to prevent filter damage and contamination. All operations are performed wearing nitrile gloves. Nozzle/Impactor-plates are cleaned swiftly during filter exchange by wiping with clean laboratory paper cloths and some distilled water.

The cascade impactor is installed stacked on top of the backup filter holder on the aerosol sampler (a.). The whole assembly of impactor and filter holder can be detached from the aerosol sampler and is quickly taken to the clean workspace. The impactor is removed from the backup filter holder (b.). The backup filter is only laid in between the

top and bottom part of the filter holder and care must be taken to prevent the assembly from falling apart because the assembly cannot be secured by screws due to space limitations (c.). The filter can be quickly replaced with a single pair of tweezers. An explosion view of the cascade impactor parts (d.) shows the five stages, each consisting of a filter stacked between two Teflon® liners, a rubber spacer and the corresponding nozzle/impactor plates.

To prevent damage to and contamination of the perforated filters and liners, handling of these parts with two pairs of tweezers needs to be performed following specific loading (Figure 8) and unloading (Figure 9) procedures.

Filter loading procedure (Figure 8):

a. Start with the spacer of the impactor base or previous stage set in its final position. The nozzle/impactor plate is placed at a slightly rotated angle on top of the base to only let the center screw protrude. Bottom liner, filter and top liner are placed on the plate and aligned properly (only touch with the tweezers).
b. Turn the plate to align with the four remaining screws and carefully move the whole assembly down.
c. Install the rubber spacer on top of the assembly (touch with gloves).
d. Repeat a. through c. until the whole impactor is assembled.
e. Fix the whole assembly with nuts and washers (M7 for the peripheral screws and M10 for the center screw).
f. The assembled impactor is ready for installation on the sampler.

Filter unloading procedure (Figure 9)

a. Extract the whole stack of impactor stages from the impactor base and turn it upside down.
b. The impactor parts are removed one by one from the stack. When exchanging filters, these parts can be directly re-used for re-assembly on the now free impactor base following the filter loading procedure. It is also a good idea to swiftly clean the parts at this stage.
c. Store the sample filters without folding in properly labelled PE-bags and put them in a cardboard box for safe transport.

When exchanging filters, both procedures are performed simultaneously and impactor stages taken apart are immediately re-assembled with new filters on the impactor base.

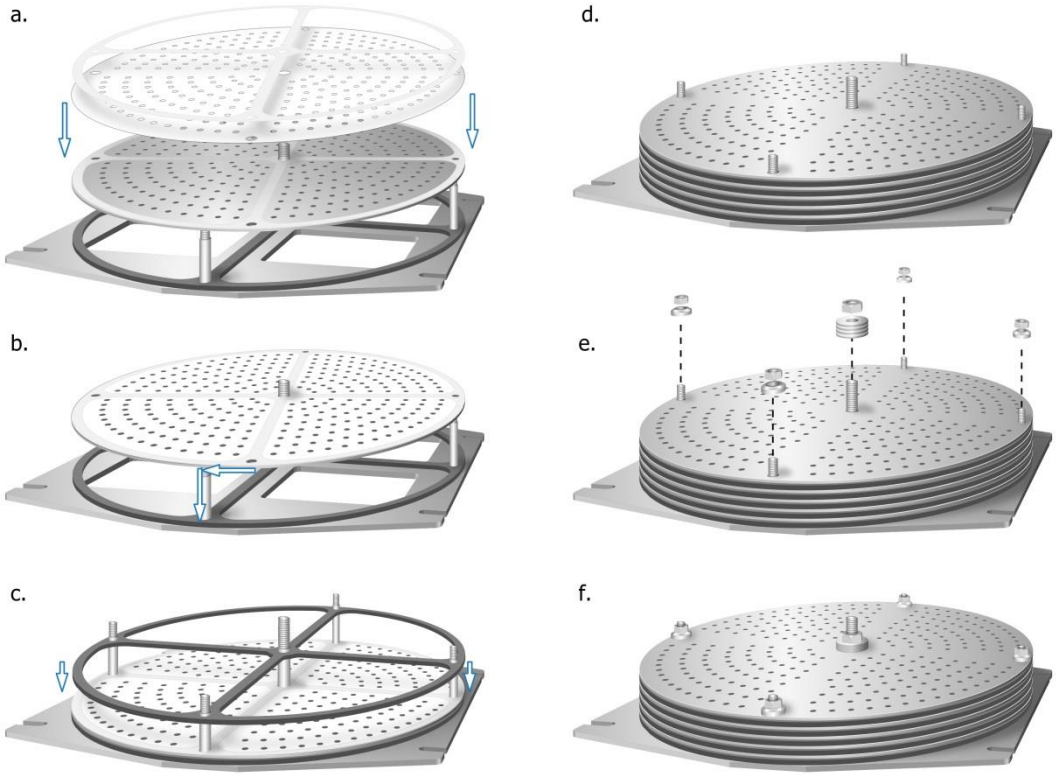

Figure 8. Filter loading procedure for the AH-600F cascade impactor

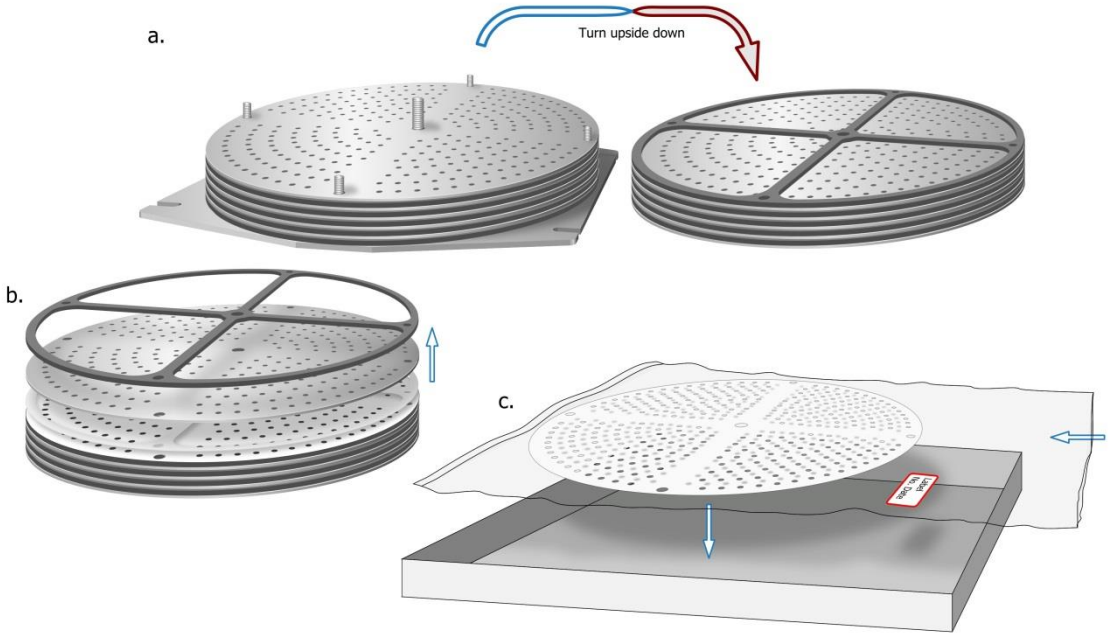

Figure 9. Unloading filters from the AH-600F cascade impactor.

4.2.1.2. Filter Weighing Procedure

Although the Pallflex Tissuquartz™ filters have low moisture pickup, the filters are conditioned, each on a separate grill, in a weighing chamber with temperature and humidity control at 25±0.5°C and 50±5% RH for 24 hours prior to weighing. This keeps humidity effects of filter and sampled aerosol particles at a minimum. Filters are carefully handled with a single pair of wafer-tweezers (with a flattened tip) pinching the filter at a sample-free space near one of the holes for the fixing screws or at the border area. The filters must not be touched even with nitrile-gloves on to avoid any contaminations. An average of five weighings is calculated for filters before, and after sampling. The weight increase of up to about 120 mg resembles the size fraction of particulate matter collected on each of the filters.

4.2.2. Aerosol Source Samples

One of the aims of this study is not only to measure protein content in ambient aerosol, but also to match amino acid concentration patterns with those of aerosol emission sources in order to find contributing sources using a chemical mass balance model (see Section 4.3.3). Therefore aerosol or bulk samples from a list of prominent aerosol sources most likely to contain protein matter in the urban region were collected and, if possible sampled with the size-selective high volume aerosol sampler. Direct sampling from aerosol sources generally results in sufficiently high yields of fine PM within reasonably short sampling times e.g., for kitchen exhaust. Sampling of fine particles from aerosols of many biological materials proved more difficult because they mainly consist of large particles, need to be transported and ground down on widespread areas such as roads (Patra, et al., 2008) to produce fine particles or only break down to fragments after ageing or exposure to high humidity conditions. Simple grinding experiments of bulk samples did not produce enough fine aerosol particles for re-suspension experiments with the aerosol-sampler and were analyzed from powdered bulk samples. Samples include leaves that can be re-suspended as biogenic material in road dust, skin an scales that can be emitted by abrasion, pollen from Japanese cedar (cryptomeria japonica). The latter two were either directly sampled in the field (pollen) or from re-suspended material with the cyclone separator attached to the cascade impactor.

For direct sampling of aerosols with heavy loads of large particles, a cyclone separator was designed with a similar geometry to the Sharp Cut Cyclone (SCC; cut-size $d = 2.5$ µm; flow rate: 16.7 l·min^{-1}) (BGI, inc., 2001; Kenny, et al., 2000) which is

implemented as a compact horizontally oriented pre-separator for PM2.5 samplers in routine analysis. Scale was chosen to approximately match a cut-size diameter for particles around 7 µm at a flow rate of 566 l·min^{-1} required by the high volume aerosol sampler. According to the semi-empirical Equation (23) (Lapple, 1951), the cut-point is given by a relationship of inlet flow velocity v_i and the inlet diameter b (=D_{in}).

$$d_{p,50} = 3 \cdot \sqrt{\frac{\mu \cdot b}{2\pi \cdot \rho_p \cdot v_i \cdot N_e}} \tag{23}$$

With v_i proportional to the volume flow divided by the inlet nozzle cross section, the cyclone diameter was found to be 24cm after scale-up and change in cut-off diameter. Further the "neck" between the main body and collection cup was adapted to allow 150ml sample bins to be attached directly as well as the inner surfaces of the cyclone to be cleaned when the sample bin is detached. Original, calculated and final adapted dimensions of the cyclone are shown in Table 4 for the design variables shown in Figure 10a. Classic vertical orientation ensured proper separation and collection of large particles in the sample bin.

The adapted cyclone constructed of a 0.5 mm polycarbonate sheet was assembled with an inlet adapter that could be easily attached to the AH-600F high volume Anderson impactor as (Figure 10b.). Fine aerosol from sources emitting mostly large particles at high loads in the order of a few g·m^{-3} could be successfully sampled with the adapted cyclone attached.

a. b.

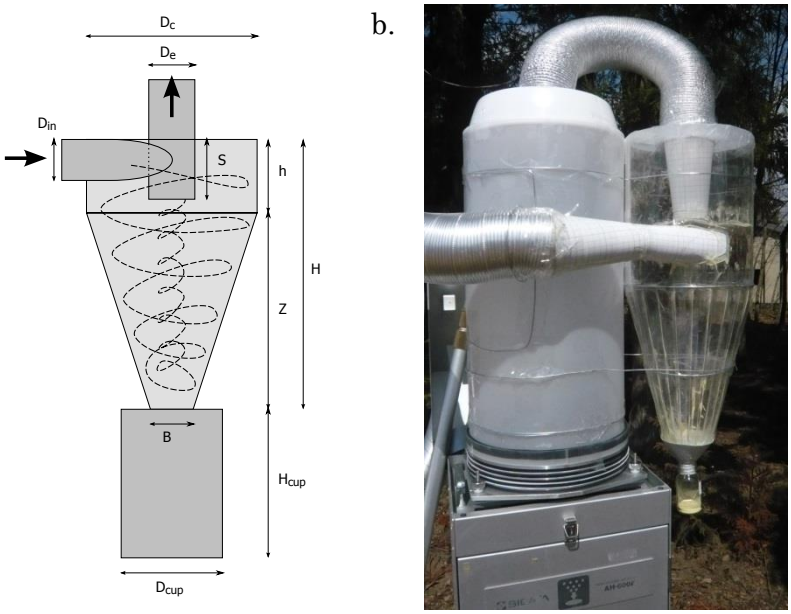

Figure 10 a. Schematic diagram of a cyclone separator and its dimensions. b. Cyclone assembly attached to the aerosol sampler with a suction duct (ø=10 cm) connected for field sampling of Japanese cedar pollen.

Table 4. Dimensions (in cm) of a BGI Sharp Cut Cyclone (SCC), calculated for a geometrically similar cyclone of 24 cm diameter which was adapted for a small sampling bin.

	D	Din	De	B	H	h	Z	S	Hcup	Dcup
Original SCC	3.495	0.24·D	0.27·D	0.25·D	1.58·D	0.43·D	1.13·D	0.35·D	0.87·D	0.635·D
Calculated	24	5.76	6.48	6	37.92	10.32	27.12	8.4	20.88	15.24
Adapted	24	5.8	6.5	10	41	10.3	27.1	8.4	4	12

4.2.2.1. Kitchen Aerosol Sampling

Kitchen aerosols were sampled from a kitchen (Itamae-Ryōri "Ebisuya", 2009) exhaust vent during lunchtime, where chicken cutlets and fried chicken were constantly prepared (Figure 11). Aerosols of oil and juices from meat or crumbing were discharged from the kitchen area through an unfiltered ventilation fan at a velocity of 3.0 ms^{-1} (⌀=30 cm; Flow rate~13 $m^3 \cdot min^{-1}$). The aerosol sampler withdraws only a small portion (0.566 $m^3 \cdot min^{-1}$) from this flow through a duct (⌀=10 cm) connected to the top nozzle plate of the Anderson-type impactor. Filters are unloaded from the impactor and filter holder after transporting the whole assembly back to the laboratory.

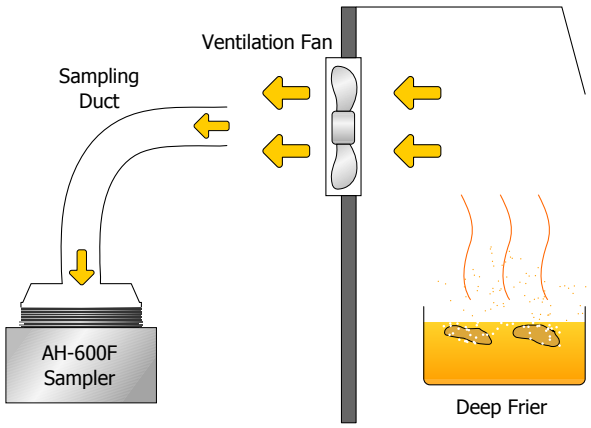

Figure 11. Schematic of the sampling-arrangement for kitchen-aerosols (from deep-frying): Around 10% of the unfiltered exhaust flow was collected by the aerosol sampler.

4.2.2.2. Pollen Sampling

Pollen samples were collected on several days in March 2010 from some seven blooming Japanese cedar of the Kumodōri variety planted at the plant nursery site of The University of Tokyo Chichibu Forest. From mere tapping, pollen is released in yellow dust clouds from the cedar blooms. To efficiently collect released pollen, air was collected directly from blooms at up to about 5 m height through an aluminum duct affixed to an extensible rod (Figure 12). Through gentle shaking and rattling, pollen dust clouds at concentrations of around 0.5 $g \cdot m^{-3}$ could be collected.

The cyclone separator proved to remove the large cedar pollen (20-30 µm) efficiently from the air stream, leaving behind about 0.1% (in the range of 1 µg·m^{-3}) of fine particulate matter to be collected by the cascade impactor. Particulate mass was concentrated in top and bottom fractions with particles >7 µm and <1.1 µm yielding about 5 mg sample per filter from 8 m^3 collected on a single sampling day.

Figure 12. Suction duct for sampling pollen from Japanese cedar blooms.

4.2.3. Analysis of Amino Acids in Hydrolysate

Protein matter was determined by analyzing amino acids by a reversed phase high-performance liquid chromatography (RP-HPLC) with fluorescence detection after hydrolysis and pre-column derivatization with 6-aminoquinolyl-N-hydroxysuccinimidyl carbamate (AQC-Reagent, Equation (24)) using the AccQ-Tag™ reagent kit from Waters, Milford. Hydrolysis with HCl (6 M, Wako) was performed on aerosol samples in order to dissolve the specimen and separate the solid filter matrix, which in case of the Tissuquartz™ filters remains un-digested.

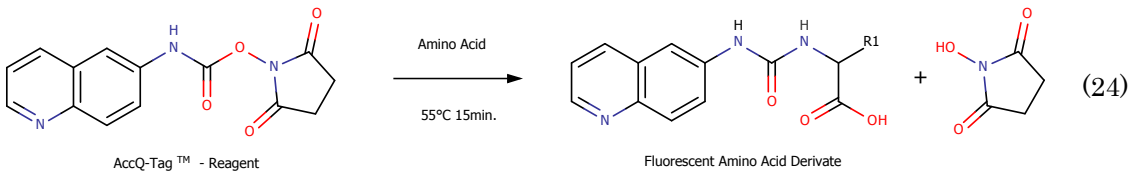

(24)

4.2.3.1. Hydrolysis Procedure

An eighth part of a filter was cut out of each filter using a roller cutter and divided into small pieces which then could be inserted into the hydrolysis tube. Aerosol particles

sampled on the perforated impactor-stage filters are clearly visible as darkened dots of aerosol-particles deposited through the orifices of the previous stage. When cutting and handling the filter material with tweezers and a roller cutter touching or cutting through these dots is avoided to minimize sample loss by depositions on the tools. For dot counts not dividable by 8 (Stage 1 and 3 with 300 dots), the sample is divided evenly by cutting one dot into halves (Figure 13).

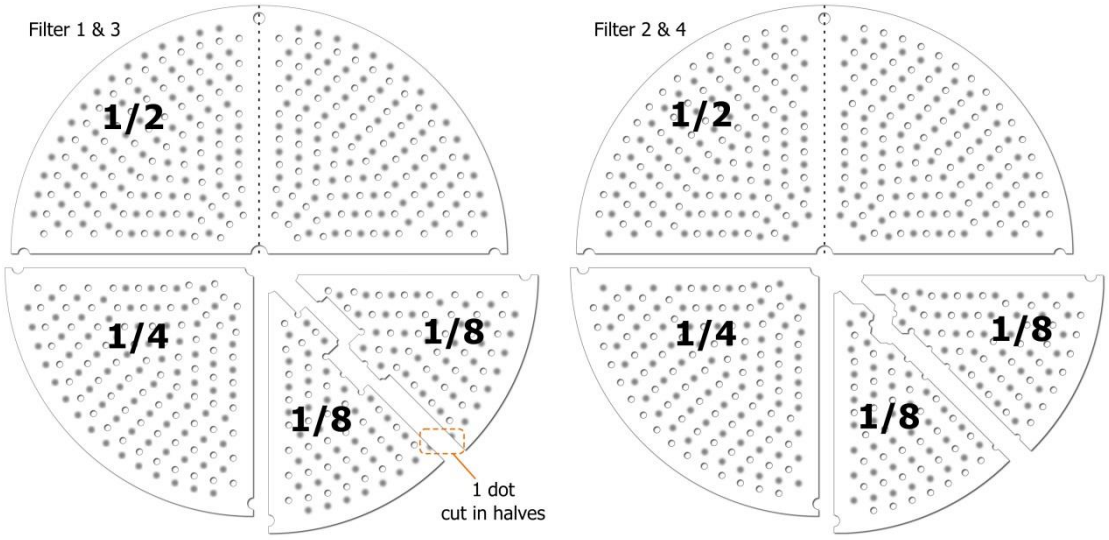

Figure 13. Filter cutting scheme for eighth part aliquots of aerosol samples on collection filters.

The remains of each filter which is divided in halves quarters or eighth parts are folded (half filter) or stacked (quarter and eighth part), so that sampled surfaces face each other and packed into sealable plastic bags for storage in the freezer. Any losses through sample transfer effects caused by mechanical contact can thereby be minimized. The eighth part for analysis is further cut in strips of about eight dots, after rim parts which were covered by the Teflon® liner during sampling have been cut off and discarded. Folded twice along the long side with the dots facing inwards to form sticks they are fed into a 19 ml hydrolysis tube (a Pyrex® sample tube equipped with a Teflon® valve and Viton® seals). Sample filled into the tube is then spiked with 10 µL (100 nmol) of n-leucine internal standard solution ($1 \cdot 10^{-5}$ mol·L^{-1}). After adding 6 mL of HCl (6 M), the liquid is cooled to its freezing point in an ethanolic cooling bath (cooled with dry ice or liquid N_2 in a cold finger). As soon as the liquid starts to solidify, the tube is evacuated and flushed with N_2 three times to remove O_2. Finally, the tube is thawed and evacuated. The sealed hydrolysis tubes are left to warm to room temperature and dried off with paper towels before they are set in a dry block bath at 110°C for the 24 hours

hydrolysis.

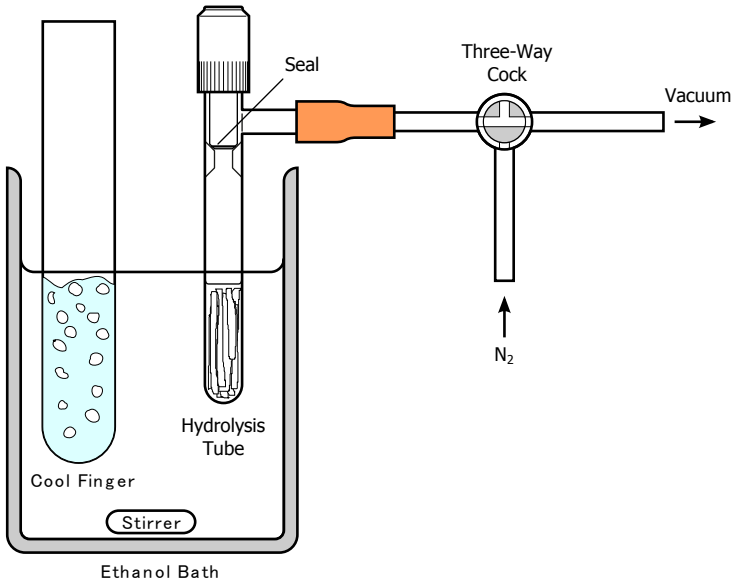

Figure 14. Flushing and evacuating the Hydrolysis Tube with N_2.

If the filter pieces are not lined up with left-over space going through from the bottom of the vial, bubbles can be trapped below the filter driving up the sample-filter into the head-space of the hydrolysis tube. In such a case parts of the filter lacks contact with the HCl solution or even dry out and thus proper hydrolysis will fail. Hydrolysis tubes should be checked for lifted filters, which can be put back to the bottom and straightened by careful (hot acid in evacuated tube) shaking and tapping, after hydrolysis start. After 24 hours the tubes are removed from the dry block and allowed to cool before aerating.

Supernatant is transferred to a 50 ml round flask over a u-shaped glass siphon (4 mm outer diameter; Figure 15) by suction with a vacuum adapter. Residual liquid in the highly porous filter material could be efficiently recovered, leaving behind less than 10% of the solution by pressing glass pipe's orifice against the filter material. For samples without filter material, the solution is pipetted into and filtered through a Kiriyama-filter funnel placed on the vacuum adapter instead of the siphon. HCl solution is removed to dryness by vacuum rotary-evaporation at 60°C. The dry sample is dissolved in 1 ml of distilled water for further processing.

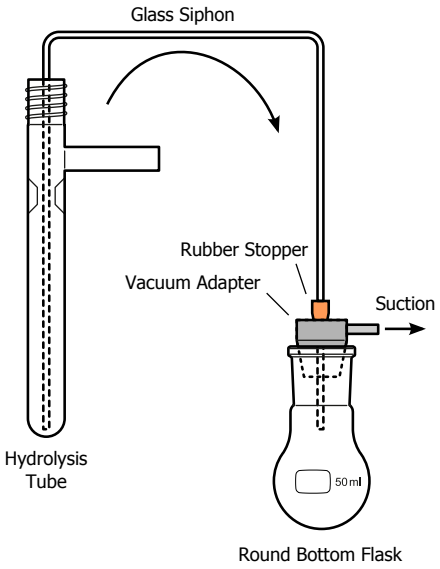

Figure 15. Glass siphon for transferring supernatant to a 50ml round bottom flask for rotary-evaporation.

Derivatization is performed by subsequent mixing of 70 µL borate buffer solution with 10 µL aqueous sample solution and 20 µL ACQ-reagent solution (acetonitrile). For each mixing step the 300 µL polypropylene auto sampler vials are sealed with screw-caps and set on a vortex mixer for 10 seconds. The vials are heated to 55°C for 15 minutes in a dry block bath to complete the reaction. After releasing internal pressure from gaseous by-products (CO_2) the vials are set in the HPLC auto-sampler. Residual aqueous sample solutions are shock frozen in Eppendorf tubes and stored frozen to allow re-analysis should they become necessary.

4.2.3.2. HPLC-Analysis Procedure

Analysis of amino acids derivatized with ACQ was reported previously (Liu, et al., 1995; Perrot, et al., 2002; Boogers, et al., 2008) with fixed pH of 4.95-5.9 or following a pH gradient (van Wandelen & Cohen, 1997) but separation of the derivatized amino acids proved difficult to succeed in one analysis run on the general purpose HPLC-system used in this study. Oxidation of the sulfur containing amino acids cysteine and methionine (Albert, et al., 2008) has been considered, was not implemented in the current procedure for sake of simplicity. Cysteine (Cys) is detected as the dimer cysteine (Cys_2) and methionine as is. Internal standard of α-amino butyric acid (AABA) which is used as internal standard in most of the mentioned analysis methods is found to interfere with cysteine detection (measured as its dimer cystine) and was replaced by

norleucine (Nle) which could be separated successfully. After optimization of pH and HPLC Gradient speeds, the following analysis procedure was finally performed:

Two gradient programs were set up with three eluents. The HPLC system from Shimadzu Corporation consisted of a DGU-14A degasser, three LC-10AD$_{SP}$ liquid pumps, a static eluent mixer, a CTO-10AS$_{VP}$ column oven and an SPD-10AV$_{VP}$ UV-VIS as well as an RF-10A$_{XL}$ fluorescence detector. Flow rate was 1mL/min and the analysis column was an octadecyl-bonded silica reversed-phase column (Inertsil® ODS-3; 250 mm×4.6 mm i.d.; 5 μm particle size) conditioned at 37°C by the column oven. Samples were injected by a Eluent A was a sodium-acetate buffer which was prepared by adding 136mmol sodium acetate and 4 mmol triethylamine (TEA) to 900 mL and titrating with a 10% acetic acid (~44 mmol) solution to 5.1 pH. The solution was then filled up to 1 L to give the final solution. Eluent B and C were acetonitrile and distilled water, respectively.

Four-point calibration curves are set up for each of the amino acid analytes by preparation of four standard mixtures with an integrated self-checking mechanism for elution sequence correctness. Nle and amino acids are mixed in a special concentration pattern shown in Table 6 allowed measurement of calibration curves for all 20 amino acids from four standard solutions Std.1-4 measured in all auto-sampler schedules. Possible displacement of elution order and peak interference caused by instrument drifts in could be reliably detected from concentration levels used in the calibration curves of each analyte. For initial investigation of retention times in a new gradient program, a binary pattern with five standard mixtures enabled unique identification of each analyte in the elution sequence.

Table 5. HPLC analysis time programs a. and b. with eluents A, B and C

Program a				Program b			
Time (min)	A	B	C	Time (min)	A	B	C
0	100%	0%	0%	0	100%	0%	0%
3	100%	0%	0%	3	100%	0%	0%
9.25	95%	5%	0%	9.25	95%	5%	0%
15.5	90%	10%	0%	21.75	90%	9%	0%
28	70%	30%	0%	34.87	70%	30%	0%
35	40%	40%	60%	37.5	40%	33%	0%
35.25	0%	60%	40%	38.5	40%	40%	60%
39.25	0%	60%	40%	38.75	0%	60%	40%
39.5	0%	0%	100%	42.75	0%	60%	40%
43.5	0%	0%	100%	43	0%	0%	100%
44	100%	0%	0%	45	100%	0%	0%

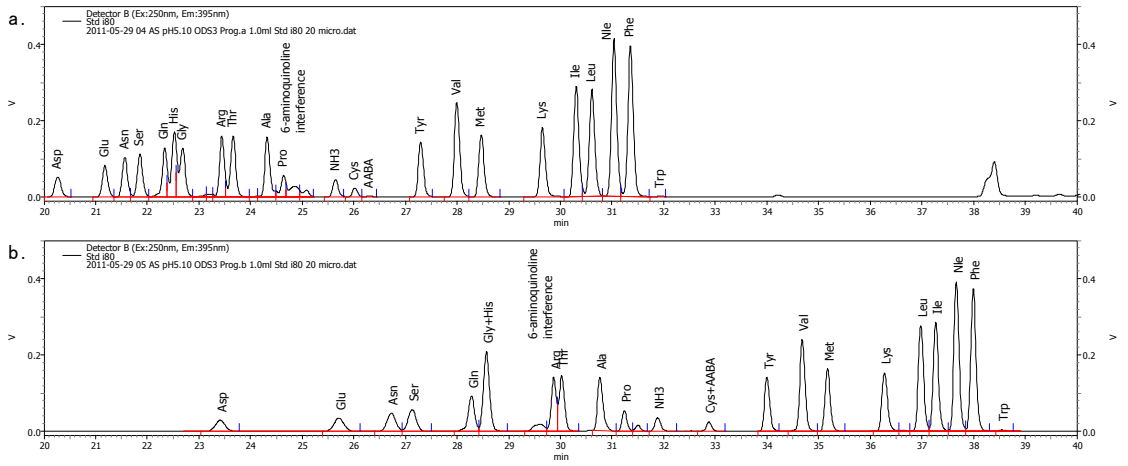

Figure 16. Chromatograms of a standard containing all amino acids measured by the fluorescence detector with gradient programs a and b.

Table 6. Concentrations of amino acids in standard mixtures for simultaneous calibration and analyte retention time verification (µmol·L^{-1}). Retention times of fluorescent amino acid derivates in gradient programs a and b. *interference with UV-active 6-aminoquinoline byproduct from the reaction with H_2O. **measured as cystine (Cys_2).

Standard mixtures						Program a.		Program b.	
amino acid		Std.1	Std.2	Std.3	Std.4	Analyte	peak time	Analyte	peak time
aspartic acid	Asp	100	60	30	0	Asp	20.60	Asp	24.00
glutamic acid	Glu	0	100	60	30	Glu	21.50	Glu	26.35
asparagine	Asn	30	0	100	60	Asn	21.80	Asn	27.20
serine	Ser	60	30	0	100	Ser	22.05	Ser	27.40
glutamine	Gln	100	0	0	30	Gln	22.50	Gln	28.30
histidine	His	0	100	0	30	His	22.70	His	28.60
glycine	Gly	0	0	100	30	Gly	22.90	Gly	28.80
arginine	Arg	60	30	0	100	Arg	23.60	Arg *	30.00
threonine	Thr	100	60	30	0	Thr	23.75	Thr	30.30
alanine	Ala	0	100	60	30	Ala	24.40	Ala	31.00
proline	Pro	30	0	100	60	Pro *	24.60	Pro	31.45
						NH_3	25.20	NH_3	32.00
cysteine**	Cys	60	30	0	100	Cys	26.10	Cys+AABA	33.05
						AABA	26.20		
tyrosine	Tyr	100	60	30	0	Tyr	27.50	Tyr	34.20
valine	Val	0	100	60	30	Val	28.20	Val	34.85
methionine	Met	30	0	100	60	Met	28.65	Met	35.40
lysine	Lys	60	30	0	100	Lys	29.85	Lys	36.50
iso-leucine	Ile	100	0	0	30	Ile	30.50	Leu	37.15
leucine	Leu	0	100	0	30	Leu	30.80	Ile	37.45
norleucine	Nle	0	0	100	30	Nle	31.20	Nle	37.80
phenylalanine	Phe	60	30	0	100	Phe	31.60	Phe	38.20
tryptophan	Trp	100	60	30	0	Trp	32.15	Trp	38.70

Table 5 summarizes the two gradient time programs and analyte elution times are listed in Table 6. Note, that in Program a and Program b, 6-aminoquinoline which is produced together with CO_2 from a side-reaction with H_2O interferes by UV absorption with the peaks of the proline derivate and the arginine derivate, respectively (Figure 16). Glycine and histidine, as well as AABA and Cys peaks coincide and cannot be analyzed in the latter program (Figure 16). Sub-optimal elution conditions regarding the first eluting derivates in program b further cause decreased peak height due to peak broadening. Despite the bad overall analysis performance, the second analysis allowed proline to be analyzed without interference and other analytes eluting in the latter part of the program to be verified. Tryptophan displays only very weak fluorescence and is much better detected by the UV-detector at $\lambda = 254$ nm. Presence of a large peak of NH_3 present as ammonium in levels around 1 $\mu g \cdot m^{-3}$ even in background aerosols (Kasper & Puxbaum, 1998) can, however interfere with Pro and Cys detection if its peak becomes too large.

4.3. Results and Discussion

Ambient aerosol samples were collected on the rooftop of the three-story Komaba Communication Plaza building at the Komaba campus of the University of Tokyo, 1.5 km west of Shibuya. Sampling times from about one to two weeks were chosen to cover a variety of weather and pollution episodes during a sampling period of almost a whole year ranging from February 2009 to January 2010 and yielded tens to hundreds of mg of PM per filter. Figure 17 shows cumulative aerosol mass concentrations of the aerosol samples divided to five size fractions. With a few exceptions most visible at high concentration episodes in March and May, aerosol concentrations closely resemble urban aerosol concentration in Tokyo as published by NIES.

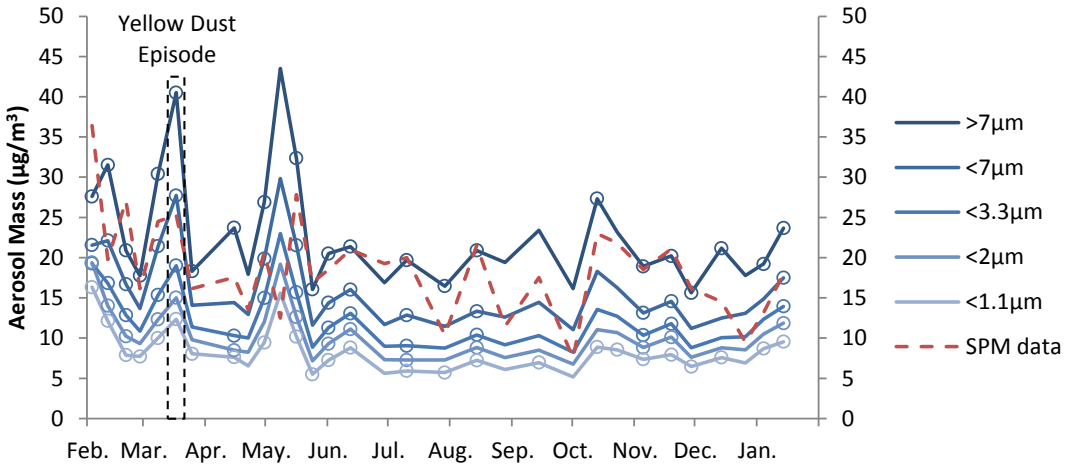

Figure 17. Cumulative aerosol mass concentrations of ambient aerosol fractions sampled with the AH-600F high volume aerosol sampler in comparison with SPM (<10 µm) aerosol data published by NIES (National Institue for Environmental Studies, Tsukuba, 2010) averaged for each sampling interval.

Data points are plotted at the beginning of each sampling interval and samples, for which amino acid analysis were carried out are marked with circles. Mostly, samples during episodes with low aerosol concentrations and of intermediate sized fractions were left un-analyzed, because overall amino acid concentration was found not sufficient for proper quantification in those samples or fractions (LOQ was around 1 ng·m^{-3} amino acid content for 1-week samples). One of the un-analyzed intervals include a high wind episode with wind speeds exceeding 40 m·s^{-1} in May where local wind-blown soil and road dust particles, which were visible to the bare eyes, is a major cause of the difference from SPM data. Another period of high concentration in March is caused by "yellow dust" from Mongolian sand storms, reported having been observed on two days for Tokyo (Japan Meteorological Agency, 2009).

4.3.1. Amino Acid Content in Ambient Aerosols

Amino acids measured from hydrolysate of aerosol were detected in the range of less than one to several tens of ng·m^{-3}. Histidine (His), asparagine (Asn), glutamine (Gln), methionine (Met), tyrosine (Tyr) and tryptophan (Trp) were mostly not detected in aerosol samples due to low abundance (His, Met), decomposition (Trp) or conversion to acidic forms during hydrolysis (Asn, Gln). Concentration patterns in ambient aerosol could however be compiled from the remaining amino acids. Amino acid patterns in aerosol size fractions show some differences apart from total concentration being low in

intermediate size fractions and indicate that coarse and fine particles originate from different source types.

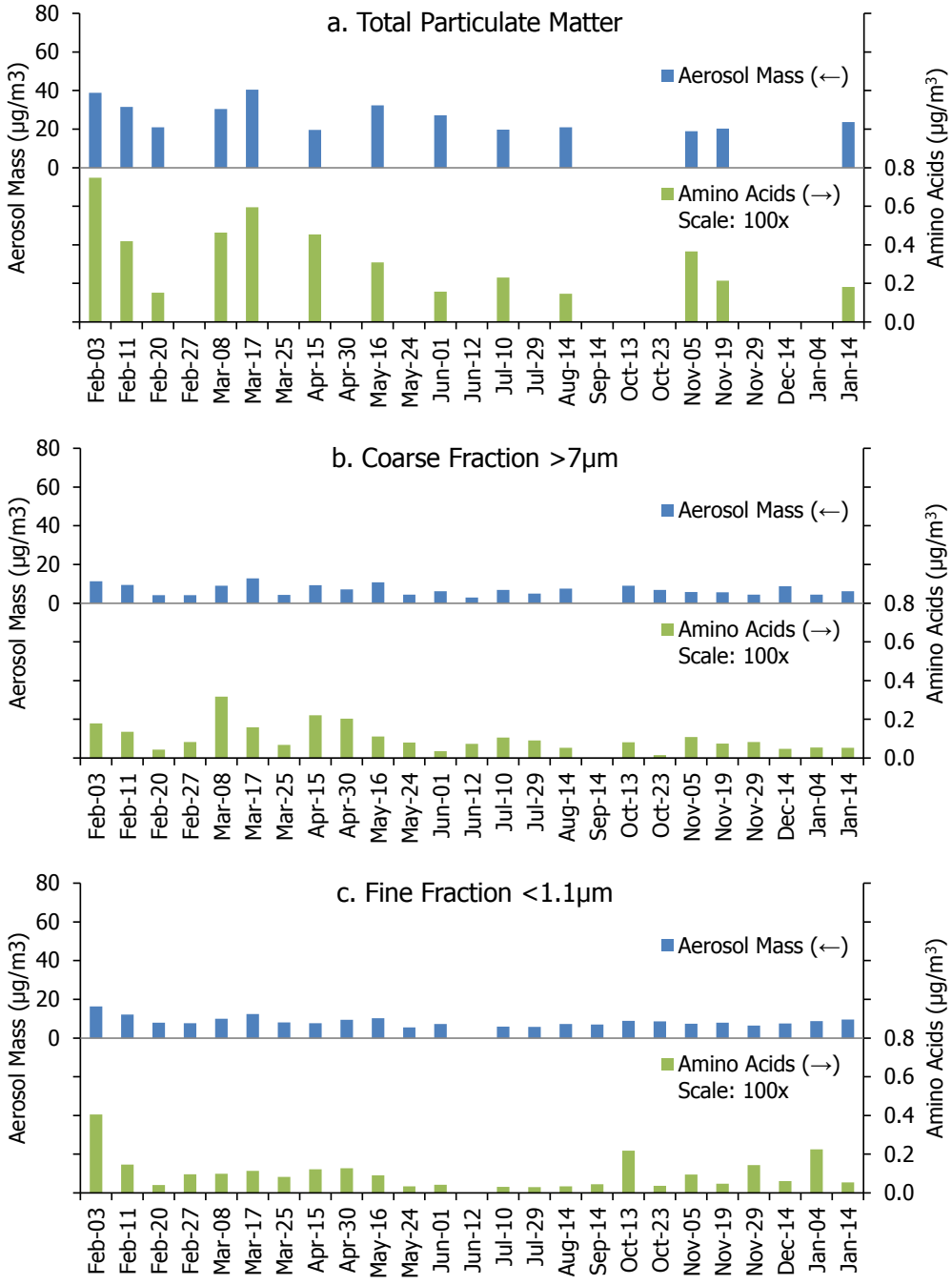

Figure 18. Aerosol mass concentrations and combined amino acid concentrations of ambient aerosol samples. a. total particulate matter (samples for which not all fractions were analyzed are left blank), b. coarse fraction >7 µm, c. fine fraction.

Mass concentrations of combined amino acid content approximately resembling protein mass, has been found to make up around 1.5% of aerosol mass in all measured aerosol

samples. Also, no distinct seasonal variation can be observed in this proportion. Combined amino acid concentrations in Figure 18 show that amino acid content is not limited to specific size fractions but is found in coarse and fine aerosol fractions at nearly the same order of magnitude. Protein content present in large and small particle size fractions show that PBAPs are either already small particles at the aerosol emission source (e.g., fungal spores or bacteria), or are generated by break-up of large particles (biomaterial or soils).

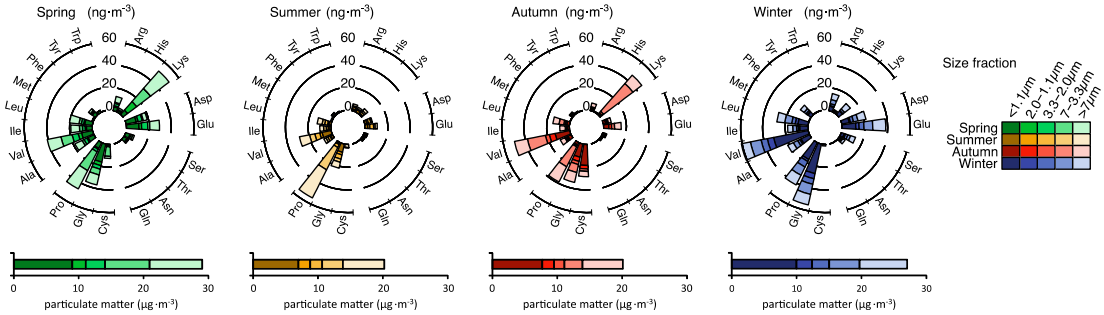

Figure 19. Seasonal variation of amino acid profiles measured from hydrolysate of ambient aerosol. Amino acid profiles are similar for spring and autumn and lowest amino acid concentrations are observed during summer.

Amino acid compositions vary between size fractions within a sampling period and between samples from different meteorological episodes. For seasonal averages in Figure 19, samples are categorized by starting dates of sampling periods falling into three-month intervals starting with March-May representing spring. Spring and autumn show some similarity with high concentrations of Lys, Val and Pro in the larger size fractions. During summer, most amino acids are only detected at very low levels, because overall PM concentration was low with no high PM episodes. Winter averages are mostly dominated by a single sample of very high concentration in the smallest size fraction (e) starting on Feb. 3.

4.3.2. Amino Acids in Aerosol Source Samples

In order to obtain amino acid source profiles for aerosol particle sources several types of samples containing protein matter were collected and either analyzed by direct hydrolysis of powdered samples or sampled with the high volume aerosol sampler after separation of large particles.

Kitchen aerosols sampled from a kitchen (Itamae-Ryōri "Ebisuya", 2009) exhaust vent contained similar amounts of amino acids as shown in Figure 20 at a total of 2.0 to 2.8 $\mu g \cdot m^{-3}$ in all particle-size fractions above 1.1 µm, with particulate matter concentrations showing a rising tendency towards large particles from 59 to 122 $\mu g \cdot m^{-3}$. The amino acid pattern observed for the smallest particles in Figure 20 e. is distinctively different from those in larger PM fractions with high content of glutamic acid and valine. AAs make up 1.7-3.9% of PM in each fraction.

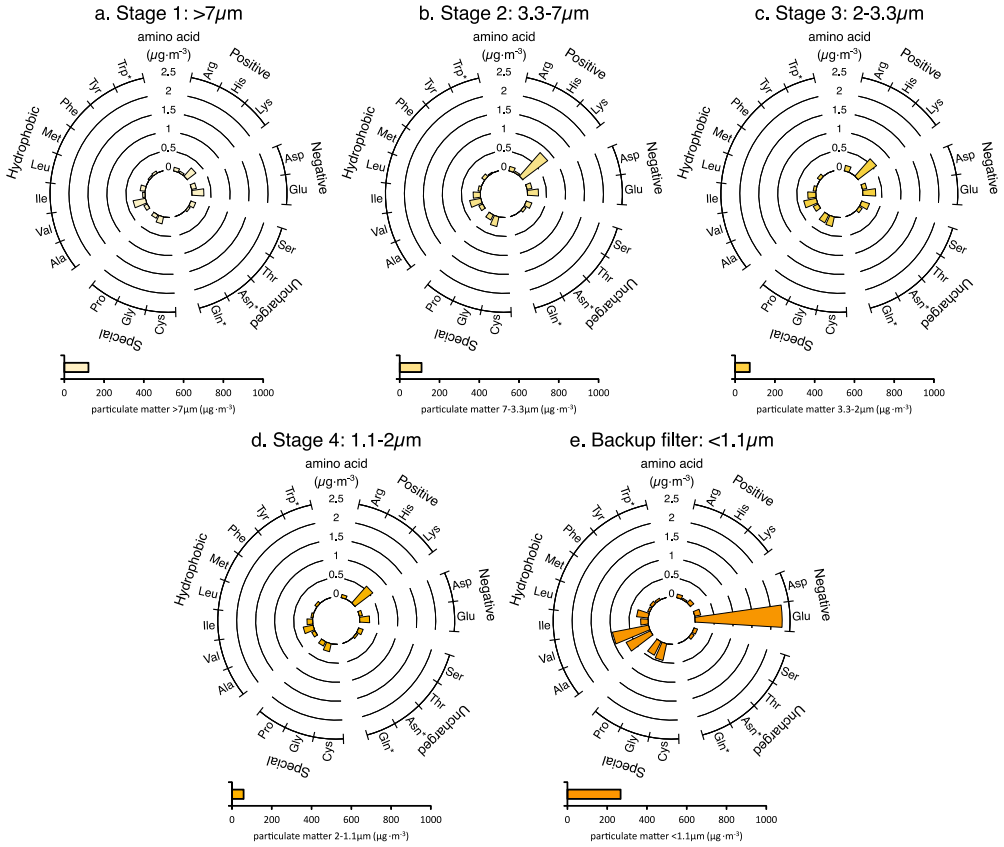

Figure 20. Amino acid profiles of kitchen exhaust aerosol sampled with the high volume aerosol sampler show high similarity between size fractions larger than 1.1 µm on impactor stage 1 to 4.

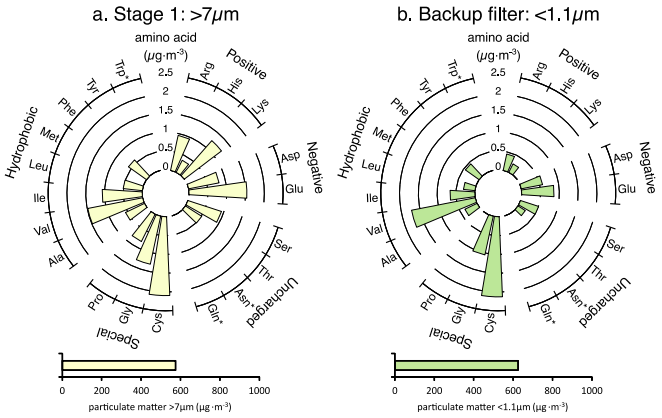

Figure 21. Amino acid profiles of pollen field-samples from cryptomeria japonica. Particles from impactor stage 1 (>7μm) and from the backup filter (<1.1μm) displayed slightly different amino acid compositions.

In pollen samples large particles made up 99.7% of total PM (0.53 g·m^{-3}) and were separated with the cyclone separator from smaller particles, which are of main interest in size resolved analysis. With most particles larger than 7 μm separated, remaining fine PM was mainly found on the first impactor stage collecting particles >7 μm and on the backup filter <1.1 μm at a concentration of only 5mg in 8 m^3 aerosol sample. On intermediate impactor stages from 7 to 1.1 μm PM could not be quantified gravimetrically (<2 mg per filter). For these size-fractions, AA analysis was not carried out. For CMB-modeling, results from the first impactor stage (>7 μm) are used for particles larger than 3.3 μm and those from the backup filter (<1.1 μm) for smaller fractions. AA compositions Figure 1(c) in the two analyzed fractions were very similar with minor differences for lysine (Lys), glutamic acid (Glu) and proline (Pro) and overall AA content made up 2-2.6% of PM. Remarkable are the high concentrations of cysteine and valine

The remaining source-profiles were pooled from multiple results of powdered samples and literature data, where possible. Samples analyzed by direct hydrolysis include leaves, which are ground down to small particles by road traffic, ground fingernail and skin shavings, which contribute to house dust, as well as residential house dust samples, kitchen aerosols and Japanese cedar pollen. Source profiles for evaluation in the CMB receptor model are compiled as patterns of amino-acid concentrations found in unit mass of the respective aerosol source. Aliquots of the powdered samples were then spiked with internal standard and hydrolyzed in 6mL hydrolysis tubes (with 2 mL 6 N HCl) following the same procedure as for filter samples, except that the hydrolysate was filtered using a small Kiriyama-funnel to remove undigested residue.

Leaf samples from defoliating trees of local maple, zelkova serrata (elm family), ginkgo and Japanese red pine were collected during October and November 2008. The freshly fallen and mostly dry leaves were further dried in the desiccator and ground down in the mortar to obtain powdered samples with help of liquid nitrogen additions which increased brittleness of hard to crush fragments.

Amino acid profiles of ground leaf samples do almost completely coincide for different species of trees, as shown in Figure 22, for samples from different elm (a. and b) and maple (c. and d.) variations, when normalized to amino acid content. Corresponding sample mass, however show significant variations, indicating different amounts of non-protein material in each of the samples.

Tryptophan (Trp), which is usually lost during the hydrolysis process, has been detected in all leaf samples. For receptor model calculations, it is however excluded, because it has not been detected in quantifiable amounts in any of the other samples.

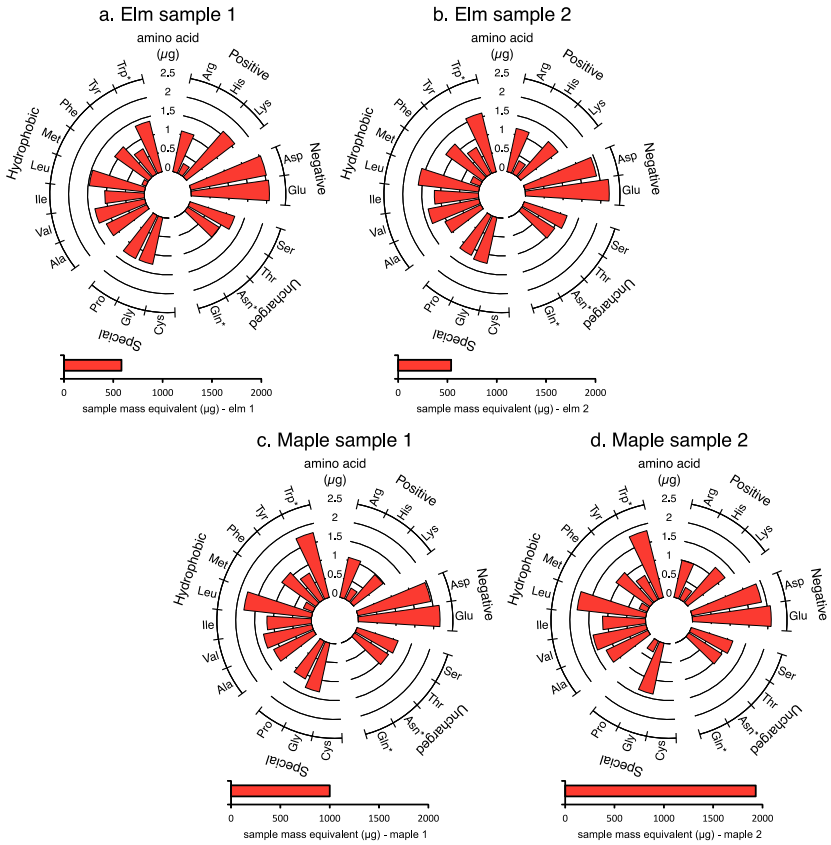

Figure 22. Amino acid profiles measured in hydrolysate of elm (a. and b.) and maple (c. and d.) leaf samples are almost identical but show some variation in protein concentration per sample mass.

Skin samples were collected by shaving off surface skin from the almost hairless inner side of the forearm in small portions repeated over several days. Fingernails were directly filed to obtain powdered samples. Skin and fingernail samples (Figure 23 a. and b., respectively) show some differences with cysteine only detected in fingernails and glycine and proline at elevated levels in skin samples. Overall analysis results these samples, however, agreed with previous results for d. hair (Robbins, 2012), e. wool (Cornfield & Robson, 1955), c. horn and f. feathers (Block & Bolling, 1951) and were combined as keratins. High protein content is typical for these samples with amino acid content making up 44, and 66% for skin and fingernails, respectively. Due to sample mass data missing in the references, profiles are calculated as amino acid percentage in total protein mass. Though generally considered relatively large particles in the order of tens of µm, keratins may play a role in overall house dust composition.

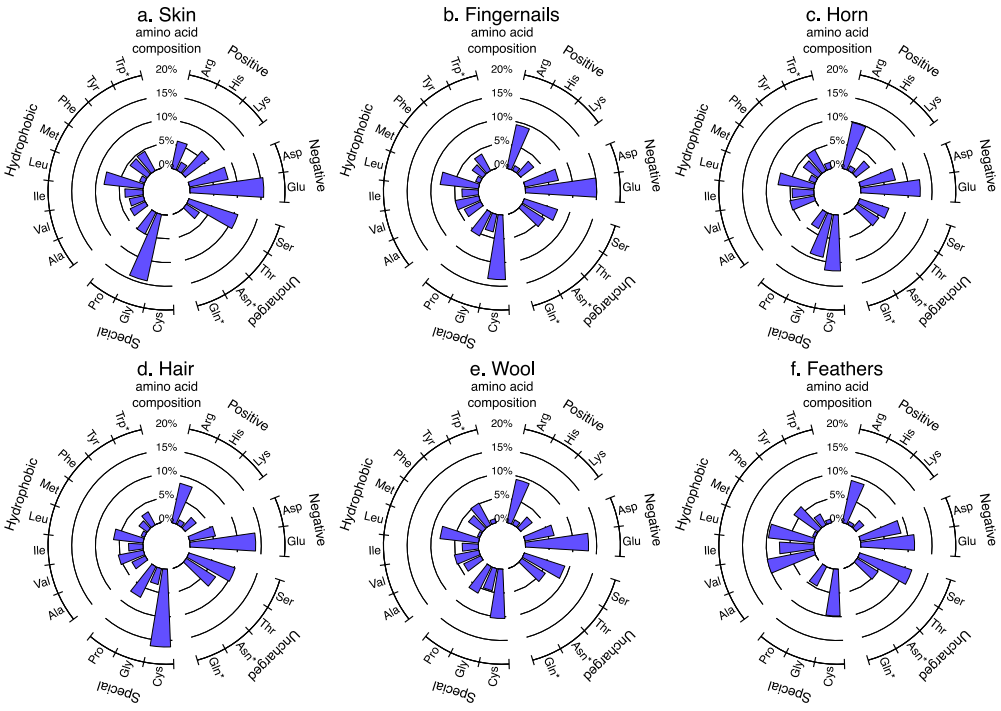

Figure 23. Amino acid profiles of different kinds of keratin: a. skin and b. fingernail samples were analyzed in this work and combined with literature data for c. horn, d. hair, e. wool and f. feathers.

4.3.3. Source Apportionment

To explain amino acid patterns in ambient aerosol (Figure 24 a.) data sets were combined and narrowed to six groups of b. kitchen, c. pollen, d. leaves, e. keratins, f. silk

and g. spores as aerosol sources. For leaves and skin, the same pattern was applied for receptor modeling in all size fractions, while for kitchen and house dust, profiles of the corresponding size fractions were used and for pollen, the profile from the large particle fraction was used for fractions > 2 μm and else from the fine aerosol fraction. Amino acid concentrations and aerosol mass uncertainties for each group were estimated from inter-sample variations and limits of detection of the measurement method. The chemical mass balance model was allowed to eliminate sources in order to prevent assignment of negative concentrations caused by contributions of unknown sources to ambient aerosol data. Source apportionment results summarized in Figure 25 use total amino acid mass rather than aerosol mass as reference.

Contributions from kitchen aerosols are present in all fractions but are only high in large particles a. >7 μm and for a few samples also in intermediate fractions b. 7-3.3 μm to d. 2-1.1 μm. Most likely false assignments are seen in the sample starting on March 17, which should be dominated by aeolian dust from Mongolian desert storms, as reported on two days for Tokyo (Japan Meteorological Agency, 2009). Pollen is found in fraction a. > 7 μm from February to March which represents the main pollen season in Japan with the Japanese cedar blooming, but also occur persistently for particles <1.1 μm throughout the year. Leaves start occurring in fraction a. >7 μm around December, shift to fraction e. <1.1 μm during February and are detected until around May. Keratins, silk and spores did not show obvious seasonal trends and were detected in fraction a. and b. >3.3 μm as well as in fraction e. < 1.1 μm.

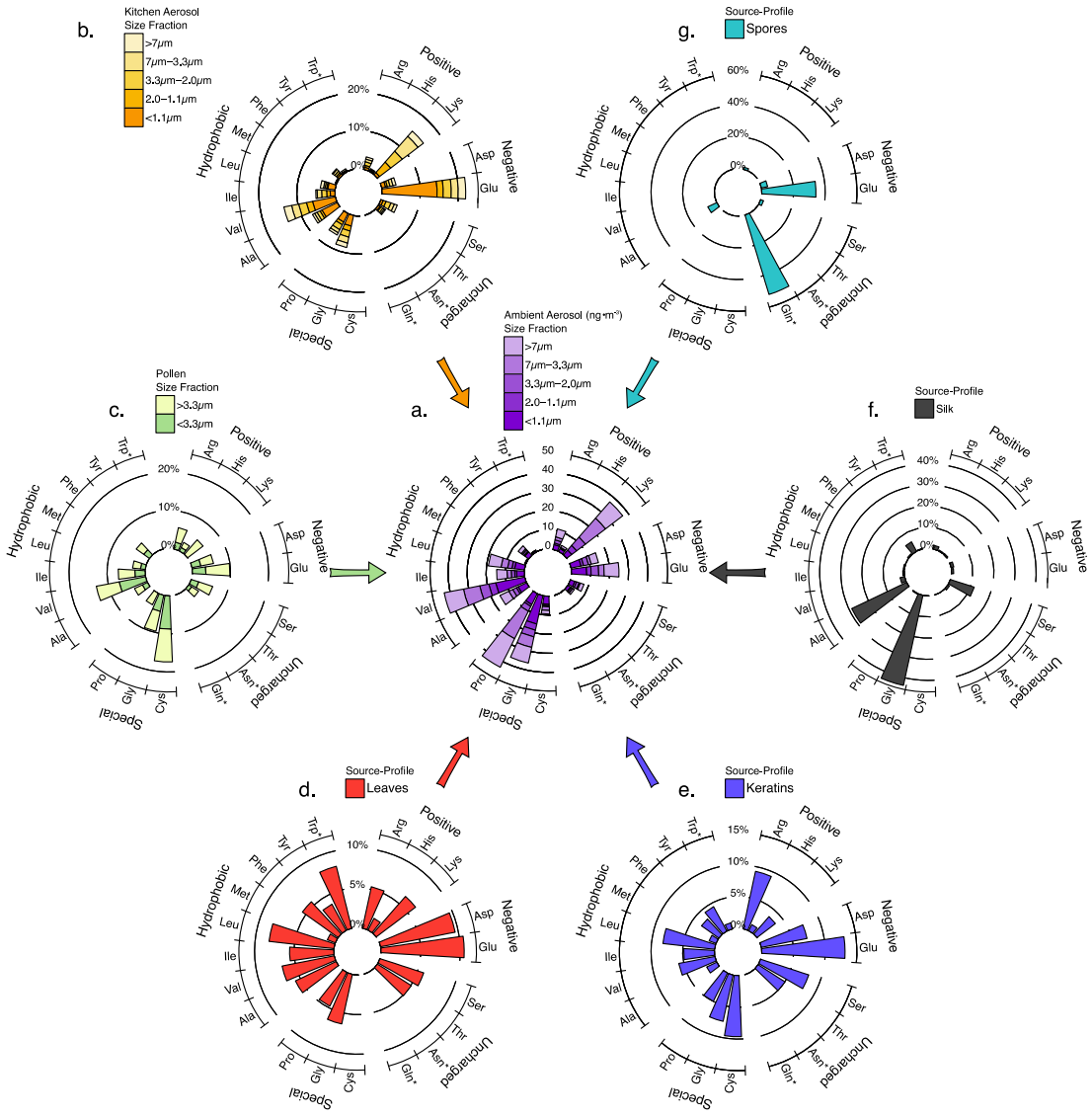

Figure 24. Amino acid compositions in a. ambient aerosol are represented as average composition for each particle size fraction. Six source-profiles of b. kitchen exhaust aerosol, c. small sized fractions of airborne pollen from cryptomeria japonica field-samples, and of d. fallen leaves, e. keratins, f. silk, and g. fungal spores are used to explain a. ambient aerosol data. *Asn, Gln and Trp were not included in the receptor model.

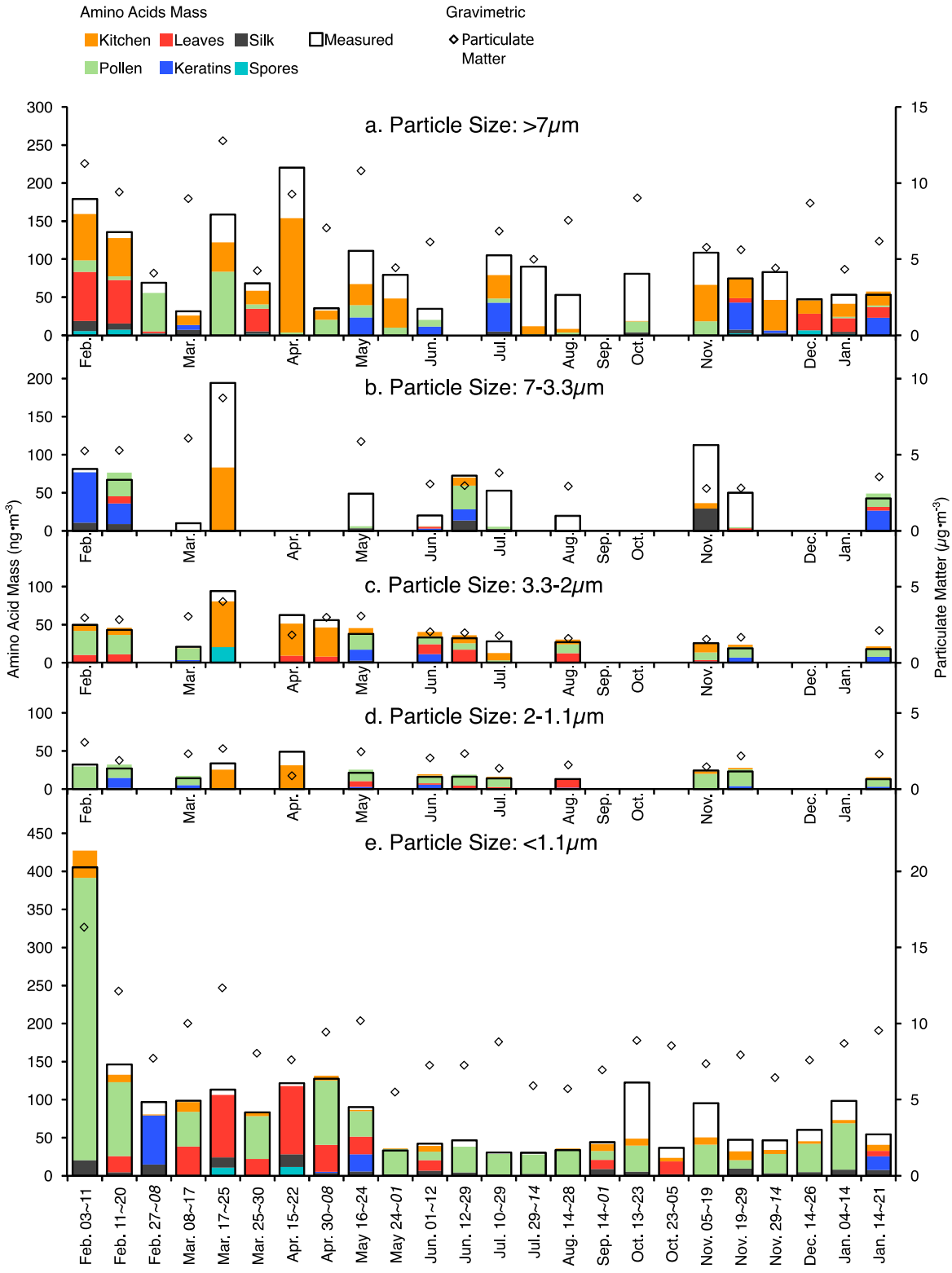

Figure 25. Source apportionment results for aerosol size fractions collected over a one year period from February 2009 to January 2010.

These results demonstrate that emission sources of PBAPs can be traced by analyzing protein amino-acid compositions down to the sub-micrometer region which previously required identification and analysis of a tracer substance for each source. At the same time the weakness of the chemical mass balance model for false assignments which in this work is played on by the presence of unknown sources and the limited number of species analyzed surface in the form of implausible results such as the assignment of high contributions from kitchen aerosols during the aeolian dust episode or persistent presence of pollen in particles < 1.1 µm.

4.4. Conclusion

Protein content of primary biological aerosol particles has been utilized to detect their presence in five particle size fractions separated by a high-volume cascade-impactor. Protein amino-acids are found in proportions of 0.5 to 2% relative to particulate matter almost uniformly distributed over all size fractions of urban aerosol down to particle sizes < 1.1 µm. No distinct seasonal variation was observed in the proportion. This means for the samples of urban aerosol collected in this study, that PBAPs are present in accumulation mode particles at approximately the same mass concentrations as in coarse particles larger than 7 µm. Though not all amino acids could be measured in ambient aerosol sample-fractions due to low abundance or hydrolysis stability of some proteinogenic amino acids, aerosol sources could be traced using the chemical mass balance model calculations even with reduced the number of variables available. For the first time seasonal variation of contributions from primary biological aerosol particle sources could be traced using their amino acid profiles without the need to use source-specific tracer substances, immunological or microscopic methods. Elimination of interferences and improvements in limit of quantification together with a more extended aerosol source library and combination with data of elemental analysis or analysis of other species can improve speed of analysis, as well as accuracy and completeness of aerosol source apportionment results, which, especially for intermediate fractions providing only low absolute sample amounts was subject to high uncertainties. Annual average protein content in urban atmospheric aerosol above Tokyo was 0.30 $\mu g \cdot m^{-3}$ to which the largest and smallest particle size fractions of > 7 µm and < 1.1 µm contribute 29% each. Though contributions of urban aerosols may make up only part of global PBAP emissions estimated at roughly 1000 $Tg \cdot yr^{-1}$ (Jaenicke, 2005), the surprisingly high abundance of sub-µm particles measured in this study

strongly support PBAPs as significant source of cloud condensation nuclei, especially when considering the associated number concentrations. Also, increased occurrence of allergies in urban areas can be ascribed to prolonged exposure to those highly respirable particles. As depositions in the alveolar region of the respiratory tract that need to be processed by the immune system, they may play a role in the activation of allergic reactions, especially in combination with other pollutants. (World Health Organization, 1999)

5. Characterization of Aerosols from Pyrotechnics

Aerosols emitted by pyrotechnics have previously mostly been analyzed for inorganic pollutant substances such as heavy metals, and inorganic ions. In terms of performance, obstruction of visibility through particulate matter is also an important aspect. Pronounced hygroscopic behavior of the highly concentrated sub-micrometer particulate matter emissions may also play a role in cloud nucleation chemistry.

5.1. Visible Aerosols from Pyrotechnics

Through interaction with humidity in ambient air, combustion products of pyrotechnics can produce dense smoke-plumes, i.e., aerosols. For fireworks, reduction of adverse effect on visibility is of particular interest, because ongoing displays can be obscured under high humidity and low wind conditions. Even supposedly smoke-free compositions like ammonium perchlorate (AP)/hydroxyl-terminated polybutadiene (HTPB), which is used as propellant in some rocket motors, develop visually obscuring aerosols from its gaseous combustion products under high humidity conditions. (Kubota, 2004) Though the production of visible aerosol is intended in some applications, e.g., smoke screens or signaling (Conkling, 1985; Hardt, 2001), it is disturbing in firework scenes especially if increased by humidity. Especially in the Asian region, very high humidity conditions tend to occur often during the warm season which is when firework festivals are mostly held.

Solid hygroscopic particles in aerosols can grow by condensation of water to form aqueous droplets when critical relative humidity is exceeded. The effect of relative humidity on particle growth is well known for a number of substances. (Cziczo & Abatt, 2000; Schenkel & Schaber, 1995) HCl emissions from chlorine based oxidants like perchlorates, which are commonly used in pyrotechnics, also cause mists to be produced in high humidity or low temperature conditions. (Kubota, 2004; Cocks & Fernando, 1981) In presence of HCl vapor, condensation on hygroscopic particles, which act as hygroscopic particles, is further promoted to produce even denser smoke clouds.

Light scattering by aerosol particles reduces contrast and brilliance, i.e., visibility of pyrotechnics. Attenuation of straight light transmittance through aerosol clouds and addition of scattered light to otherwise generally dark background both degrade the visual impression of pyrotechnics. Most conceivable combustion products except soot can be described as transparent particles with refractive indices of about 1.33 to 1.5. For such particles, scattering efficiency increases largely for visible light ($\lambda \approx 0.5$ μm) when

diameters grow to around 1µm. (Jacobson, 2005c; Bohren & Huffman, 1983) Particle size and growth characteristics of therefore make up important factors in describing the optical depth of aerosol emissions.

Although efforts are made to develop compositions and substances that produce reduced visible aerosol (smokeless) emissions (Kubota, 2004; Conkling, 1985; Pagoria, et al., 2002; Badgujar, et al., 2008) the effect of relative humidity has not yet adequately been characterized. Studies on aerosol emissions from pyrotechnics based on field measurements (Wehner, et al., 2000; Wang, et al., 2007; Dutschke, et al., 2011) at outdoor pyrotechnics' displays, where relative humidity cannot adequately be adjusted, or on confined volume experiments (Dutschke, et al., 2009; Hanley & Mack, 1980; Harkoma, 2013) mostly do not include experiments at high humidity conditions. Particle sizes reported in the range of a few 100 nm can however increase significantly by uptake of water vapor from humid ambient air.

Visible aerosol development after combustion of pyrotechnics in ambient air of arbitrary relative humidity can be simulated in chamber experiments. Gas and particulate emissions are quickly diluted and cooled in air and undergo nucleation, coagulation and condensation processes. In this work, a measurement method using a small-scale combustion-chamber is proposed for quantification of visual obstruction by aerosol. This allows comparison of visible aerosol development after combustion of different types of pyrotechnic compositions over a range of controlled humidity conditions. Humidity characteristics of the following three types of pyrotechnic compositions were measured to illustrate typical differences in aerosol visibility: Ammonium and potassium perchlorate (AP, KP) based compositions which are widely used as a basis for pyrotechnic compositions (Kosanke & Kosanke, 2004). Black powder (BP) which is still the predominant composition used as lifting charge, although it is well known for producing relatively dense aerosols.

5.2. Experimental Methods

5.2.1. Combustion Chamber

A chamber consisting of a cubic steel frame covered with acrylic sheets at the top and three sides, a stainless steel floor and a detachable soft PVC sheet at the front side was constructed as shown in Figure 26. Room temperature was controlled by air conditioning. After initial temperature and humidity conditions were applied with a humidity controllable type air-conditioning unit (Apiste PAU300S-HC), the chamber

was sealed. Combustion experiments were mainly performed at 20°C, but measurements which were also made at 30°C and for BP also at 10°C showed that aerosol opacity is virtually independent of temperature. Samples were placed on a combustion platform (b) and ignited by an electrically using a nichrome wire embedded in a ceramic tube and air in the chamber was mixed using an electric fan (d) so that a sufficiently homogeneous aerosol was yielded within about ten seconds after combustion.

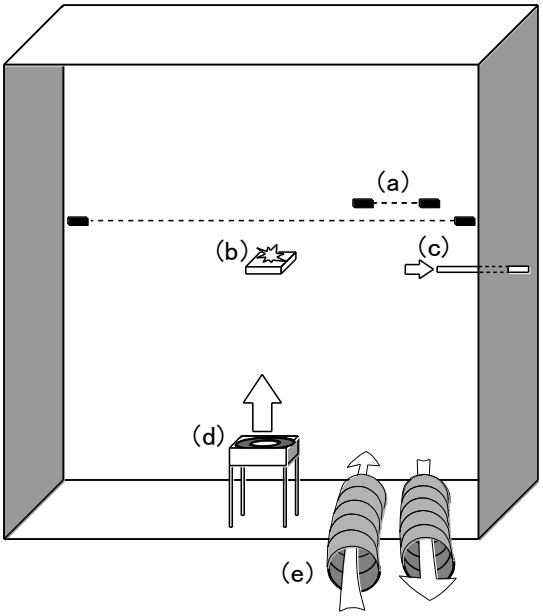

Figure 26. Combustion chamber features (front view). (a) Laser emitter - transmittance sensor assemblies; (b) combustion platform; (c) sample suction port; (d) circulation fan and psychrometer; (e) ducts to humidity control unit

5.2.2. Light Extinction

To evaluate the opacity of the aerosol, light transmittance was monitored during combustion experiments with two laser sensors (Keyence LX-100, λ=670 nm) installed in the middle of the chamber at distances of 77.5 and 10 cm between emitter and sensor, respectively. An attachment was added to the sensors as shown in Figure 27 to protect the emitter and sensor windows from any aerosol depositions by a flow of clean air from an external membrane pump. Two grams of sample per cubic meter were found to be optimal for producing an adequate response in the scattering coefficient over the whole humidity range while not inflating the front chamber cover too much.

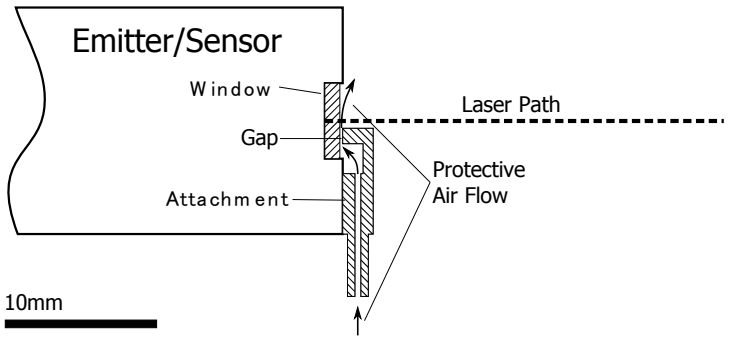

Figure 27. Laser Emitter/Sensor attachment to protect laser windows from particle deposition. Filtered air is supplied through PVC tubings from a membrane pump.

Visibility of aerosol is caused by light scattering or absorption and is dependent on its particle size and number concentration. Combustion products found in aerosol particles can be considered mainly to consist of solid salts or oxides and aqueous solutions of salts and acids which have refractive indices in the range of n_r = 1.33 to 1.5 (real part) for visible light ($\lambda \approx 0.5$ µm). Such particles only show minimal light absorption (imaginary part of refractive index), unless soot particles or special dye substances (colored smoke compositions) are present, or they grow very large as in precipitating clouds. Single particle scattering efficiencies can be described by Mie scattering theory for small spherical particles ($0.03 \cdot \lambda < d < 32 \cdot \lambda$) and scatter visible light ($\lambda \approx 0.5$ µm) most efficiently with particle diameters between 0.3 and 2 µm. (Jacobson, 2005c; Bohren & Huffman, 1983) Particles which are much smaller than the wavelength of light ($d < 0.03\lambda$) are in the Rayleigh regime and absorb or scatter light only weakly. For larger particles, scattering efficiencies also decrease with number concentrations because mass concentrations are limited by condensable vapors available and are hence only reached by coagulation processes.

5.2.3. Particle Size Distributions

Particle size distributions (PSD) of aerosols generated by pyrotechnics were reported in previous research to be found in the range of several hundreds of nm. (Wehner, et al., 2000; Dutschke, et al., 2011; Dutschke, et al., 2009) Visible increase of smoke development in high humidity conditions, however, suggests further growth of hygroscopic particles. A flow of aerosol was transferred to particle measurement equipment a pipe (12 mm i.d.) of stainless steel serving as sample suction port (Figure 26 (c)) in order to perform continuous measurement of particle size distributions.

5.2.3.1. Particle Counter

PSD measurements using an optical particle counter (RION KC-11) were only possible with extremely small amounts of composite pyrotechnics sample in the order of tens of mg for the low-smoke AP/HTPB base-composite, because aerosol concentrations quickly exceeded the measurable range of 10^6 particles per liter. At such high concentrations, particles cannot be separated to single countable signals in the measurement instrument's light path. Low sample size further made complete combustion difficult and changes in light-transmittance hardly measurable under conditions which would allow the simultaneous application of particle counting techniques as was previously also observed in large scale chamber experiments. (Hanley & Mack, 1980)

5.2.3.2. Mie Scattering PSD Analyzer

To measure PSD of highly concentrated aerosol generated in the chamber, a HORIBA LA-920 particle size distribution analyzer was modified to introduce aerosol in a sheath flow into a flow cell for measurement of its Mie light scattering pattern. This allowed direct measurement of the aerosols PSD without prior dilution. Calculation parameters for Mie scattering calculations in particle size measurements with the particle size distribution analyzer were performed using refractive indices of water and air at 20°C ($n_r = 1.33\ n_i = 1.0 \cdot 10^{-9}$). Simple analysis of scattering patterns with Mie scattering codes (Prahl, 2012; Flateau, 2011) show that scattering patterns change greatly with particle size ($d = 0.1 \sim 10$ μm), but not noticeably with refractive indices in the expected range ($n_r = 1.33 \sim 1.50$). Therefore, deviation of actual refractive indices from those used for Mie-scattering pattern analysis does not largely affect calculated PSDs. Also, overall scattering efficiencies can be considered practically indifferent in the range of refractive indices expected. (Peng & Effler, 2012)

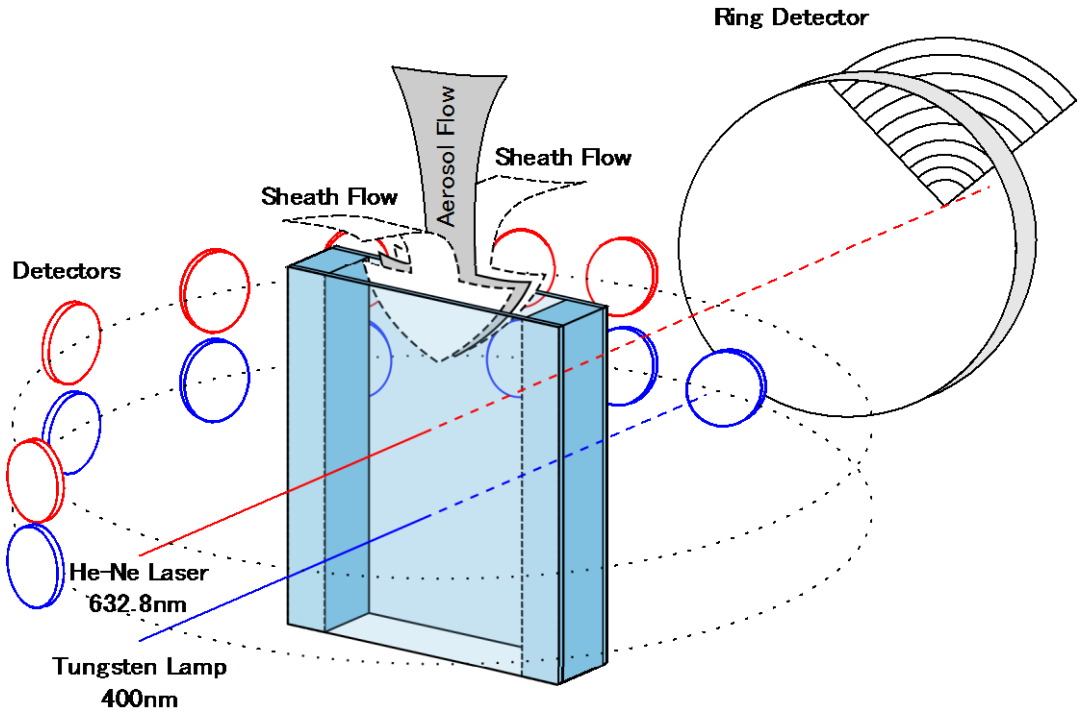

Figure 28. Setup of the MIE light scattering based particle size distribution analyzer with aerosol introduction in a sheath flow.

5.2.4. Relative Humidity and Temperature Control

In order to obtain reproducible measurement results, temperature was held constant at 20°C for most experiments and relative humidity was varied by adding humidity utilizing a humidity controlled air conditioning unit (Apiste PAU300S-HC) connected through ducts to the combustion chamber (Figure 26 (e)). Dehumidification capacities of room air conditioning and humidity controller were not sufficient to reach relative humidity conditions below 40% during the summer months. Experiments at very dry conditions were therefore only carried out during the winter months where relative humidity as low as 25% could easily reached by keeping room temperature at 20°C. After initial temperature and humidity conditions were applied with the air-conditioning unit, the chamber was sealed throughout the combustion experiment.

5.2.4.1. Room Air Conditioning

Although temperature and humidity inside the chamber can be controlled by the dedicated air conditioning unit, room temperature had to be matched with the chamber settings, because, heat transfer and condensation processes on the thin chamber surfaces could significantly influence the environment inside the chamber. Temperature

drifts and premature water vapor losses would adversely affect aerosol observations.

5.2.4.2. Humidity Measurement

Measurement of temperature and relative humidity during combustion measurements proved difficult due to corrosive, condensing HCl gases causing electronic sensors to fail or drift due to contact errors and chemical attack of the sensor itself. Therefore a classic Aßmann-psychrometer was resorted to with wet-bulb and dry bulb temperature measurement through thermocouples. A continuous air flow past the wet and dry bulb ensured quick establishment of equilibrium conditions. A mirrored heat shield was found unnecessary in the chamber configuration, since the room was well isolated and conditioned at ambient temperature and no direct sunlight or radiation from heated surfaces could disturb the temperature sensors and accurate measurement was predominantly found important at high relative humidity, where the radiation effect is minimal. The mirrored surfaces would further quickly deteriorate due exposure to the corrosive gases and aerosols and lose their radiation reflecting capability. More importantly, the thermocouple surfaces had to be protected from HCl attack which causes elevated temperatures to be reported by a plastic film coating. The wet and dry bulb temperatures can be converted to relative humidity by

$$RH = \frac{e'(p, T_{\mathrm{db}}, T_{\mathrm{wb}})}{e'_w(p, T_{\mathrm{db}})} \tag{25}$$

where $e'_w(T, p)$ is the saturation vapor pressure of water and $e'(p, T_{\mathrm{db}}, T_{\mathrm{wb}})$ is the psychrometric wet-bulb vapor-pressure given as

$$e'(p, T_{\mathrm{db}}, T_{\mathrm{wb}}) = e'_w(p, T_{\mathrm{wb}}) - 6.53 \cdot 10^{-4} \cdot (1 + 0.000944 \cdot T_{wb}) \cdot p \cdot (T_{db} - T_{wb}) \tag{26}$$

with saturation vapor pressure

$$e'_w(p, T) = f(p) \cdot 6.112 \exp\left(\frac{17.62 \cdot T}{243.12 + T}\right) \tag{27}$$

and pressure correction

$$f(p) = 1.0016 + 3.15 \cdot 10^{-6} \cdot p - 0.074 \cdot p^{-1} \tag{28}$$

(World Meteorological Organization, 2008).

5.2.5. Theoretical Considerations

5.2.5.1. Chemical Equilibrium Analysis

Combustion of AP/HTPB composite pyrotechnics can be interpreted as a two-step process. A premixed flame of ammonia with perchloric acid closely coupled with the sublimation and decomposition of AP and HTPB binder provides excess oxidizer to form

diffusion flames with fuel fragments released from the binder. (Kubota, 2007) Though this process its kinetics are complex near the surface, especially, if additives have to be taken into account, combustion products and flame temperatures can roughly be estimated using chemical equilibrium calculations with the NASA Chemical Equilibrium with Applications (CEA) program package (Zehe, 2010) which was extended with thermodynamic data available online (Anon., 2013). Equilibrium states were analyzed for a dilution series with air for the lightly oxidant-deficient composite. The results were visualized as mass fractions excluding the mass of air additions to track conversion of all species related to the corresponding metals.

5.2.5.2. Nucleation, Coagulation and Growth Kinetics

Homogeneous and heterogeneous nucleation mechanisms both play important roles in aerosol generation from pyrotechnics. Previous investigations on aerosol size distributions in the range of some 100 nm (Wehner, et al., 2000; Dutschke, et al., 2011; Dutschke, et al., 2009) strongly support primary particle generation by homogeneous nucleation. Particle nucleation and growth kinetics have however not been extensively studied in theory for pyrotechnics. Studies on such processes include both experimental measurements and numerical simulations in the vicinity of burning coal particles (Senior & Flagan, 1982) or in turbulent jets (Zhou & Chan, 2011; Lesniewski & Friedlander, 1998) of hot gas. A program for solving particle nucleation and growth problems utilizing a Nodal General Dynamic Equation solver model (NGDE) (Prakash, et al., 2003) was extended for calculations of PSDs resulting from condensation of gaseous metal chlorides when they are cooled down by dilution with ambient air. The NGDE model computes PSDs in logarithmic volume space covering to particles of ~10^{-27} to 10^{-15} m^3 which is discretized to bins to allow changes in number concentrations of each bin to be simulated. In the GDE given by equation (29), phenomena of interest are limited to nucleation, coagulation and surface growth and are iteratively solved. Nucleation and collision frequencies, as well as condensation and evaporation speeds have been compiled from previous work.

$$\frac{dN_k}{dt} = \left.\frac{dN_k}{dt}\right|_{coag.} + \left.\frac{dN_k}{dt}\right|_{nucl.} + \left.\frac{dN_k}{dt}\right|_{evap./cond.} \tag{29}$$

Vaporized metal chloride in hot exhaust from the composite corresponding to a volume of around 2.5 L at standard conditions is diluted to a volume of 1 m^3 following an

exponential dilution function to imitate the dilution process occurring in the combustion chamber. Particle nucleation, condensation and coagulation are simulated according to the physical properties vapor pressure, surface tension and molecular mass of each of the metal chlorides in liquid state. Trends of mean particle sizes and number concentrations for different concentrations and dilution speeds were analyzed.

5.2.6. Composite Pyrotechnics Preparation

5.2.6.1. Base Composites

As a representation of pyrotechnic compositions used in fireworks, perchlorate based composite formulations presented in Table 7 were used. Application of ammonium perchlorate (AP) and potassium perchlorate (KP) mixed with hydroxyl-terminated polybutadiene (HTPB) binder enabled easy laboratory scale production. Further, grain black powder (75% potassium nitrate, 15% charcoal, 10% Sulfur; Kayaku Japan Co., Ltd) was used as a representative of chlorine free pyrotechnic composition. Combustion times varied from instantaneous combustion for black powder up to ten seconds for KP composites. Temperature inside the combustion chamber increased less than 1.0 K per gram combusted sample after combustion, but returned to within 0.2 K above initial conditions in a few minutes due to radiative and convective heat transfer to the surrounding room.

Table 7. Formulations of composites based on perchlorates

	Oxidant		Binder (Fuel)
Symbol	AP	KP	HTPB + Curing Agent
A	82%		18%
K		84%	16%

5.2.6.2. Metal and Metal Compound Additives

The use of metal compounds and metal powders is essential for flame coloration and generation of spark effects in pyrotechnics. Together with combustion products from the pyrotechnic compositions' base components their reaction products are found in emissions of very fine aerosol (smoke) particles in the range of a few 100 nm (Wehner, et al., 2000; Dutschke, et al., 2011; Dutschke, et al., 2009). The particles consist of solid metal chlorides or oxides which can act as condensation nuclei for HCl and H_2O vapor (Cocks & Fernando, 1981; Kubota, 2004; Schenkel & Schaber, 1995) emitted by the pyrotechnic composition. Though such particles scatter light only weakly at their initial

size, they produce visually opaque aerosols (Conkling, 1985; Hanley & Mack, 1980) when they grow in size, reaching a maximum in light scattering efficiency at around 1 μm for visible light (~500 nm), if number concentrations are conserved (Bohren & Huffman, 1983; Jacobson, 2005c).

Metal powders of various particle size and type find use in gold to silvery-white light, flash, sparkle and tail effects. These light effects are based on continuous spectrum emissions of high temperature particles. (Shimidzu, 1981) Practical safety and combustion performance limit the common metal types to aluminium (Al), Magnesium (Mg), Magnalium (Mg-Al, i.e., ~50% alloy of Mg and Al) and Titanium (Ti). For colored flames of green, blue, yellow and red, respectively as well as their mixtures, only compounds of barium, copper, sodium and strontium are commonly used in pyrotechnic compositions. These metals generally need to form volatile chlorides during combustion to exhibit colored emission lines. (Shimidzu, 1981; Kosanke & Kosanke, 2004) Because chlorides of these metals are hygroscopic, they cannot be directly used as additives in pyrotechnic compositions. Therefore the necessary metals are added as compounds which are decomposed and converted to metal chlorides during combustion. The necessary amount of chloride is generally provided by a dedicated chlorine donor compound or hydrochloric acid produced by the oxidant such as ammonium perchlorate (AP). These metal chloride vapors produce fine aerosol particles at high number concentrations when the exhaust gas is rapidly diluted and cooled to ambient temperatures.

AP, despite its good performance in producing colored flames, is less common in firework compositions. It also corresponds to oxidant/fuel (binder) systems in pyrotechnics being recently desired to reduce solid residue fallout. It finds heavy use in propellants and produces virtually no solid ashes or aerosols under dry conditions in contrast to oxidants based on the more common potassium salts. (Shimidzu, 1981) Though its relatively high excess of HCl emissions are known to produce visible aerosols under high humidity, combustion chamber experiments have shown that the effect is limited to relative humidity (RH) higher than 85%. The effect of additive metals and metal compounds on visible aerosol generation, particularly at high relative humidity conditions, was studied in this work by analyzing aerosol development trends in that combustion chamber.

Table 8. Formulations of composites based on ammonium perchlorate/poly-butadiene

Main Formulation			Flame Coloring and Sparkling Effect Additives		
HTPB	AP	Curing Agent	Compound	Effect	Additive Ratio
			$Ba(NO_3)_2$	Green	5-20%
			CuO	Blue	0.5-20%
			$Na_2C_2O_4$	Yellow	1-20%
			$SrCO_3$	Red	1-10%
14.5%	81.9%	3.6%	Fe_2O_3	Catalyst	2-10%
			Al	Sparks, Silver Flames	10-30%
			Mg	Flame Modifier	5-20%
			Mg-Al	Sparks, White Flames	5-30%
			Ti	Sparks	5-30%

As oxidant / fuel system with only negligible visible aerosol over a wide relative humidity (RH) range up to 85% allowing quick laboratory scale production ammonium perchlorate (AP) / hydroxyl-terminated HTPB was chosen. Potassium perchlorate is much more common as oxidant in pyrotechnics but is known for producing large amounts of solid particles including large fallout particles and fine visible aerosols. Another alternative is potassium nitrate which, as a chlorine-free system, has little visible aerosol output but generates less intensive light and large amounts of large particle residue/fallout. The AP/HTPB system, on the other hand, allows aerosol generation induced and amplified by additive compounds to be observed with low interferences from fallout-losses or particles generated by the oxidant / fuel system of the base composite. HTPB was treated curing agent (polymeric methylene diphenyl diisocyanate) mixed with AP and varying amounts of additives as shown in Table 8. The composites were then rolled out as sheets that could easily be cut to appropriate sample sizes after curing overnight.

5.3. Results and Discussion

5.3.1. Linearity over Distance and Concentration

Measurements of light transmission showed that light attenuation (A) and maximum scattering (attenuation) coefficient (b) occurring in an experiment (b_{max}) show linear dependencies to transmission length (l) and sample mass (m), respectively, even at high humidity settings (90% RH).

$$A = \log_{10}\left(\frac{I_0}{I}\right) = b \cdot l = b^* \cdot m \cdot l \tag{30}$$

Table 9. Variables used in the scattering relation

Symbol	Description
A	light attenuation
I_0	initial light beam intensity
I	light intensity at the detector
m	sample mass
l	length of light path
b	light scattering coefficient of the aerosol (smoke)
b_{max}	maximum light scattering coefficient
b^*	sample-mass specific scattering coefficient
b^*_{max}	maximum sample-mass specific scattering coefficient

Based on Equation (30) analogous to the Lambert- Beer law (Jacobson, 2005c) they can be converted to sample-mass specific scattering coefficient values (b^*; b^*_{max}) which are independent of the two parameters. Symbols used in this relation are summarized in Table 9. Note that mass here does not refer to aerosol mass (mass concentration of particles in the chamber) but to mass of incinerated sample. Because some products remain gaseous or quickly precipitate as solid ashes, while water vapor can be absorbed by aerosol particles, mass of aerosol generated by pyrotechnics is not easily predictable, whereas sample mass is a convenient reference.

Only for scattering coefficients greater than 2 m^{-1}, this relation shows a non-linear behavior (Figure 29) and mass-specific scattering coefficients decrease. Processes like coagulation and deposition, which are dependent on aerosol concentration and particle size, reduce particle numbers and thereby overall light scattering. The linear region towards lower sample mass best represents real firework displays, where aerosols are quickly dispersed over a large volume. A series of similar measurements on smoke screen compositions has been performed by Harkoma. (Harkoma, 2013) In his measurements, which were performed in a smaller chamber (0.15 m^3), scattering (extinction) coefficients much more quickly decreased after combustion than observed in this study. This may be an indication for increased coagulation and wall deposition effects caused by higher aerosol concentrations or temperatures after combustion, but differences in type of aerosols produced can also play a role.

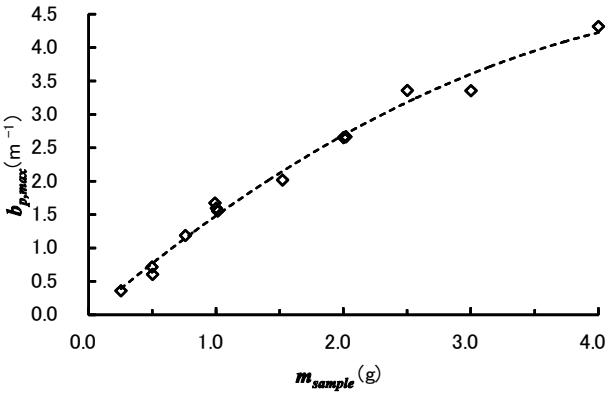

Figure 29. Maximum scattering coefficient after combustion of composite-K at 90%RH plotted against sample mass.

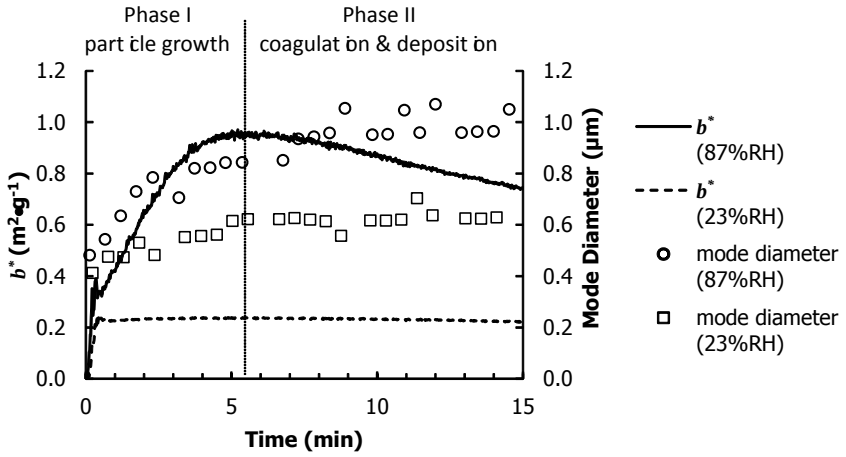

Figure 30. b^* and mode diameter of aerosol generated by combustion of 2g composite-K at ○87%RH and □23%RH.

Despite its similarity to the Beer-Lambert law, b^* gained by this relation displayed time dependency caused by particle growth and deposition in the generated aerosol, especially at high relative humidity conditions. Composite-K shows typical characteristics as seen in time curves of b^* in Figure 30 for 87% and 23%RH. After combustion under high humidity conditions, particle growth (mode diameter: ○) was observed for 4 to 6 minutes in phase I and reached a maximum after which b^* declined slowly. Continuing growth in mode diameter of the aerosol observed in phase II suggest coagulation processes, but increased losses due to particle deposition on wall and fan surfaces also possible with larger particles. Under dry conditions up to 50%RH (23% in Figure 30), b^* reached it's a nearly constant value immediately after initial fluctuations

due to fan circulation. After slight growth (mode diameter: □) in phase I the measured PSDs also remain constant, indicating negligible coagulation and deposition for particle modes up to a diameter of 0.6 µm during the experiment. Increase of aerosol visibility of Composite-K at high RH can be attributed to condensation of water vapor and HCl onto KCl particles which leads to high number concentrations of particles with diameters around 1µm, which have high scattering coefficients.

Somewhat different results were obtained for the remaining two compositions: In experiments with composite-A, b^* either reached its maximum even more quickly within 1 minute at humid conditions (above 80%RH) and declined within 5 to 10 minutes almost to complete transparency, or, when dry conditions (below 80%RH) were applied, did not show any measurable light attenuation at all. This is because combustion products of composite A only consist of gases like CO_2, H_2O and HCl, of which the latter induces aerosol generation at high relative humidity. Although particle size could not be measured with the particle size distribution analyzer, because scattered light intensity was too low and PSD changed too quickly, visible particle depositions on chamber walls and floor were observed and hydrochloric acid could be captured in open containers containing a layer of water placed on the chamber floor. This indicates particle loss due to precipitation of large particles which cannot be sustained in a small agitated chamber. Black powder showed time curves of b^* similar to those of composite-K, only reaching its maximum more quickly 2 to 3 minutes after combustion.

5.3.2. Measurement of Particle Size Distribution

In the current series of combustion experiments, measured PSDs were mostly found to consist of a single mode. PSDs of aerosols generated by composite-K and black powder under humid conditions displayed a mode diameter shifting to larger sizes over time, indicating particle growth which may occur by coagulation of particles or absorption of water and other vapors. The absence of particle growth under dry conditions below 40% RH, suggests that coagulation over timescale of minutes can be neglected for small particles, but may play a role after particle growth to diameters in the near-µm range.

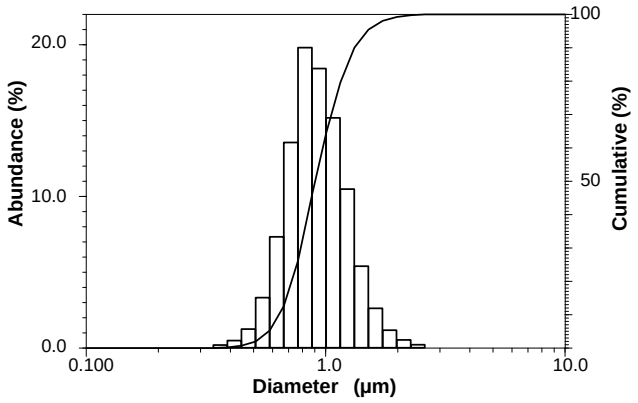

Figure 31. Particle volume distribution of aerosol 5 minutes after combustion of 2g composite-K at 87% RH shows a single mode at about 1 µm.

In experiments with composite-A, particle size grew so quickly, that aerosol disappeared by deposition on chamber surfaces as indicated in the previous chapter and measurements with the Mie scattering PSD analyzer did not succeed due to low time resolution (≈30 sec) and insufficient scattering intensity.

In Figure 30, mode diameter is plotted along with b^*_{max} for composite-K at 87%. Mode diameter grew from 0.55 to around 1.05 µm within quarter an hour, passing 0.8 µm where b^* reached its maximum. Figure 31 shows the PSD measured at that point, displaying its single mode diameter (maximum abundance). Only in a few experiments a second coarse mode of a larger particle size ranging from 4 to 9 µm could be observed because response with respect to aerosol mass was relatively low. Even larger particles are further quickly deposited before they can accumulate to sufficiently high concentrations necessary for measurement with this method.

Particles larger than 4 µm proved difficult to measure using scattered light analysis, because aerosol-mass specific light scattering intensities rapidly decrease above that size (and are lost in light scattering background of smaller particles). In total, these particles should therefore not play a major role in aerosol visibility. For detailed analysis of large particles in such aerosol, more advanced measurement methods are required which, without further countermeasures, however, may not withstand the corrosive combustion products over prolonged times.

Supplementary measurements with an optical particle counter after combustion of very small amounts of sample as shown in Figure 32 confirmed the presence of particles exceeding diameters of 2 µm. Because particle size resolution of the instrument used were low, presence of multiple modes, particle size changes or precise volume concentrations, mass concentrations or diameters could not be determined with the

used instrument. Volume concentrations in Figure 32 were estimated assuming spherical particles and constant number distributions in each size class.

For Composite K, particles with diameters in the range of 2 ~ 5 µm were detected, but make up only a small fraction as number concentrations. Thus they do only minimally contribute to light scattering and were not detected in the measurements using the PSD analyzer. Quick disappearance of large particles formed after combustion of composite-A confirmed loss of aerosol particles by deposition. Other particle measurement methods (e.g. mobility particle sizer) may provide better size resolution and enable measurement of the highly concentrated aerosols generated in chamber experiments, but require measures against particle size drifts caused by change in relative humidity (e.g. by dilution) and corrosion of instrument parts by the combustion products.

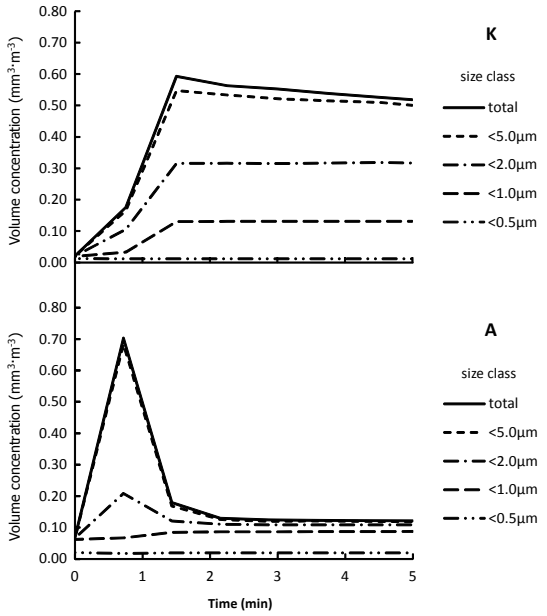

Figure 32. Particle counter results converted to volume concentrations after combustion of 23 mg composite-K at 80%RH and 41 mg composite-A at 88%RH.

5.3.3. Temperature Dependence of Humidity Curves

To characterize the aerosol's opacity at given conditions in simple charts, the maximum reading of b^* was extracted for each experiment. Values of b^*_{max} plotted against humidity show characteristic curves, depicting aerosol properties for each composite (Figure 33). These curves are independent of temperature and coincide for measurements performed in this study at 20°C and 30°C (for BP also at 10°C). Combustion products forming solids by a phase transition from the gas-phase typically produce fine aerosol particles

in the sub-micrometer size-range and show a base-line at dry conditions. These particles can further grow when relative humidity exceeds a characteristic threshold to form larger particles displaying higher scattering efficiencies, if they contain a hygroscopic combustion product. Critical relative humidity, at which it starts absorbing water vapor to form a liquid phase, is easily recognizable by an abrupt rise in the curve's slope and can be found in literature for many compounds.

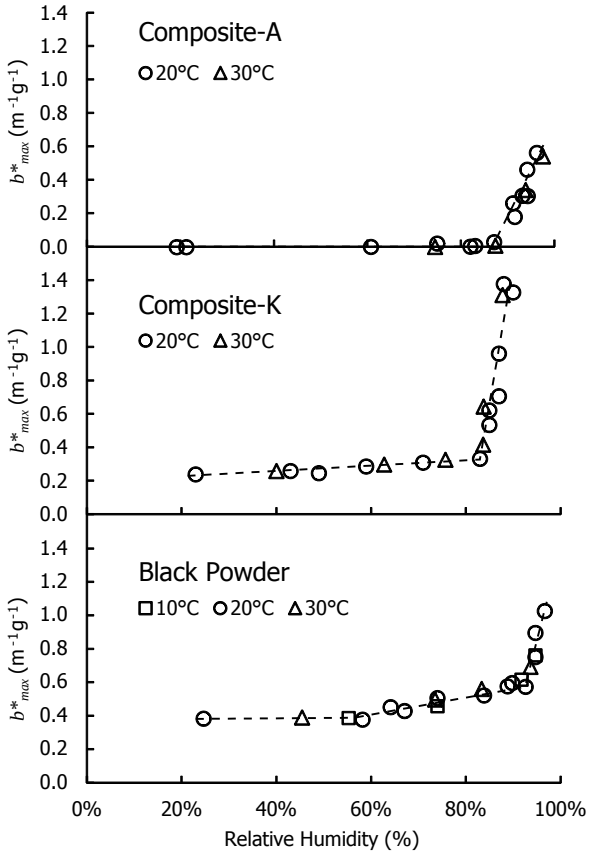

Figure 33. b^*_{max} of composite-K, composite-A measured at 20°C and 30°C, of BP also at 10°C plotted against initial relative humidity. (For composite-K values go up to 2.48 at 96% RH, but are not plotted.).

Composite-A developed no visible aerosol at all for humidity settings below 80% RH, because its primary combustion products only consist of gases. Hydrochloric acid, one of its combustion products, produced particles which rapidly grow by absorbing water vapor at highly humid conditions causing a rise in b^*_{max}. Under experimental conditions, however, particles grew too large to stay suspended in the confined volume of the chamber and were quickly deposited on chamber surfaces. Therefore, b^* only briefly rose and the air in the chamber cleared up almost completely within a few minutes. This

kind of deposition may not occur quickly in open air. Therefore aerosols may be persistent and reach higher opacities than these measurements suggest.

Aerosols emitted by combustion of composite-K consist of KCl. Therefore, the plot of b^*_{max} is constant until critical relative humidity of KCl is reached at 85% where the plot shows a sharp rise. Unlike in composite-A, particle size does not grow so large that particles are deposited quickly.

Combustion products of black powder consist of a complex mixture of solids and gases. Main components found in the solid fraction include K_2SO_4 and K_2CO_3, among others (von Maltitz, 2004) of which only K_2CO_3 is hygroscopic with a critical relative humidity of 43%. Its high solubility and low abundance result in a moderate rise of aerosol opacity in respect to relative humidity. The final steeper rise at near saturation humidity can be attributed to K_2SO_4 (critical relative humidity: 97%).

PSDs measured with the Mie scattering analyzer showed only a single mode for the composites measured in this work. Other modes do obviously exist, as indicated by particle counter measurements, but light scattering properties can approximately be represented by the single mode PSD measured. The size effect can be visualized more easily by plotting mode diameters of the PSDs at maximal attenuation. These plots (Figure 34) look remarkably similar to b^*_{max} (Figure 33), but show a less intensive rise at high humidity conditions. Significant increase in particle size from a few hundred nm to the µm-range is causing the higher b^*_{max} in composite K at high RH conditions. KCl particles undergo hygroscopic growth by reduced vapor-pressure of water. For black powder, however, no rise in particle diameter is observed at all with increasing RH, although b^*_{max} clearly shows a rising tendency. Here, the main aerosol constituent K_2SO_4 does not display a simple hygroscopic growth mechanism as with composite K. The increase of b^*_{max}, in this case may be indicating growth of the hygroscopic subcomponent K_2CO_3 existing as separate particles of different size, which could not be resolved in the presence of large amounts of K_2SO_4 particles. Also the PSD analyzer is not able to measure volume or number concentration values, which would provide more insight. To properly explain complex growth phenomena like those occurring in the example of black powder, more sophisticated measurement methods with a wider dynamic range are required.

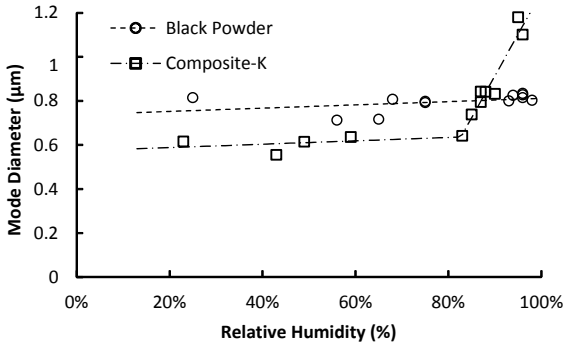

Figure 34. Aerosol mode diameter at the time of b^*_{max} plotted against initial relative humidity.

5.3.4. Effect of Additives

Fine aerosol particles are generated at high number concentrations from metal chloride or metal vapors during combustion and act as condensation nuclei for H_2O and HCl vapors when cooled to ambient temperatures. At high relative humidity conditions, they grow to particle sizes up to diameters of around 1µm within minutes as can be seen in Figure 35a for aerosol generated from 2 g of an AP/HTPB composite with 10% of CuO additive at 89% RH. Light extinction has been shown above to be proportional to sample-mass and can be normalized as a sample-mass specific scattering or extinction coefficient b^*. The temporal development of aerosols from metal compound additives is analogous to that of potassium perchlorate based composites depicted in Figure 30. In the initial growth phase (Phase I) driven by condensation of H_2O and HCl vapors, particles gain on light scattering efficiency until light extinction reaches its maximum at the point indicated by the dashed line. Although maximum light scattering efficiency for a single aqueous particle should lie at a diameter of 1.3 µm (1.0 µm for λ = 500 nm (Jacobson, 2005c)) according to MIE theory, mode diameters of PSDs have only been observed at around 0.6 µm at the maximum of light extinction in 670 nm laser measurements (Figure 35 b). Thereafter growth by coagulation and, if particles grow too large, deposition processes on chamber surfaces take over and light extinction starts to decrease due to loss in particle number-concentration (Phase II). It was not possible to obtain quantitative data as number concentrations from PSD measurements in the current setup, but the continuing growth in size suggest coagulation as the growth mechanism during Phase II. Compared to the rising slope b^* displays during Phase I, Phase II can be considered having only low influence on the maximum value of b^*. At very dry conditions extinction coefficient even reaches a constant value almost instantly

and does not decrease notably within the observed time span. The maximum value of sample-mass specific light extinction b^*_{max} can be extracted for each combustion experiment as a measure for the aerosol's obscuring potential

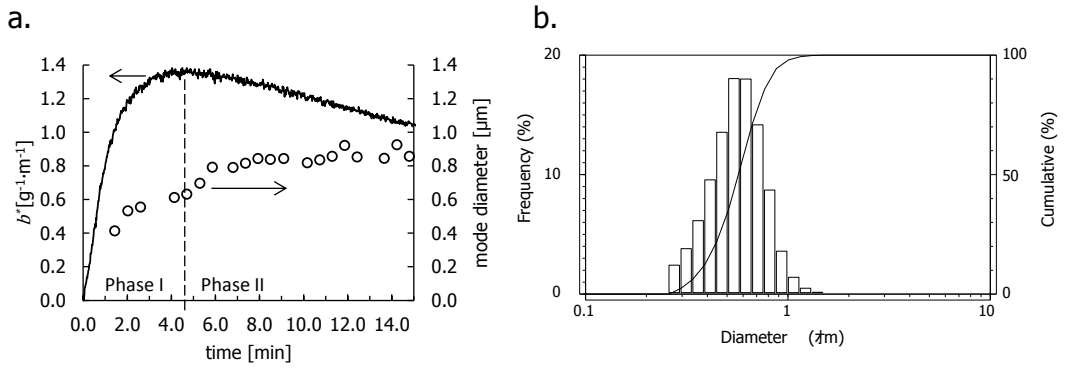

Figure 35. a. Change of sample-mass specific extinction coefficient b^* and mode diameter of aerosol from AP/HTPB composites with 10% CuO additive over time b. PSD measured at maximum light extinction, 4.7 minutes after ignition.

A series of b^*_{max} measurements can efficiently describe the humidity characteristics of a test-composite. The base composition of AP/HTPB-composites used in this work produces only negligible amounts of visible aerosol up to about 80% RH. In Figure 36, b^*_{max} is plotted against initial relative humidity. Usage of potassium perchlorate (KP) would result in a high baseline throughout the whole humidity range with a sharp increase over 85% RH. Metal compound additives like $SrCO_3$ induce visible aerosol development from AP/HTPB composites even below 80% RH. b^*_{max} moderately increases with rising relative humidity until it shows a steep rise over 80% RH. Hygroscopic aerosol particles already form aqueous solutions by absorbing H_2O vapors at lower RH and efficiently scavenge excess HCl vapors emitted by the composite. Growth of such particles can be considered being controlled mainly by the HCl/H_2O system and causes the steep rise in light scattering efficiency over 80%RH. Visible aerosol increase can therefore be best extracted at 80% RH where the effect of metal compound additives is high while aerosol which may originate from the base composition itself is negligible. Also, losses due to coagulation and deposition processes, which would increase with growing particle sizes at higher RH, can be kept within acceptable limits. Results for metal powder additives and flame coloring additives are analyzed separately, because of differences in their combustion behavior and combustion products involved. Further Fe_2O_3, which is often used as catalyst in pyrotechnics to increase the combustion speed, is discussed together with the coloring agents.

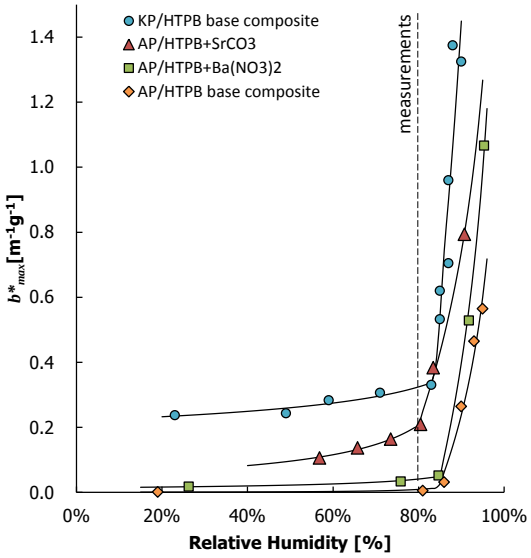

Figure 36. Humidity dependence of maximum sample-mass specific extinction coefficient of KP/HTPB base composite and AP/HTPB composites with 5% of $SrCO_3$, $Ba(NO_3)_2$ and without additives.

5.3.4.1. Metal Powders

Sparkling effects in pyrotechnics are produced by burning metal particles which burn at lower combustion rates than the composite itself. The metal particles are ignited but not evaporated in the pyrotechnic flame and continue burning after being ejected into ambient air. The particles' incandescent light emissions depend on particle temperature and combustion times which are influenced by metal type and particle properties such as size and shape. If particles burn long enough, tail or willow-like effects can be produced. For some metals, particles can also burst during combustion (e.g., Ti) and add a crackling effect. Most of the material, however, remains in the condensed phase during the whole process and very low levels of smoke have been observed for composites containing Al and Ti powders compared to samples containing Mg, as a plot of b^*_{max} at 80%RH against amount of added metal shows in Figure 37.

Mg represents an exception to combustion mechanism observed for other metals. Due to its low boiling point of 1363K, compared to the other metals (Al: 2743 K; Ti: 3560 K), it evaporates within the flame, unless metal particles are very large, and can contribute to higher flame temperatures there. Thus AP/HTPB composites containing only Mg powder additive does not emit incandescent light at all, despite the very bright flame burning Mg produces as bulk material. If solid or liquid particles are present in the flame, however, a bright high temperature incandescent flame can be produced (e.g.,

white stars with $Ba(NO_3)_2$ or Mg flash-compositions). As a result Mg produces fine aerosol particles of MgO at high number concentrations by homogeneous nucleation from the gas phase. These hygroscopic particles absorb HCl and H_2O vapor to form aqueous solutions of $MgCl_2$ and HCl which grow in size, particularly under high RH. The slope for AP/HTPB with Mg flattens at high ratios of Mg in Figure 37, due to reduced emissions of free HCl from a lower proportion of AP/HTPB base composite (in 2 g sample) and accelerated coagulation of particles at high aerosol concentrations.

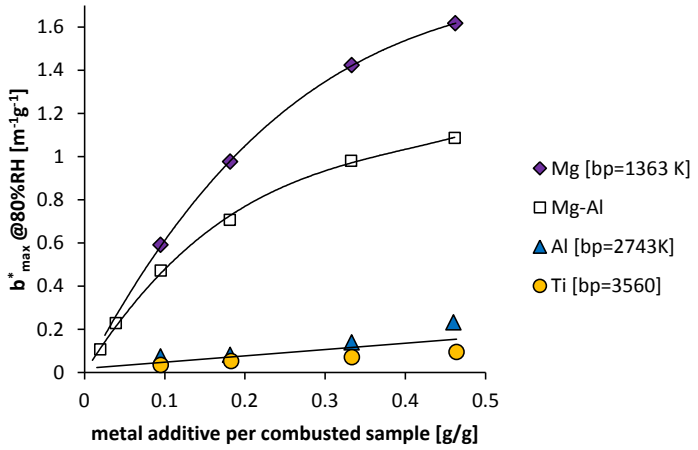

Figure 37. Maximum sample-mass specific extinction coefficient of AP/HTPB composites with Mg, Mg-Al, Al and Ti metal powder additives at 80% RH show the role of Mg in aerosol development. Boiling points (Zhang, 2011) are denoted as "b.p."

Mg-Al behaves very similar to Mg in respect to visible aerosol formation, but produces bright white sparks. Clearly Al is responsible for the metal particles not evaporating completely during combustion in the composite flame due to its higher boiling point at 2743 K. Some of the Al seems to be evaporated, though, as light extinction measurements suggest. Values of b^*_{max} are significantly higher than would account for half the amount of Mg as would be expected from the proportion of Mg in the alloy. Higher temperatures of metal-particles resulting from better combustion performance of Mg-Al compared to Al also support this. Elemental analysis of aerosol particles should provide insight into the mechanism of this phenomenon.

Particle emissions of aluminium oxides have been reported for combustion plumes of solid rocket motors to have maxima in their PSDs at 0.1 and 2 µm. (Ross, et al., 1999) These particles act as condensation nuclei for H_2O vapor and HCl emissions, which can be observed as thick white rocket trails. Combustion in these propellants, however, follow a different temperature and pressure profile during combustion and use atomized

aluminium, which has combustion characteristics different from aluminium flakes common in firework pyrotechnics. Aluminium is therefore much more readily vaporized in those propellants than Al and Ti used as spark effect metals in pyrotechnics. In case of magnalium, Al vapors may be present more abundantly during combustion due to Mg supporting the combustion and evaporation process of the metal particles.

Particle emissions of aluminium oxides have been reported for combustion plumes of solid rocket motors to have maxima in their PSDs at 0.1 and 2 μm. (Ross, et al., 1999) These particles act as condensation nuclei for H_2O vapor and HCl emissions, which can be observed as thick white rocket trails. Combustion in these propellants, however, follow a different temperature and pressure profile during combustion and use atomized aluminium, which has combustion characteristics different from aluminium flakes common in firework pyrotechnics. Aluminium is therefore much more readily vaporized in those propellants than Al and Ti used as spark effect metals in pyrotechnics. In case of magnalium, Al vapors may be present more abundantly during combustion due to Mg supporting the combustion and evaporation process of the metal particles.

5.3.4.2. Flame Coloring Agents

Flame coloring compounds form volatile metal chlorides ($BaCl_2$, CuCl, NaCl, and $SrCl_2$) during combustion, which produce fine aerosol particles by homogeneous nucleation during rapid cooling of the exhaust gas. Figure 38 shows linear plots of b^*_{max} against metal chloride mass formed per g composite during combustion, which flatten out at high additive ratios because combustion performance cannot be sustained by the base composite. Furthermore, all metal chlorides except $BaCl_2$ show the same slope, which implies that aerosol nucleation and growth processes at high temperatures (boiling points are 1833, 1763, 1686 and 1523 K, respectively (Perry, 2011)) immediately after combustion results in particle number-concentrations proportional to mass concentrations, even for metal chlorides. Mg from the previous section would also fit the common slope of the colorants if it is considered an analogous nucleation process of MgO from Mg vapor. This suggests that particles produced by rapid condensation at high temperatures have the same average masses rather than diameters or volumes for all compounds. When cooled to ambient temperatures at high RH, these hygroscopic particles grow by uptake of HCl and H_2O and become highly efficient in light scattering.

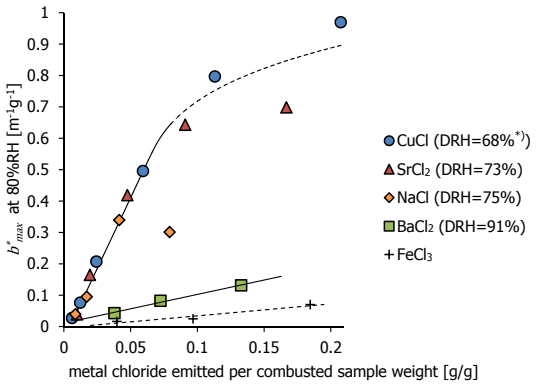

Figure 38. Maximum sample-mass specific extinction coefficient of AP/HTPB composites with CuO, $SrCO_3$, $Na_2C_2O_4$ $Ba(NO_3)_2$ calculated as chlorides formed during combustion. Deliquescent relative humidity (Greenspan, 1977) annotated as "DRH". *) DRH of $CuCl_2$ (Rockland, 1960)

$BaCl_2$, which showed low visible aerosol response, has the highest deliquescence relative humidity value (91% RH at 20°C) (World Meteorological Organization, 2008) among the tested metal compounds (68%, 73%, 75% RH for $CuCl_2$, $SrCl_2$ and NaCl respectively – CuCl is oxidized and converted to $CuCl_2$ by O_2 and HCl over 50% RH (Richardson, 1997)). HCl vapor therefore does not condensate on $BaCl_2$ particles. Instead, HCl and H_2O vapors are absorbed by heterogeneous nucleation on other hygroscopic particles present in ambient air. This results in formation of large particles at low number concentration analogous to the base composite without additives. This is observed over the whole humidity range and is also seen in Figure 36, where b^*_{max} of AP/HTPB with 5% of $Ba(NO_3)_2$ additive only slightly surpass those of the base composite. For $Ba(NO_3)_2$ additives, PSDs could not be measured in the current setup, because overall scattering efficiencies were too low. Weak forward-scattered light of the transmission lasers has however been observed with the naked eye through the transparent chamber walls at relatively large scattering angles up to around 45°, suggesting particles sized in the range of a few 100 nm.

Fe_2O_3, which catalyzes decomposition of the HTPB binder during combustion is converted to gaseous $FeCl_3$, has a much lower boiling point of 553~589 K because of its molecular structure and ability to form dimers. It will therefore stay gaseous longer than chlorides from coloring agents. Although $FeCl_3$ is very hygroscopic, its presence does not increase light extinction noticeably. In Figure 38, its plot rises only marginally to 0.07 at its maximum addition ratio of 10%. It can be therefore said, that $FeCl_3$ will

only form aerosol particles at much lower concentrations than compounds condensating at high temperatures if at all. A plot of b^*_{max} over humidity is practically indistinguishable from plots of aerosol produced by the base composite. Under very high RH of over 90%, aerosol particles grow large enough for a faint brownish coloration from dissolved $FeCl_3$ to be observed.

When excessive amounts of additive are used, combustion performance (combustion speed) of the composite is degraded and aerosol opacity does not further increase linearly, because reduction of particle number-concentrations by coagulation-effects is accelerated and energy output of the base composite is not sufficient to support complete reaction and vaporization of the metal compounds or even stable combustion. For $Na_2C_2O_4$ the negative effect of its endotherm decomposition reaction appears most distinctly at additions as low as 10% (0.08 as NaCl in Figure 38), while for the same amounts of $SrCO_3$ (0.09 as $SrCl_2$) and CuO (0.11 as CuCl) b^*_{max} at 80% RH deviate only slightly from the linear trend. Also, color quality can be reduced by continuous spectrum emissions (condensed phase) or emission spectra (vapors) of interfering by-products, if too much additive is used. Additive ratios for a pyrotechnic composite therefore have to be optimized for each additive.

5.3.4.3. Light Intensity and Additive Ratio

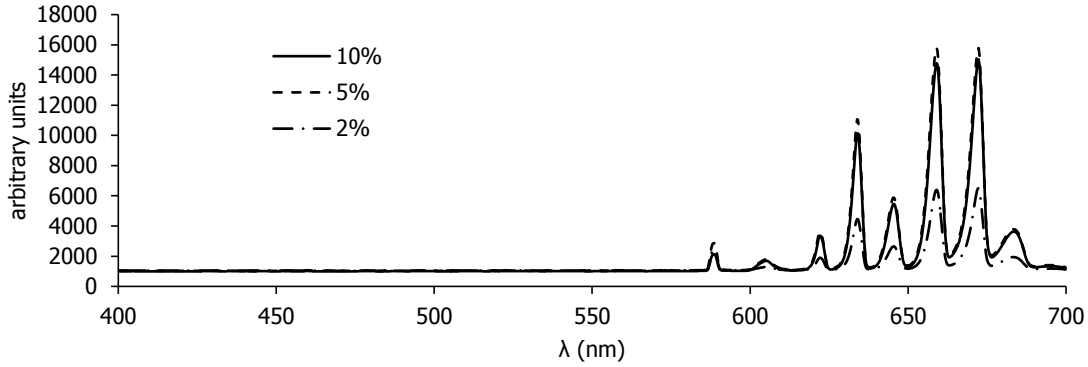

Figure 39. Emission spectra SrCl during combustion of AP/HTPB composite with 2, 5 and 10% $SrCO_3$ additive

Emission spectra of metal compound additives are converted to their corresponding metal chloride vapors during combustion as discussed above. These metal chlorides are partly converted to molecules capable of emitting characteristic colored light spectra by decaying from an excited state. (Kosanke & Kosanke, 2004) Intensities theoretically should be proportional to these species and increase with higher amounts of the

respective additives, as spectra in Figure 39 shows for AP/HTPB composites with 2 and 5% $SrCO_3$ additive. Further addition of 10% does not yield higher intensities, though aerosol emissions still rise as shown in 5.3.4.2. Measurement of emission spectra in combustion chamber experiments as shown in Figure 39 help finding appropriate additive ratios for the various flame coloring compounds, but are also subject to influences of the combustion platform and inhomogeneous ignition of the composite surfaces. Final decisions on visual appearance of different compositions therefore need to be evaluated in launch experiments.

5.3.5. Chemical Equilibrium and Particle Nucleation Calculations

All metal compounds used as coloring agents are transformed to their metal chlorides according to chemical equilibrium calculations and exist only in the gas phase at adiabatic combustion temperatures. Figure 40 shows the main species containing the respective metal in the case of $SrCO_3$ as additive. Dilution with ambient air first causes further increase in temperature, because combustion of the oxygen deficient composite can progress. Further dilution, however, cools the mixture and at around 1100°C after 5-fold dilution where the first condensed-phase species of liquid $SrCl_2$(L) appears, which subsequently transforms to solid phases of $SrCl_2$(b) and $SrCl_2$(a) representing high-temperature superionic and low-temperature phases (Hull, et al., 2011) of a cubic fluorite crystal-structure, respectively. Analogous formation of condensed phase metal chlorides from their vapors has been obtained as a result for all coloring agents. Only CuO shows the peculiarity of forming Cu metal vapor (which in experiments can be condensed as metal on cold surfaces held into the flame) before condensation as CuCl. Rapid cooling of those gaseous species by turbulent mixing lead to supersaturated conditions at high temperatures of over 1000°C under which particles are formed by a homogeneous nucleation process.

Except Mg which at least partly forms metal Mg and $MgCl_2$ vapors before condensing as MgO metals used for spark effects only form their oxides in liquid state. Mg follows the same scheme as the coloring agents with the difference of MgO forming from Mg or $MgCl_2$ vapor. When plot against MgO mass the slope of b^*_{max} also concords with the metal chlorides. Other metals actual combustion processes may not be sufficiently reproduced with chemical equilibrium calculations, but results showing only little aerosol formation support a combustion mechanism with minimal nucleation from the

gas phase.

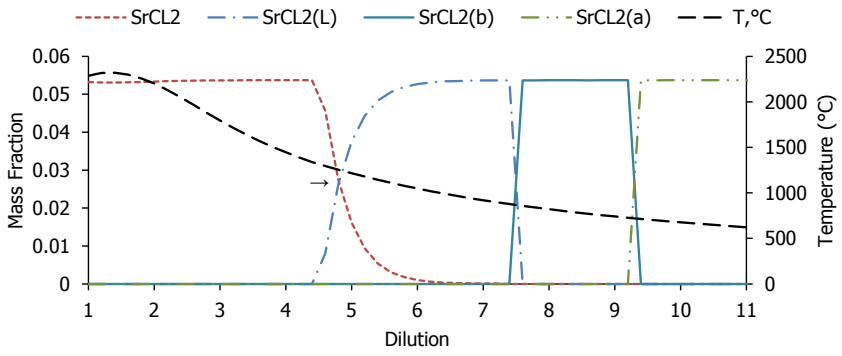

Figure 40. Equilibrium calculation results for AP/HTPB with 5% $SrCO_3$ additive and dilution with air. Mass fractions exclude mass added by dilution air.

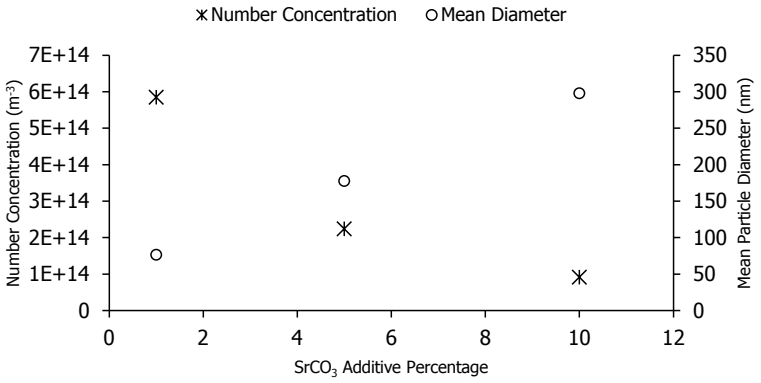

Figure 41. Simulation results modeling particle nucleation, growth and coagulation during dilution of vaporized $SrCl_2$ with ambient air within about 0.08 seconds.

Particle nucleation, growth by condensation of monomers and coagulation processes of vaporized metal chlorides could be described by solving General Dynamic Equation with available software (Prakash, et al., 2003). The model results in smaller particles and higher number concentrations at higher dilution (and consequently cooling) rates. Dilution rates were chosen so that exponential dilution of exhaust gas from the combustion to the chamber volume of $1m^3$ would complete in 0.0008 to 8 seconds. For all calculations an increase in metal chloride concentration formed from the additive compound would form significantly larger particles as Figure 41 shows for the case of $SrCO_3$. Number concentrations show therefore a decreasing trend with mass concentration of introduced metal chloride. This contradicts with the trends observed for light extinction properties of the aerosol, which would suggest equally sized particles regardless of concentration. It is an indication for too many assumptions having been

made in this application of the simple model beginning at the dilution rates and also including the particle growth and coagulation model itself, which assumes liquid particles, although temperatures approach or even fall below the melting points during the particle growth processes.

5.3.6. Aerosol Reduction Techniques

As the trends found in this study show, optical light extinction properties of aerosol is proportional to the mass of volatile metal chlorides set free by the pyrotechnic composition. These emissions can be reduced by adding less coloring agent additive. This needs to be balanced with the yield in light emission of the composition which also depends on additive ratio. Excess use of coloring agents, though is clearly has no merits, since intensities level off at high concentrations. For copper compounds, equilibrium calculations have however shown that sulfur, e.g., brought in in the form of copper(II)sulfate, will cause Cu_2S to be formed instead of CuCl from the metal vapor. This compound has a lower molar mass and produces therefore somewhat less primary aerosol mass, as could also be confirmed in experiments. Further, reduction of excess HCl emitted by the base composite can also reduce hygroscopic growth of the aerosol, though number concentrations of the metal-compound bearing particles may not be reduced.

5.4. Conclusion

Promotion of visible aerosol development by common additive metals (Mg, Al, magnalium, Ti) and flame coloring metal compounds ($Na_2C_2O_4$, CuO, $SrCO_3$, $Ba(NO_3)_2$) after combustion of pyrotechnic compositions based on the low-smoke oxidant/fuel system of ammonium perchlorate / hydroxyl-terminated poly-butadiene has been confirmed at high relative humidity above around 80%. With the exception of Al and Ti metal powders for sparkling effects and $Ba(NO_3)_2$ for green flames, which produce only minimal visible aerosols, light extinction has been found to increase proportionally with the mass concentration of the corresponding metal chloride (CuCl, NaCl, $SrCl_2$) or metal oxide (MgO) emissions. Fine aerosol particles are produced through homogeneous nucleation during the combustion process and act as condensation nuclei for HCl produced during combustion and H_2O vapors present in ambient air after dilution. Growth of these particles to highly opaque aerosols occurs distinctly at relative humidity above 80%. For low smoke pyrotechnics producing only little visible smoke

even under high relative humidity, Al and Ti are found to be effective spark-generating metals, while from the available coloring agents only Ba (green) is found to be unaffected by humidity. Iron (III) oxide (Fe_2O_3), which is often used as catalyst increasing combustion speed of composites, was found to have practically no influence on visible aerosol generation, because it forms iron(III)chloride which has a very low boiling point and therefore follows a different nucleation mechanism. Under RH conditions above 80%, use of Mg and magnalium should be avoided and replaced by Al and Ti as much as possible. Use of flame-coloring compounds of Cu (blue), Na (yellow) and Sr (red) produce thickening smoke at high humidity and needs to be minimized contrary to Ba (green) which does not increase smoke production.

Aerosol visibility at high humidity conditions evaluated in this chapter can directly be taken as a measure for CCN-active emissions. From global firework consumption of 0.28 Tg·yr^{-1}, (Tu & Granados, 2011; Xiangyi & Zhiwei, 2011) aerosol production can be estimated as around 0.028 Tg·yr^{-1}, assuming an average content of flame-coloring metal compounds and Mg of 10% in pyrotechnic compositions. This is seemingly low compared to other sources, e.g., biomass burning with 49.2 Tg·yr^{-1} or mineral dust with 1000-4000 Tg·yr^{-1}, but may still be relevant because of the extraordinary properties of these aerosol particles. With particle sizes reaching around 0.6 µm even in dry atmosphere, aerosol particles emitted by pyrotechnic compositions must be considered very good cloud condensation nuclei. At this size, increase of vapor pressure of small liquid particles due to surface curvature becomes almost insignificant. Therefore hygroscopic nature of metal chlorides which make up most of the particles emitted here make them activate as CCN at lower relative humidity conditions than other particles from gas to particle conversions like secondary aerosols or soot and thereby affect cloud droplet formation. On the other hand, compounds that produce low visible smoke emissions are associated with either low number concentrations due to large particle size or with almost non-hygroscopic particles, which are less likely to become CCN-active, especially if other CCN are present. Aerosols emitted by pyrotechnic compositions also pose a health risk as they can penetrate to the alveolar region and grow through absorption of water vapor to sizes over 1 µm at which they are efficiently deposited.

6. General Conclusions

For the two types of aerosol sources investigated in this work, new more detailed data on the nature of particle generation and growth or breakup of particles could be acquired. Usage of protein amino-acid composition in primary biological aerosol particles (PBAPs) discussed in Chapter 4 for source apportionment in a receptor model represents an alternative to tracer compounds used hitherto for this class of aerosol sources, in that most PBAPs can be detected using the same analysis method. Although the application of receptor models is very common for atmospheric aerosols, amino acids have not been recognized as relevant component to extract source contributions. In this work nonspecific detection of PBAPs with subsequent assignment of PBAP source classes from size resolved aerosol samples was attempted for the first time using amino acids. It has been found that sources such as pollen or dandruff among others which were formerly considered emitting mostly large particles also produce significant amounts of small particles down to the sub-µm range. Through size resolved analysis of amino acids in hydrolysate of aerosol sampled directly from emission sources as well as of ambient urban aerosol, size distributions at the site of emission and subsequent size transitions could be observed. For some PBAP sources, e.g., pollen and leaf debris, seasonal variation could be observed with pollen emissions starting in February and particles from leaves first occurring in November being ground down from coarse particles to fine particles until late spring. Combined amino acids in particles < 1.1 µm (112 $\mu g \cdot m^{-3}$ annual average) make up almost as much protein mass as in coarse particles > 7 µm (110 $\mu g \cdot m^{-3}$ annual average). Transport, grinding, and dispersion of plant debris and deposited coarse PBAPs estimated at a source strength of around 1000 $Tg \cdot yr^{-1}$ (Jaenicke, 2005) as well as microbiological material with soil and mineral dusts by road traffic needs to be reconsidered as a large source of fine suspended particulate matter also containing PBAPs. These results are contrary to the previous view that PBAPs mostly consist of coarse mode particles and implicate a health risk through permanent exposure of pulmonary alveoli to respirable PBAPs present in urban aerosols. Clearance of particles from this part of the lung poses a high level of stress to the immune system because the mucociliary clearance which physically transports depositions out of the lung is not available here. (World Health Organization, 1999) Together with exposure to sensitizing dusts these fine fractions of PBAPs may lead to increased occurrence of allergies. Regarding their properties as cloud condensation nuclei, PBAPs are recently assigned a role as giant CCN. (Posselt &

Lohmann, 2008). When considering size distributions based on number concentrations, which are relevant for these cloud droplet formation processes, small PBAPs < 1.1 µm would even greatly outnumber all larger size fractions. Because these particles are large enough for their activation as CCN to remain uninhibited by surface curvature, they might play an important role in cloud dynamics.

Chapter 5 presents an intercomparable method for measuring humidity characteristics of pyrotechnic aerosols, which allows estimation of visible smoke plumes from pyrotechnics. It has been shown that a small unpressurized combustion chamber is sufficient to achieve reproducible observations of these aerosols with sufficiently low deposition rates of relevant aerosol particles. Thanks to the chamber's small size controlled humidity and temperature conditions as well as homogenous aerosol distribution after combustion were reached quickly. The effect of metal and metal compound additives has been explained as Mg metal and metal chloride emissions which are volatile at combustion temperatures and form very small particles in the range of hundreds of nm by condensation from gaseous state. Especially avoiding the use of Mg-containing compounds (by replacement with Al and Ti) has been found an effective way to reduce aerosol emissions which form visible smoke plumes under high relative humidity. Coloring agents were found to produce highly concentrated metal chloride aerosols at particle sizes of several 100 nm. The number concentration of hygroscopic particles growing to a size of around 1 µm showed a peculiar linear dependence on mass concentrations of emitted metal chloride, which could not satisfactorily explained by numerical calculations particle formation and growth by nucleation, growth and coagulation processes after combustion. Of the flame coloring agents only $BaCl_2$ aerosols did not grow by absorption of water vapor at high relative humidity conditions. For these particles, particle sizes remain significantly smaller than the wavelength of light and therefore barely visible. They are therefore less efficiently scavenged by rainfall and are less likely to act as cloud condensation nuclei because of almost negligible hygroscopicity. Together with aerosols from Al and Ti metal which mostly produce particles larger than about 100 µm or more at low number concentrations it is applicable in low-smoke applications. For Mg-containing compositions and all other metal compounds used as coloring agents, resulting aerosols have proven very efficient condensation nuclei, most probably also promoted by the presence of excess HCl which condensates together with H_2O vapor. Therefore these particles can be expected to take part in aerosol-cloud interactions much more readily

than most aerosols considered in current models such as fly ash or soot particles from combustion of fossil or biogenic fuels which are much smaller with particle sizes of up to around 100 nm and are not hygroscopic if not even hydrophobic (cf. soot) when freshly emitted. Global annual emissions of aerosols from pyrotechnics as metal chlorides only make up 0.028 $Tg \cdot yr^{-1}$, but may become significant under unfavorable meteorological conditions because they tend to be concentrated both in time and space. In such cases aerosols from pyrotechnics not only can have an obvious influence on cloud and fog chemistry, but also on human health as well respirable aerosol particles containing heavy metal chlorides as well as other salts and soot along with gaseous pollutants, e.g., H_2S and NO_x emitted by the variety of compositions found in pyrotechnic products.

In this thesis, two potentially significant sources of aerosols with high contributions to the accumulation mode with particle sizes of around 1 µm have been characterized. PBAPs have been found not only to be ground down in deposition- and re-suspension processes such as erosion in arid regions or on roads, but also to be emitted directly by the aerosol source. They occur at much higher number concentrations than considered in current concepts assuming mostly coarse particles and are also significant in mass based size distributions. For aerosols emitted by pyrotechnical compositions, fine aerosol emissions were found to be almost inevitable for colored flame compositions with the exception of green coloring Ba compounds. In sparkling effects from metal powders, however, avoidance of Mg and Mg containing alloys is an effective alternative for low smoke compositions. Aerosols from pyrotechnics are also remarkable for their high hygroscopicity immanent to the metal chlorides needed for producing colored flames. Aerosol particles from these two different sources represent very good cloud condensation nuclei and occurring at this particle size influence the energy balance of this planet not only directly through (scattering) aerosol-radiation interactions, but also by inducing changes in aerosol-cloud interactions. Global estimated source strengths are 0.3 $Tg \cdot yr^{-1}$ and 1000 $Tg \cdot yr^{-1}$ for pyrotechnic aerosols and PBAPs, respectively. The latter only partly originates in urban regions where about half of the protein-containing particles were found in sub-µm particles and have different size distributions usually with presence of coarse particles elsewhere. Aerosols from pyrotechnics, on the other hand mostly contain sub-µm particles growing to 1µm or more under high humidity conditions apart from quickly precipitating large particles > 100 µm known as fallout. These two types of fine aerosols have not received appropriate attention and need to be taken into account in health assessments as well as radiative forcing models.

Acknowledgements

I would like to express my deep gratitude to Associate Professor Akutsu Yoshiaki, whose enthusiasm and support enabled me to do what has now become this dissertation. This work would not have been possible without the guidance he provided.

I would also like to thank Associate Professor Yoshinaga Jun, who provided the high volume aerosol sampler for the ambient aerosol and field measurements.

Special thanks also go to Haraguchi Tatsushige and his colleagues at the University of Tokyo Chichibu Forest, whose support allowed me to collect pollen samples directly from Japanese cedar trees with the cyclone separator while simultaneously collecting fine particulate matter with the aerosol sampler.

Also I would like to thank the Komaba Communication Plaza staff for providing the sampling location on the rooftop for urban ambient aerosols and the owner of Itamae-Ryōri “Ebisuya” who enabled me to collect the kitchen aerosol samples.

For the second part about pyrotechnics, many thanks go to Dr. Matsunaga Takehiro. Without his support and ideas measurements of the highly corrosive would not have succeeded. Dr. Okada Ken, thank you for the support with the measurement equipment. Great thanks go to Shimada Akihiro, who taught me how to prepare the pyrotechnic compositions safely and provided the know-how about how to best handle and ignite the composite samples.

Many thanks to all the colleagues in my Lab and last but not least also to Professor Kagemoto Hiroshi who retired from the Lab in spring 2014 for his support.

7. References

Abe, R. Y. & Puxbaum, H., 2006. *PM10-Aerosolquellenprofile aus den Bereichen Küchendämpfe, landwirtschaftliche Stäube und Straßenstäube.* Vienna: graduate thesis, Vienna University of Technology.

Albert, C., Lóki, K., Pohn, G. & Varga-Visi, É., 2008. Investigation of performic acid oxidation in cas of thiol-containig amino acid enantiomers. *Acta Universitatis Sapientiae, Alimentaria,* Volume 1, pp. 73-80.

Anon., 2013. *NIST-JANAF Thermochemical Tables.* [Online]
Available at: http://kinetics.nist.gov/janaf/

Armstrong, D. W., Kullman, J. P., Chen, X. & Rowe, M., 2001. Composition and Chirality of Amino Acids in Aerosol/Dust from Laboratory and Residential Enclosures. *Chirality,* Volume 13, pp. 153-158.

Badgujar, D., Talawar, M., Asthana, S. & Mahulikar, P., 2008. Advances in science and technology of modern energetic materials: An overview. *Journal of Hazardous Materials ,* 151(2-3), pp. 289-305.

Bauer, H. et al., 2003. Airborne bacteria as cloud condensation nuclei. *Journal of Geophysical Research,* 108(D21), p. 4658.

BGI, inc., 2001. *Sharp cyt cyclone instructions for use and maintainance.* Waltham: s.n.

Birgersson, B., Sterner, O. & Zimberson, E., 1988. Chemie und Gesundheit. In: *Eine verständliche Einführung in die Toxikologie.* Weinheim: Wiley-VCH, pp. 96-102.

Block, R. J. & Bolling, D., 1951. *The Amino Acid Composition of Proteins and Foods.* Second Edition ed. Springfield, Illinois: Charles C Thomas.

Bogdanovic, J. et al., 2006. Airborne exposure to wheat allergens: optimized elution for airborne dust samples. *Journal of Environmental Monitoring,* Volume 8, pp. 1043-1048.

Bohren, C. & Huffman, D. R., 1983. *Absorption and scattering of light by small particles.* Weinheim: WILEY-VCH Verlag GmbH & Co. KGaA.

Boogers, I., Plugge, W., Stokkermans, Y. Q. & Duchateau, A. L., 2008. Ultra-performance liquid chromatographic analysis of amino acids in protein hydrolysates using an automated pre-column derivatisation method. *Journal of Chromatography A,* Volume 1189, pp. 406-409.

Caseiro, A. et al., 2009. Wood burning impact on PM10 in three Austrian regions. *Atmospheric Environment,* Volume 43, pp. 2186-2195.

Cocks, A. T. & Fernando, R. P., 1981. The rates of formation of hydrogen chloride/water aerosols by homogeneous nucleation. *Atmospheric Environment,* 15(7), pp. 1293-1299.

Conkling, J. A., 1985. Smoke and Sound. In: *Chemistry of Pyrotechnics.* New York: Marcel Dekker Inc., pp. 167-179.

Cornfield, M. C. & Robson, A., 1955. The Amino Acid Composition of Wool. *Biochem J,* 59(1), pp. 62-68.

Custovic, A. et al., 1999. Dust mit allergens are carried on not only large particles. *Pediatr Allergy Immunol,* Volume 10, pp. 258-260.

Cziczo, D. J. & Abatt, J. P. D., 2000. Infrared observations of the response of NaCl, MgCl2, NH4HSO4, and NH4NO3 aerosols to changes in relative humidity from 298 to 238K. *Journal of Physical Chemistry,* Volume 104, pp. 2038-2047.

Dahneke, B., 1983. Simple Kinetic Theory of Brownian Diffusion in Vapors and Aerosols. In: R. E. Meyer, ed. *Theory of Dispersed Multiphase Flow: proceedings of an advanced seminar conducted by the Mathematics Research Center.* Madison: Academic Press, pp. 97-133.

Daniels, M. J., Domoinici, F., Samet, J. M. & Zeger, S. L., 2000. Estimating particulate matter-mortality dose-response curves and threshold levels: an analysis of daily time-series for the 20 largest US cities. *American Journal of Epidemiology,* 152(5), pp. 397-406.

Després, V. R. et al., 2012. Primary biological aerosol particles in the atmosphere: a review. *Tellus Ser B,* Volume 64.

Deutsche Forschungsgemeinschaft, 2012. Aerosole. In: *MAK- und BAT-Werte-Liste.* Weinheim: Wiley-VCH, pp. 188-196.

Drewnick, F. et al., 2006. Measurement of fine particulate and gas-phase species during the New Year's fireworks 2005 in Mainz, Germany. *Atmospheric Environment,* Volume 40, pp. 4316-4327.

Dutschke, A. et al., 2011. Aerosol Emissions from Outdoor Firework Displays. *Chemical Engineering & Technology,* 34(12), pp. 2044-2050.

Dutschke, A., Lohrer, C., Seeger, S. & Kurth, L., 2009. Gasförmige und feste Reaktionsprodukte beim Abbrand von Indoor-Feuerwerk. *Chemie Ingenieur Technik,* 81(1-2), pp. 167-176.

Elsasser, M. et al., 2013. Dynamic Changes of the Aerosol Composition and Concentration during Different Burning Phases of Wood Combustion. *Energy & Fuels,* Volume 27, pp. 4959-4968.

Flateau, P. J., 2011. *scatterlib.* [Online]
Available at: https://code.google.com/p/scatterlib

Franze, T., Krauser, K., Niessner, R. & Pöschl, U., 2003. Proteins and Amino Acids in Air Particulate Matter. *J Aerosol Sci,* 34(Supplement 2), pp. S777-778.

Greenspan, L., 1977. Humidity Fixed Points of Binary Saturated Aqueous Solutions. *Journal of Research for the National Bureau of Standards - A. Physics and Chemistry,* 81A(1), pp. 89-96.

Hanley, J. T. & Mack, E. J., 1980. *A laboaratory investigation of aerosol and extinction characteristics for Salty Dog, NWC 29 and NWC 78 pyrotechnics,* Washington DC: Calspan Report No 6665-M-1, Department of the Navy Naval Air Systems Commmand.

Hardt, A. P., 2001. Generation of Smoke. In: *Pyrotechnics.* Post Falls: Pyrotechnica Publications, pp. 318-332.

Harkoma, M., 2013. Visual and Near Infrared Mass Extinction Coefficient of Five Pyrotechnic Screening Smokes. *Journal of Pyrotechnics,* Volume 32, pp. 67-77.

Hering, S. V., 1995. Impactors, Cyclones, and Other Inertial and Gravitational Collectors. In: B. s. Cohen & S. V. Hering, eds. *Air Sampling Instruments for Evaluation of Atmospheric Contaminants.* Ohio: American Conference of Governmental Industrial Hygienists Committee, pp. 279-321.

Holmquist, L. & Vesterber, O., 2002. Direct on air sampling filter quantification of cat allergen. *J Biochem Biophys Methods,* Volume 51, pp. 17-25.

Hull, S. et al., 2011. High temperature crystal structures and superionic properties of SrCl2, SrBr2, BaCl2 and BaBr2. *Journal of Solid State Chemistry,* Volume 184, pp. 2925-2935.

IPCC, 2013. Climate Change 2013: The Physical Basis. In: T. F. Stocker, et al. eds. *Working Group I Contribution to the Fifth Assessment Report of the Intergovernmental Panel on Climate Change.* New York: Cambridge University Press, p. 595ff.

Itamae-Ryōri "Ebisuya", 2009. Meguro: Komaba 1-44-13.

Jacobson, M. Z., 2005a. Brief history of air-pollution science. In: *Fundamentals of Atmospheric Modelling, Second Edition.* New York: Cambridge University Press, pp. 470-493.

Jacobson, M. Z., 2005b. Aerosol emission and nucleation. In: *Fundamentals of Atmospheric Modelling, Second Edition.* New York: Cambridge University Press, pp. 470-493.

Jacobson, M. Z., 2005c. Radiative Energy Transfer. In: *Fundamentals of Atmospheric Modelling, Second Edition.* New York: Cambridge University Press, pp. 301-312.

Jacobs, P. W. M. & Whitehead, H. M., 1969. Decomposition and Combustion of Ammonium Perchlorate. *Chemical Reviews,* 69(4), pp. 551-590.

Jaenicke, R., 2005. Abundance of Cellular Material and Proteins in the Atmosphere. *Science,* Volume 308, p. 73.

Japan Meteorological Agency, 2009. *Kosa (Aeolian Dust).* [Online]
Available at: http://www.data.kishou.go.jp/obs-env/kosahp/kosa_data_index.html

Johri, B. M. & Vasil, I. K., 1961. Physiology of Pollen. *The Botanical Review,* 27(3), pp. 325-381.

Kasper, A. & Puxbaum, H., 1998. Seasonal variation of SO2, HNO3, NH3 and selected aerosol

components at sonnblick (3106 m a.s.l). *Atmospheric Environment,* 32(23), pp. 3925-3939.

Kenny, L. C., Gussman, R. & Meyer, M., 2000. Development of a Sharp-Cut Cyclone for Ambient Aerosol Monitoring Applications. *Aerosol Sci Technol,* Volume 32, pp. 338-358.

Kosanke, K. L. & Kosanke, B. J., 2004. The Chemistry of Colored Flame. In: *Pyrotechnic Chemistry.* Whitewater: Journal of Pyrotechnics Inc., pp. 25-49.

Kubota, N., 2004. Propellant Chemistry. In: *Pyrotechnic Chemistry.* Whitewater: Journal of Pyrotechnics Inc., pp. 7-11.

Kubota, N., 2007. Combustion of Composite Propellants. In: *Propellants and Explosives.* second ed. Weinheim: Wiley-VCH, pp. 181-233.

Lapple, C. E., 1951. Processes Use Many Collector Types. *Chem Eng,* Volume 58, pp. 144-151.

Lesniewski, T. K. & Friedlander, S. K., 1998. Particle nucleation and growth in a free turbulent jet. *Proc. R. Soc. Lond. A,* Volume 454, pp. 2477-2504.

Lidén, G. & Gudmundsson, A., 1996. Semi-empirical modelling to generalise the dependence of cyclone collection efficiency on operating conditions and cyclone design. *Joural of Aerosol Science,* 28(5), pp. 853-874.

Liou, K. N., 2002. Light scattering by particulates in the atmosphere. In: *An Introduction to Atmospheric Radiation.* San Diego: Academic Press, pp. 169-195.

Liu, H. J. et al., 1995. Determination of Amino Acids in Food and Feed by Derivatization with 6-Aminoquinoyl-N-Hydroxysuccinimidyl Carbamate and Reversed-Phase Liquid Chromatographic Separation. *J AOAC Int,* 78(3), pp. 736-744.

Marhold, H., 2003. Feinstaubproblematik in Linz. In: *Grüne Reihe Bericht Nr. 1.* Linz: Amt für. Umwelt und Naturschutz, pp. 5-38.

Miguel, A. G., Cass, G. R., Glovsky, M. M. & Weiss, J., 1999. Allergens in Paved Road Dust and Airbornde Particles. *Environ Sci Technol,* Volume 33, pp. 4159-4168.

Milne, P. J. & Zika, R. G., 1993. Amino Acid Nitrogen in Atmospheric Aerosols: Occurence, Sources and Photochemical Modification. *Journal of Atmospheric Chemistry,* Volume 16, pp. 361-398.

Motta, A. C. et al., 2006. Traffic-Related Air Pollutants Induce Release of Allergen-Containing Cytoplasmic Granules from Grass Pollen. *International Archives of Allergy and Immunology,* Volume 139, pp. 294-298.

National Institue for Environmental Studies, Tsukuba, 2010. *Air quality time series data download.* [Online]
Available at: http://www.nies.go.jp/igreen/tj_down.html

Neuberger, M. et al., 2004. Acute effects of particulate matter on respiratory diseases, symptoms and functions: epidemiological results of the Austrian Project on Health Effects of Particulate Matter (AUHEP). *Atmospheric Environment,* Volume 38, pp. 3971-3981.

Pagoria, P. F., Lee, G. S., Mitchell, A. R. & Schmidt, R. D., 2002. A review of energetic materials synthesis. *Thermochimica Acta ,* 384(1-2), pp. 187-204.

Pall Life Sciences, 2002. *Product Data - Pallflex® Filters.* Ann Arbor: Pall Corporation.

Patra, A. et al., 2008. On street observations of particulate matter movement and dispersion due to traffic on an urban road. *Atmos Environ,* Volume 42, pp. 3911-3926.

Peng, F. & Effler, S. W., 2012. Mass-specific scattering coefficient for natural minerogenic particle populations: particle size distribution effect and closure analyses. *Applied optics,* 51(13), pp. 2236-2249.

Perrot, L. et al., 2002. Yeast adapted to wine: Nitrogen compounds released during induced autolysis in a model wine. *J Ind Microbiol Biotechnol,* Volume 29, pp. 134-139.

Perry, D. L., 2011. *Handbook of Inorganic Compounds, Second Edition.* Boca Raton: Taylor & Francis Group.

Posselt, R. & Lohmann, U., 2008. Influence of giant CCN on warm rain processes in the ECHAM5 GCM. *Atmospheric Chemistry and Physics,* Volume 8, pp. 3769-3788.

Prahl, S., 2012. *Mie Scattering Calculator.* [Online]

Available at: http://omlc.ogi.edu/calc/mie_calc.html

Prakash, A., Bapat, A. P. & Zachariah, M. R., 2003. *NGDE: Software for Solution of Nucleation, Surface Growth and Coagulation Problems.* [Online]
Available at: http://www.me.umn.edu/~mrz/software.htm

Puxbaum, H., 2011. Aerosol Source-Receptor Studies. In: H. Puxbaum & W. Winiwarter, eds. *Advances of Atmospheric Aerosol Research in Austria.* Vienna: s.n., pp. 89-107.

Richardson, H. W., 1997. The Manufacture of Copper Compounds. In: *Handbook of copper compounds and applications.* New York: Marcel Dekker, Inc., pp. 53-92.

Robbins, C. R., 2012. Chemical Composition of Different Hair Types. In: *Chemical and Physical Behaivor of Human Hair.* Berlin Heidelberg: Springer-Verlag, pp. 105-175.

Rockland, L. B., 1960. Saturated Salt Solutions for Static Control of Relative Humidity between 5° and 40° C. *Analytical Chemistry,* 32(10), pp. 1375-1376.

Ross, M. N., Whitefield, P. D., Hagen, D. G. & Hopkins, A. R., 1999. In Situ Measurement of the Aerosol Size Distribution in Stratospheric Solid Rocket Motor Exhaust Plumes. *Geophysical Research Letters,* 26(7), pp. 819-822.

Sarkar, S. et al., 2010. Chemical speciation of respirable suspended particulate matter during a major firework festival in India. *Journal of Hazardous Materials,* Volume 184, pp. 321-330.

Schenkel, A. & Schaber, K., 1995. Growth of salt and acid aerosol particles in humid air. *Journal of Aerosol Science ,* 26(7), pp. 1029-1039.

Schmidl, C. et al., 2008. Chemical characterization of particle emissions from burning leaves. *Atmospheric Environmen,* Volume 42, pp. 9070-9079.

Senior, C. L. & Flagan, R. C., 1982. Ash Vaporization and Condensation During Combustion of a Suspended Coal Particle. *Aerosol Science and Technology,* 1(4), pp. 371-383.

Shimidzu, T., 1981. *Fireworks: The Art Science and Technique.* third ed. Austin: Pyrotechnica Publications.

Shi, Y. et al., 2011. Effect of fireworks display on perchlorate in air aerosols during the Spring Festival. *Atmospheric Environment,* Volume 45, pp. 1323-1327.

Swoboda, I. et al., 2004. Molecular Characterization of Polygalacturonases as Grass Pollen-Specific Marker Allergens: Expulsion from Pollen via Submicronic Respirable Particles. *J Immunol,* 172(10), pp. 6490-6500.

Tu, Y. & Granados, D. V., 2011. *2010 Fireworks annual report: Fireworks-related deaths, emergency department-treated injuries, and enforcement activities during 2010,* Bethesda: U.S. Consumer Product Safety Commission.

United States Environmental Protection Agency, 2005. *Chemical Mass Balance (CMB) Model.* [Online]
Available at: http://www.epa.gov/scram001/receptor_cmb.htm

van Wandelen, C. & Cohen, S. A., 1997. Using quaternary high-performance liquid chromatography elution systems for separating 6-aminoquinolyl-N-hydroxysuccinimidyl carbamate-derivatized amino acid mixtures. *J Chromatogr A,* Volume 763, pp. 11-22.

Vandenkerckhove, J. & Jaumotte, A., 1961. Remarks on the burning mechanism and erosive burning of ammonium perchlorate propellants. *Szmposium (International) on Combustion,* 8(1), pp. 689-693.

von Maltitz, I., 2004. Our Present Knowledge of the Chemistry of Black Powder. In: *Pyrotechnic Chemistry.* Whitewater: Journal of Pyrotechnics Inc., pp. 1-12.

Wang, Y., Zhuang, G., Xu, C. & An, Z., 2007. The air pollution caused by the burning of fireworks during the lantern festival in Beijing. *Atmospheric Environment ,* 41(2), pp. 417-431.

Wehner, B., Wiedensohler, A. & Heintzenberg, J., 2000. Submicrometer aerosol size distributions and mass concentration of the millennium fireworks 2000 in Leipzig, Germany. *Journal of Aerosol Science,* 31(12), pp. 1489-1493.

World Health Organization, 1999. *Hazard Prevention and Control in the Work Environment: Airborne Dust,* Geneva: WHO.

World Health Organization, 2003. *Health aspects of air pollution with particulate matter, ozone and nitrogen dioxide: Report on a WHO Working Group.* Basel: WHO, Regional Office for Europe.

World Meteorological Organization, 2008. Measurement of Humidity. In: *Guide to Meteorological Instruments and Methods of Observation, Seventh edition.* Geneva: WMO, p. I.4.

Xiangyi, X. & Zhiwei, F., 2011. Shining through. *China Daily USA*, 1 July.

Yasueda, H., Yasuo, Y., Shimizu, T. & Shida, T., 1983. Isolation and partial characterization of the major allergen from Japanese cedar (Cryptomeria japonica) pollen. *Journal of Allergy and Clinical Immunology,* 71(1), pp. 77-86.

Yu, M., Lin, J. & Chan, T., 2008. A New Moment Method for Solving the Coagulation Equation for Particles in Brownian Motion. *Aerosol Science and Technology,* Volume 42, pp. 705-713.

Zehe, M. J., 2010. *Chemical Equilibrium with Applications.* [Online]
Available at: http://www.grc.nasa.gov/WWW/CEAWeb/

Zhang, Y., 2011. Corrected Values for Boiling Points and Enthalpies of Vaporization of Elements in Handbooks. *Journal of Chemical Engineering,* Volume 56, pp. 328-337.

Zhou, K. & Chan, T. L., 2011. Simulation of Homogeneous Particle Nucleation in a Free Turbulent Jet. *Aerosol Science and Technology,* Volume 45, pp. 973-987.